



**UNIVERSITÀ DELLA CALABRIA**

Dipartimento di Ingegneria Civile

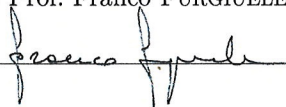
Dottorato di Ricerca in  
Ingegneria Civile e Industriale

**CICLO  
XXXI**

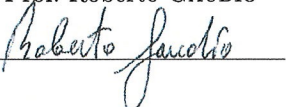
**INTERPRETATION OF LOCAL SCOURING AT BRIDGE PIERS AND  
ABUTMENTS WITH THE PHENOMENOLOGICAL THEORY OF  
TURBULENCE**

**Settore Scientifico Disciplinare  
ICAR/01 - Idraulica**

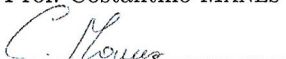
**Coordinatore:** Ch.mo Prof. Franco FURGIUELE

Firma 

**Supervisor:** Ch.mo Prof. Roberto GAUDIO

Firma 

Ch.mo Prof. Costantino MANES

Firma 

**Dottorando:** Dott. Francesco COSCARELLA

Firma 



*To those who love me...  
those that never wanted anything in return*

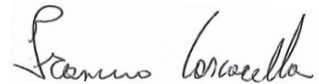


## Declaration

I hereby declare that, except where specific reference is made to the work of others, the contents of this dissertation are original and have not been submitted in whole or in part for consideration for any other degree or qualification in this, or any other university. This dissertation is my own work and contains nothing which is the outcome of work done in collaboration with others, except as specified in the text and Acknowledgements.

Saturday 16<sup>th</sup> February, 2019

Francesco COSCARELLA

A handwritten signature in black ink, reading "Francesco Coscarella". The signature is written in a cursive style with a large initial 'F'.



## Acknowledgements

Firstly, I would like to express my sincere gratitude to my supervisors Prof. Roberto Gaudio *Dipartimento di Ingegneria Civile, Università della Calabria*, and Prof. Costantino Manes *Dipartimento di Ingegneria dell'Ambiente, del Territorio e delle Infrastrutture, Politecnico di Torino* for the continuous support to my doctoral study. Their guidance helped me during the whole period of research and writing of this thesis. Their advices and recommendations during this three years of my life were priceless. I could not have imagined having a better advisors and mentors for my PhD study.

My sincere thanks also go to Dr. Nadia Penna, Dr. Domenico Ferraro, and Eng. Danilo Algieri Ferraro, who provided me the opportunity to join their team. Without their precious support, it would not be possible to conduct this research.

In the course of the study, I received much advice and assistance from several people. In particular, I wish to thank Eng. Fabio De Napoli, Mr. Claudio Capalbo, Mr. Francesco Leone, Mr. Salvatore Straticò for their technical assistance during the laboratory campaign.

My heartfelt thanks to the one who rapt my heart, Sara. Without her comfort, this study would never have been finished.

I thank also my friends and the Guides and Scouts of my Scout Group for supporting me spiritually throughout my life.

Last, but not least, I wish to thank my family. They encouraged me during my study to overcome all the problems.



## **Abstract**

The phenomenological theory of turbulence is here applied to the scouring phenomenon at bridge piers and abutments. In the last five decades many researches have been devoted to the development of predictive formulae able to quantify the maximum scour depth for both design and risk assessment needs of hydraulic structures. Owing to the complexity of the problem, most of the proposed formulae were developed on an empirical basis, which made them susceptible to scale issues and not fully consistent with the physics underpinning the scouring phenomenon. Recently, some studies of Gioia & Bombardelli (2005), Bombardelli & Gioia (2006), Manes & Brocchini (2015) and Ali & Dey (2018) have proposed a different approach, which exploits a theory to derive scaling relations between the equilibrium scour depth and non-dimensional parameters. Their work presented the phenomenological theory of turbulence and the paradigms of the sediment incipient motion theory assuming rough flow conditions, meaning that the momentum transport near the sediment-water interface was dominated by eddies belonging to the turbulent energy spectrum inertial range and scaling with the sediment diameter. In order to provide more general models and on the basis of the findings of Bonetti et al. (2017), the present work relaxes this as-

sumption by exploring the scaling of the equilibrium scour depth in cases where momentum transport is affected by eddies belonging to the dissipation and production range. This improvements were applied to the scouring phenomenon at bridge piers, to derive a predictive formula for the maximum scour depth, and to the scouring phenomenon at bridge abutments, to derive a scaling law that does not allow a directly assessment of the maximum scour depth, but provides new avenues for the development of general predictive formulae that are founded more on physical than empirical bases. In both cases, the proposed theory includes the relevant non-dimensional parameters controlling the scouring process and, contrary to commonly employed empirical formulae, it is free from scale issues.

## Sommario

La teoria fenomenologica della turbolenza è stata applicata ai fenomeni di escavazione alle pile e alle spalle di ponte. Negli ultimi cinquant'anni, per esigenze progettuali e di valutazione del rischio delle strutture idrauliche, molte ricerche sono state orientate allo sviluppo di formule predittive capaci di quantificare la massima profondità di scavo. A causa della complessità del problema, la maggior parte delle formule proposte è stata sviluppata su basi empiriche: ciò le ha rese non solo suscettibili di effetti scala, ma anche non coerenti con i fenomeni fisici alla base del processo di escavazione. Recentemente, Gioia & Bombardelli (2005), Bombardelli & Gioia (2006), Manes & Brocchini (2015) e Ali & Dey (2018) hanno proposto un approccio diverso, che sfrutta un approccio teorico per derivare le relazioni di proporzionalità tra la massima profondità di scavo all'equilibrio e parametri adimensionali. Il loro lavoro si è basato sulla teoria fenomenologica della turbolenza e quella del moto incipiente dei sedimenti assumendo condizioni di fondo scabro, ovvero in cui il trasporto della quantità di moto vicino all'interfaccia acqua-sedimenti era dominato da vortici appartenenti al *range* inerziale dello spettro di energia turbolenta e con dimensione dell'ordine del diametro dei sedimenti. Al fine di fornire modelli generalizzati, seguendo

Bonetti et al. (2017), il presente lavoro rende meno stringente quest'ipotesi analizzando la massima profondità di scavo all'equilibrio nei casi in cui il trasporto di quantità di moto è influenzato da vortici appartenenti ai *ranges* dissipativo e energetico. Per ricavare una formula predittiva della massima profondità di scavo, i miglioramenti proposti sono stati applicati al fenomeno dell'escavazione localizzata alle pile e alle spalle di ponte, al fine di derivare una relazione di proporzionalità che, seppur non consenta una stima diretta della massima profondità di scavo, fornisce nuovi orizzonti per lo sviluppo di formule predittive che si fondino su basi più fisiche che empiriche. In entrambi i casi, la teoria proposta considera i parametri adimensionali rilevanti che controllano il processo di scavo e, contrariamente alle formule empiriche comunemente utilizzate, è esente da effetti di scala.

# Contents

<b>List of figures</b>	<b>XX</b>
<b>List of tables</b>	<b>XXI</b>
<b>List of symbols</b>	<b>XXVII</b>
<b>Introduction</b>	<b>1</b>
<b>1 The phenomenological theory of turbulence and its applications in hydraulics</b>	<b>7</b>
1.1 State of the art . . . . .	7
1.2 Revised phenomenological theory of turbulence . . . . .	12
1.3 Co-spectral budget model and its developments . . . . .	18
1.3.1 Rough turbulent flow case . . . . .	27
1.3.2 Smooth turbulent flow case . . . . .	29
1.4 Summary . . . . .	32
<b>2 Near-bed eddy scales and clear-water local scouring around vertical cylinders</b>	<b>33</b>
2.1 Introduction . . . . .	33

---

2.2	A revisited theory . . . . .	36
2.2.1	$d/\eta$ effects . . . . .	42
2.2.2	$a/d$ effects . . . . .	50
2.3	A predictive formula for the clear-water maximum local scour depth at a vertical cylinder . . . . .	56
2.4	Example of application . . . . .	59
2.5	Conclusions . . . . .	60
<b>3</b>	<b>Local scour around bridge abutments and the phenomenol- ogy of turbulence</b>	<b>63</b>
3.1	Introduction . . . . .	63
3.2	Theoretical background . . . . .	65
3.3	Experimental setup and procedure . . . . .	69
3.3.1	Facilities . . . . .	69
3.3.2	Preliminary tests . . . . .	75
3.3.3	Design of the runs . . . . .	78
3.3.4	Experimental procedure . . . . .	79
3.4	Results and discussion . . . . .	102
3.5	Discussion and future investigation . . . . .	105
	<b>Conclusions</b>	<b>109</b>
	<b>References</b>	<b>120</b>

# List of Figures

1	Vortex flow and scour hole around a bridge pier (a) and abutment (b). . . . .	2
1.1	Energy cascade process; $\epsilon$ is the turbulent kinetic energy dissipation rate. . . . .	8
1.2	Sketch for the derivation of the turbulent shear stress. . . . .	14
1.3	The link between $\Gamma$ and the bulk variables $V$ , $R$ and the roughness size $d$ for a steady and uniform flow in an open channel with breadth $B$ and water depth $h$ . . . . .	17
1.4	Scheme of the idealized dimensionless vertical velocity spectrum $E_{ww}/E_{Kol}(K_a)$ . . . . .	21
1.5	$\alpha_1\alpha_2$ as a function of $d/R$ in the rough turbulent flow case. . . . .	29
1.6	$\alpha_1\alpha_2^{3/4}$ as a function of $Re$ in the smooth turbulent flow case. . . . .	31

2.1	Simple illustration of the interplay between eddies of scale $l = d + 5\eta$ and large-scale eddies. $V$ is the characteristic velocity of large-scale eddies (i.e., eddies scaling with $L$ ) and $w_l$ is the characteristic velocity of eddies scaling with $l$ ; $5\eta$ is the thickness of the viscous sublayer (Gioia & Chakraborty, 2006). . . . .	38
2.2	Ratio $w_l/w_d$ as a function of $d/\eta$ . . . . .	44
2.3	Dependence of $f_1$ on $d/\eta_1$ . Data by (a) Ettema (1980) and Ettema et al. (2006) and (b) Mignosa (1980), Yanmaz & Altinbilek (1991), Dey et al. (1995) and Sheppard et al. (2004). . . . .	49
2.4	(a) The von Kármán spectrum (dash-dotted line) and the Kolmogorov spectrum (solid line) in premultiplied form; (b) $w_d^P/w_d$ as a function of $y_{se}/d$ . . . . .	54
2.5	Function $f_2$ ; data by Ettema (1980) and Ettema et al. (2006). . . . .	55
2.6	Computed ( $y_{sec}$ ) vs measured ( $y_{sem}$ ) scour depths at equilibrium; (a) $y_{sec}$ from the revisited Manes & Brocchini (2015) theory; (b) $y_{sec}$ from the original Manes & Brocchini (2015) formulation; (c) $y_{sec}$ from the Richardson and Davis method (E. V. Richardson et al., 1993); (d) $y_{sec}$ from the Sheppard and Melville method (Melville (1997) and Sheppard & Miller Jr (2006)); data is taken from Ettema (1980), Ettema et al. (2006) (black squares) and Mignosa (1980), Yanmaz & Altinbilek (1991), Dey et al. (1995) and Sheppard et al. (2004) (full black circles). The solid lines represent the perfect agreement between measured and computed values, whereas the dashed lines represent the associated $\pm 30\%$ error bounds. . . . .	58



---

3.1	Flume details; (a) picture of the installation; (b) honeycomb and details of the triangular pipes. . . . .	70
3.2	Bazin weir used to measure the discharge. . . . .	71
3.3	Point gauge fitted with decimal Vernier placed in the piezometer. . . . .	72
3.4	Uniform sediments used in the recess box. . . . .	74
3.5	Flume bed upstream to the recess box divided in 4 reaches. . . . .	75
3.6	Abutment models: (a) $b = 15$ cm, (b) $b = 20$ cm, (c) $b = 25$ cm and (d) $b = 30$ cm. . . . .	76
3.7	(a) Traverse System; (b) ADV down-looking probe. . . . .	76
3.8	ADV probe and sampling volume. . . . .	77
3.9	Time evolution of the scour depth $y_s(t)$ for: (a) Run 1; (b) Run 2; (c) Run 3; (d) Run 4. . . . .	81
3.10	Time evolution of the scour depth $y_s(t)$ for: (a) Run 5; (b) Run 6; (c) Run 7; (d) Run 8. . . . .	82
3.11	Time evolution of the scour depth $y_s(t)$ for: (a) Run 9; (b) Run 10; (c) Run 11; (d) Run 12. . . . .	83
3.12	Time evolution of the scour depth $y_s(t)$ for: (a) Run 13; (b) Run 14; (c) Run 15; (d) Run 16. . . . .	84
3.13	(a) Nikon <sup>®</sup> D3000 camera with a Nikon <sup>®</sup> AF-S DX Zoom-Nikkor 18-55 mm lens; (b) photogrammetric targets; (c) Laser Scanner Leica ScanStation P20 <sup>®</sup> . . . . .	85
3.16	Example of wireframe view of a 3D polygonal mesh detail. . . . .	85
3.14	Example of 3D sparse point cloud of eroded bed captured through photogrammetric technique. The camera positions are identified by blue polygons. . . . .	86

3.15	Example of 3D edited dense point cloud of eroded bed captured through photogrammetric technique. The camera positions are identified by blue polygons. . . . .	86
3.17	3D polygonal mesh of Run 1. . . . .	87
3.18	3D polygonal mesh of Run 2. . . . .	87
3.19	3D polygonal mesh of Run 3. . . . .	87
3.20	3D polygonal mesh of Run 4. . . . .	88
3.21	3D polygonal mesh of Run 5. . . . .	88
3.22	3D polygonal mesh of Run 6. . . . .	88
3.23	3D polygonal mesh of Run 7. . . . .	89
3.24	3D polygonal mesh of Run 8. . . . .	89
3.25	3D polygonal mesh of Run 9. . . . .	89
3.26	3D polygonal mesh of Run 10. . . . .	90
3.27	3D polygonal mesh of Run 11. . . . .	90
3.28	3D polygonal mesh of Run 12. . . . .	90
3.29	3D polygonal mesh of Run 13. . . . .	91
3.30	3D polygonal mesh of Run 14. . . . .	91
3.31	3D polygonal mesh of Run 15. . . . .	91
3.32	3D polygonal mesh of Run 16. . . . .	92
3.33	Plan view of the 3D models and contours of the bed surface topography for Run 1. The red point and the black rectangle indicate the position of the maximum scour depth, $y_{se}$ , and of the abutment, respectively. Analogously for Figs. 3.34 to 3.48. . . . .	93
3.34	Plan view of the 3D models and contours of the bed surface topography for Run 2. . . . .	93

---

3.35	Plan view of the 3D models and contours of the bed surface topography for Run 3. . . . .	94
3.36	Plan view of the 3D models and contours of the bed surface topography for Run 4. . . . .	94
3.37	Plan view of the 3D models and contours of the bed surface topography for Run 5. . . . .	95
3.38	Plan view of the 3D models and contours of the bed surface topography for Run 6. . . . .	95
3.39	Plan view of the 3D models and contours of the bed surface topography for Run 7. . . . .	96
3.40	Plan view of the 3D models and contours of the bed surface topography for Run 8. . . . .	96
3.41	Plan view of the 3D models and contours of the bed surface topography for Run 9. . . . .	97
3.42	Plan view of the 3D models and contours of the bed surface topography for Run 10. . . . .	97
3.43	Plan view of the 3D models and contours of the bed surface topography for Run 11. . . . .	98
3.44	Plan view of the 3D models and contours of the bed surface topography for Run 12. . . . .	98
3.45	Plan view of the 3D models and contours of the bed surface topography for Run 13. . . . .	99
3.46	Plan view of the 3D models and contours of the bed surface topography for Run 14. . . . .	99
3.47	Plan view of the 3D models and contours of the bed surface topography for Run 15. . . . .	100

---

3.48	Plan view of the 3D models and contours of the bed surface topography for Run 16. . . . .	100
3.49	Example of a flow field measured with an ADV down-looking probe upstream to an abutment ( $x$ and $y$ are the streamwise and spanwise coordinates measured from the inlet and the left side of the flume, respectively). . . . .	102
3.50	Dimensionless scour depths $y_{se}g/U^2$ versus $\rho/(\rho_s - \rho) \cdot (b_{eff}/d_{50})^{2/3}$ ; (a) considering $b_{eff} = b$ , (b) considering $b_{eff} = b - b_r$ . The solid line represents the linear law of relation 3.19. . . . .	105
3.51	Dimensionless scour depths $V_{scour}^{2/3}g/(y_{se}U^2)$ versus $\rho/(\rho_s - \rho) \cdot (b_{eff}/d_{50})^{2/3}$ ; (a) considering $b_{eff} = b$ , (b) considering $b_{eff} = b - b_r$ . The solid line represents the linear law of relation 3.18 and the dashed lines the associated $\pm 25\%$ error bounds. . . . .	106
3.52	Scour hole shape for: (a) Run 16; (b) Run 15; (c) Run 14; (d) Run 12; (e) Run 3; (f) Run 5. . . . .	107

# List of Tables

2.1	Experimental range of used data-sets: $h$ is the flow depth, $B$ the channel breadth, $Fr = U/\sqrt{gh}$ the flow Froude number, $Re_a = Ua/\nu$ the pier Reynolds number. All the experiments were carried out using uniform sand of density $\rho_s = 2650$ kg/m <sup>3</sup> , except Mignosa (1980) experiments that were carried out using using uniform synthetic sediment of density $\rho_s = 1180$ kg/m <sup>3</sup> . . . . .	46
3.1	Experimental conditions. . . . .	80
3.2	Experimental characteristics in equilibrium conditions; $t$ is time to equilibrium, $T$ the average temperature during the run, $\nu$ the kinematic viscosity computed as a function of $T$ (expressed in °C) as $[1.14 - 3.1 \cdot 10^{-2}(T - 15) + 6.8 \cdot 10^{-4}(T - 15)^2] \cdot 10^{-6}$ m <sup>2</sup> /s (Julien, 1998). . . . .	101



# List of Symbols

$a$	pier diameter [L]
$Al$	parameter describing the alignment of the piers or abutments with respect to the flow direction [-]
$b$	abutment transversal length [L]
$b_{eff}$	effective abutment transversal length [L]
$b_r$	counter-rotating recirculation region width [L]
$B$	channel breadth [L]
$C_0$	universal Kolmogorov constant [-]
$C_d$	drag coefficient of piers or abutments [-]
$C_e$	effective discharge coefficient of the Bazin weir [ $L^{1/2}T^{-1}$ ]
$d$	sediment diameter [L]
$d_{50}$	median grain size of sediments [L]
$d_{16,84,95}$	sediment size for which 16%, 84%, 95% by weight of sediment is finer, respectively [L]
$D$	Batchelor structure function [ $L^2T^{-2}$ ]
$D_{Kol}$	Kolmogorov second-order structure function [ $L^2T^{-2}$ ]
$E$	energy spectrum [ $L^3T^{-2}$ ]
$E_{ww}$	energy spectrum of the vertical velocity [ $L^3T^{-2}$ ]
$E_{Kol}$	Kolmogorov energy spectrum [ $L^3T^{-2}$ ]
$f$	Shields mobility function for $d/\eta_1$ and relative roughness effects [-]

---

$f_1$	Shields mobility function for $d/\eta_1$ effects [-]
$f_2$	Shields mobility function for relative roughness effects [-]
$f_d$	friction factor [-]
$f_*$	auxiliary function for $\alpha_1\alpha_2$ esteem [-]
$F$	drag force acting on the pier [ $\text{MLT}^{-2}$ ]
$Fr$	flow Froude number [-]
$Fr_a$	pier Froude number [-]
$Fr_n$	abutment Froude number [-]
$F_{wu}$	co-spectrum between $u'$ and $w'$ [ $\text{L}^3\text{T}^{-2}$ ]
$g$	gravity acceleration [ $\text{LT}^{-2}$ ]
$h$	water depth [L]
$h_c$	height of the Bazin weir crest measured with the point gauge installed on the restitution channel [L]
$h_{c50}$	height of water surface 50 cm upstream the Bazin weir crest measured with the point gauge installed on the restitution channel [L]
$h_{p,in}$	measured initial piezometer water level with the point gauge inside the piezometer [L]
$h_{p,run}$	measured piezometer water level during runs with the point gauge inside the piezometer [L]
$h_w$	measured head above the Bazin weir crest [L]
$h_{we}$	effective head above the Bazin weir crest [L]
$i$	imaginary unit [-]
$k$	wavenumber [ $\text{L}^{-1}$ ]
$\mathbf{k}$	wavenumber vector [ $\text{L}^{-1}$ ]
$l$	length scale of generic eddies [L]
$L$	length scale of large eddies [L]
$L_w$	measured length of the Bazin weir crest [L]



---

$L_{we}$	effective length of the Bazin weir crest [L]
$M$	mass of the water contained within large-scale eddies [M]
$n$	Manning roughness coefficient [ $L^{-1/3}T$ ]
$p_w$	weir height [L]
$P$	power associated with large-scale eddies [ $ML^2T^{-3}$ ]
$P_{wu}$	covariance production term of co-spectral budget [ $L^3T^{-3}$ ]
$Q$	flume discharge [ $L^3T^{-1}$ ]
$\mathbf{r}$	incremental vector [L]
$Re$	Reynolds number [-]
$Re_a$	pier Reynolds number [-]
$Re_*$	shear Reynolds number [-]
$R$	hydraulic radius [L]
$\mathbf{R}$	two-point correlation [ $L^2T^{-2}$ ]
$S$	energy grade [-]
$Sh$	parameter describing the shape of the piers or abutments [-]
$t$	time to equilibrium [T]
$T$	water temperature [ $\Theta$ ]
$T_u$	turbulent intensity [-]
$T_{wu}$	co-spectral flux-transfer term of co-spectral budget [ $L^3T^{-3}$ ]
$u$	streamwise velocity component [ $LT^{-1}$ ]
$u_{rms}$	root mean square of streamwise velocity [ $LT^{-1}$ ]
$u'$	fluctuation of the streamwise velocity component [ $LT^{-1}$ ]
$u_*$	shear velocity [ $LT^{-1}$ ]
$U$	cross-sectional average velocity of the approaching flow [ $LT^{-1}$ ]
$U_c$	critical velocity for the inception of sediment motion [ $LT^{-1}$ ]

---

$v_\eta$	Kolmogorov velocity scale [LT <sup>-1</sup> ]
$V$	characteristic velocity of large-scale eddies [LT <sup>-1</sup> ]
$V_{scour}$	scour hole volume upstream to the abutment [L <sup>3</sup> ]
$w$	bed-normal velocity component [LT <sup>-1</sup> ]
$w'$	fluctuation of the bed-normal velocity component [LT <sup>-1</sup> ]
$w_d$	characteristic velocity of eddies of size $d$ [LT <sup>-1</sup> ]
$w_d^P$	characteristic velocity of eddies of size $d$ belonging to the production range [LT <sup>-1</sup> ]
$w_l$	characteristic velocity of eddies of size $l$ [LT <sup>-1</sup> ]
$\mathbf{x}$	generic point of location [L]
$x$	streamwise direction [L]
$y$	spanwise direction [L]
$y_s$	maximum scour depth [L]
$y_{se}$	maximum equilibrium scour depth [L]
$z$	bed-normal direction [L]
$z_0$	zero level of the Bazin weir [L]
$\alpha_1$	scaling function [-]
$\alpha_2$	scaling function [-]
$\Gamma$	local mean velocity gradient [T <sup>-1</sup> ]
$\delta$	Dirac delta function [-]
$\epsilon$	turbulent kinetic energy dissipation rate [L <sup>2</sup> T <sup>-3</sup> ]
$\epsilon_b$	bulk turbulent kinetic energy dissipation rate [L <sup>2</sup> T <sup>-3</sup> ]
$\eta$	Kolmogorov length scale [L]
$\eta_1$	approximate Kolmogorov length scale [L]
$\theta$	Shields parameter [-]

---

$\nu$	kinematic water viscosity [ $L^2T^{-1}$ ]
$\Pi$	velocity-pressure interaction term of co-spectral budget [ $L^3T^{-3}$ ]
$\rho$	water density [ $ML^{-3}$ ]
$\rho_s$	sediment density [ $ML^{-3}$ ]
$\sigma_g$	geometric standard deviation of the grain size distribution [-]
$\tau$	shear stress [ $ML^{-1}T^{-2}$ ]
$\tau_c$	critical shear stress [ $ML^{-1}T^{-2}$ ]
$\tau_r$	wavenumber-dependent relaxation time scale [T]
$\tau_\eta$	Kolmogorov time scale [T]
$\Phi$	velocity-spectrum tensor [ $L^3T^{-2}$ ]
$\bar{\cdot}$	time-averaged operation



# Introduction

In natural rivers, the presence of structures like bridge piers or abutments constitutes an obstruction to the flow and induces the formation of complex vortex systems, causing the generation of a local scour hole in mobile river beds. Failure of bridges due to scour at piers or abutments is a common occurrence, if the magnitude of scour is large enough to reach the pier foundations. To be specific, the presence of an obstruction to the approaching flow causes a three-dimensional flow separation. The flow impacts the structures, causing the formation of a downflow and an uplift of the free surface accompanied with a vortex (bow wave and surface roller, respectively). The downflow, interacting with the approaching flow, forms a group of helical vortices often referred to as the horseshoe vortex system or primary vortex system for pier and abutment, respectively. Downstream of the structure, wake vortices are created owing to the separation of the flow around the obstacle. The downflow and the horseshoe or primary vortex system are the main responsible for the generation of a local scour hole, as they contribute to generate strong shear stresses at the junction between the structure and the sediment bed (Fig. 1).

Quantifying the size of the expected maximum scour depth is crucial

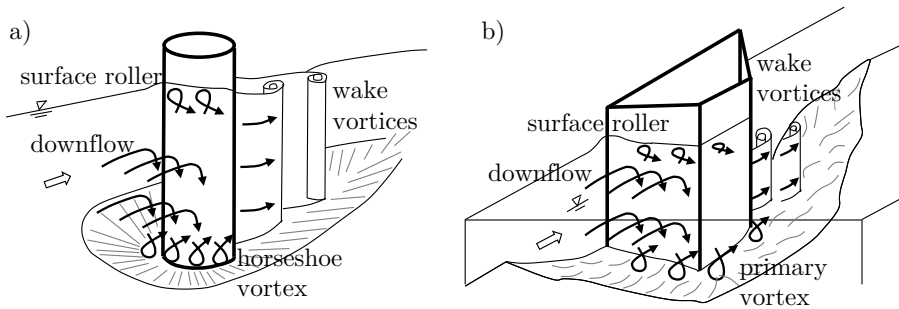


**Figure 1:** Vortex flow and scour hole around a bridge pier (a) and abutment (b).

for the design and risk assessment of many hydraulic structures (Melville & Coleman, 2000). Scour at piers and abutments has been deeply investigated in the last decades. As reported by Breusers et al. (1977), it is influenced by various parameters, which are listed as follows:

1. *parameters of the structure*: dimension, shape, number, and orientation with respect to the approaching flow direction;
2. *parameters of the sediment bed*: median particle size, particle size distribution, angle of repose, and cohesiveness;
3. *parameters of the approaching flow condition*: approaching flow velocity with respect to the critical velocity for the inception of sediment motion, approaching flow depth, shear velocity;
4. *parameters of the fluid*: mass-density, viscosity;
5. *time*, for the scour hole evolution.

Many empirical equations were proposed by various investigators to estimate the maximum scour depth at bridge piers and abutments based on

datasets from laboratory experiments and field measurements. Towards this end, researchers have mainly adopted an approach that involves coupling dimensional analysis with data-fitting procedures. In fact, assuming constant relative density of sediment and the absence of viscous effects, the maximum equilibrium scour depth  $y_{se}$  can be expressed in a non-dimensional form as (Melville & Coleman, 2000):

$$\frac{y_{se}}{a} = F\left(\frac{h}{a}, \frac{a}{d_{50}}, \sigma_g, \frac{U}{U_c}, Fr_a, Sh, Al\right) \quad (1)$$

for the case of pier, and:

$$\frac{y_{se}}{b} = F\left(\frac{h}{b}, \frac{b}{d_{50}}, \sigma_g, \frac{U}{U_c}, Fr_b, Sh, Al\right) \quad (2)$$

for the case of abutments, where  $a$  is the pier diameter,  $b$  the abutment transversal length,  $h$  the water depth,  $d_{50}$  the median sediment size,  $\sigma_g$  the geometric standard deviation of the grain size distribution,  $U$  the cross-sectional average velocity of the approaching flow,  $U_c$  the critical velocity for the inception of sediment motion,  $Fr_a = U/\sqrt{ga}$  and  $Fr_b = U/\sqrt{gb}$  the pier and abutment Froude number, respectively, and  $Sh$  and  $Al$  the parameters describing the shape of the piers or abutments and their alignment with respect to the flow direction, respectively.

This approach is associated with many shortcomings. Firstly, the problem of scour is governed by a large number of non-dimensional parameters, whose effects are difficult to identify and isolate in experiments. Secondly, empirically-derived formulae lack of almost any physical basis and, as a consequence, their validity is often limited to the experimental data they have been developed from. Therefore, since most of the available data on local

scour were obtained from laboratory experiments, it is likely that empirical formulae suffer from significant scale effects when applied to real engineering problems (Melville, 1992, 1997; Melville & Coleman, 2000).

Although the empirical approach has provided an important guide to quantifying local scour for practical applications, present advances in this research area have benefitted from the development of methodologies that are founded on physical rather than empirical basis. Recently, some researchers proposed new formulae to predict scour depths in different cases of scour mechanism (e.g., scour driven by jets, scour at bridge piers), which were derived by merging theoretical aspects (i.e., the phenomenological theory of turbulence) with empirical observations (Manes & Brocchini, 2015). The phenomenological theory of turbulence was formulated by Kolmogorov (1941) who used dimensional arguments and physical reasoning to derive scaling laws for fully-developed turbulence for specific ranges of length scales. The application of this theory has the advantage of capturing a great deal of physics while retaining simplicity (Ali & Dey, 2018). This simplicity is lost in the derivation of empirical laws as they are complicated by numerous free parameters whose physical meaning is difficult to identify.

In this work, the phenomenological theory of turbulence is used as a theoretical basis to derive scaling laws associated with the scour depth (and volume) of equilibrium.

The work is organized as follows. Chapter 1, firstly, presents a general overview of the recent application of the phenomenological theory of turbulence to hydraulic problems; secondly, using the recent results of Bonetti et al. (2017), provides a novel perspective to apply the phenomenological theory of turbulence in a correct manner. Chapter 2 provides a general pre-



dictive formula for the assessment of the maximum scour depth at bridge piers, starting from the assumption of Manes & Brocchini (2015) that the momentum transport near the sediment-water interface is dominated by eddies belonging to the inertial range and extending it to the cases in which the momentum transport is affected by eddies belonging to the dissipation and production range. Chapter 3 reports the extension of the phenomenological theory of turbulence to the phenomenon of local scouring at abutments and provides a comparison with data acquired in an original experimental campaign. The present thesis is completed with a section of Conclusions, that presents the result analysis and draws possible further developments, and a list of References.



# Chapter 1

## The phenomenological theory of turbulence and its applications in hydraulics

### 1.1 State of the art

Phenomenology of turbulence is a fascinating theory in turbulence research. Frisch's concept of the phenomenological theory of turbulence (PTT) is a «kind of shorthand system whereby the same results can be recovered in a much simpler way, although, of course, at the price of less systematic arguments» (Frisch, 1995). In the history of this subject, the pioneering work of L. F. Richardson (1922) presents the fully developed turbulent flow as an ensemble of eddies of vary sizes. The largest eddies have a size similar to the dimension of the mean flow (i.e., the flow depth for open-channel flows and the pipe diameter for pipe flows) and break-up in smaller eddies

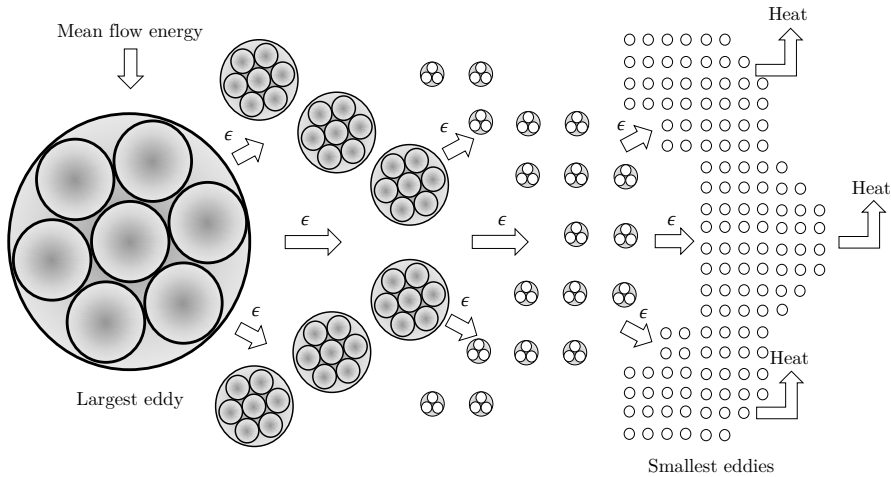


**Figure 1.1:** Energy cascade process;  $\epsilon$  is the turbulent kinetic energy dissipation rate.

owing to the fact that they are created by instabilities and are themselves unstable (Davidson, 2015). In addition, for the same reason, the eddies are transformed successively into smaller and smaller eddies with a continual cascade of energy from the large scale down to the small one. This process continues until the fluid viscosity can effectively dissipate the energy at an adequately small length scale (Fig. 1.1).

From these bases, in 1941 Kolmogorov formulated the well-known two paradigms of the fully developed turbulence that are the genesis of the PTT: 1) for fully developed turbulent flows, the turbulent kinetic energy (TKE) per unit mass is injected into the flow at scales commensurate with the largest eddies and is independent of viscosity; 2) the TKE, which is introduced at a rate  $\epsilon$ , cascades from large to small scales at the same rate, until eddies of sufficiently small scale dissipate it into internal energy still at the

same rate  $\epsilon$ . Following these paradigms, the Kolmogorov length scale  $\eta$ , i.e., the length scale at which the energy cascade begins to be influenced by viscosity, is:

$$\eta = \left( \frac{\nu^3}{\epsilon} \right)^{1/4} \quad (1.1)$$

where  $\nu$  is the kinematic fluid viscosity. The corresponding time and velocity scales are, respectively:

$$\tau_\eta = \left( \frac{\nu}{\epsilon} \right)^{1/2} \quad (1.2)$$

and

$$v_\eta = (\nu\epsilon)^{1/4}. \quad (1.3)$$

Furthermore, owing to the fact that the production of TKE occurs at large scales and is independent of viscosity, dimensional arguments suggest that:

$$\epsilon \sim \frac{V^3}{L} \quad (1.4)$$

where the  $\sim$  symbol means ‘scales as’ and  $V$  is the characteristic velocity of large eddies of size  $L$ .

Moreover, at scales  $l$  the respective characteristic velocity  $w_l$  is:

$$w_l \sim \left[ \int_{2\pi/l}^{\infty} E(k) dk \right]^{1/2} \quad (1.5)$$

where  $k$  is the wavenumber and  $E(k)$  the energy spectrum defined as follows:

$$E(k) = \frac{1}{2} \iiint_{-\infty}^{\infty} \Phi(\mathbf{k}) \delta(|\mathbf{k}| - k) d\mathbf{k} \quad (1.6)$$

where  $\mathbf{k}$  is the wavenumber vector,  $\delta$  the Dirac delta function and  $\Phi$  the

velocity-spectrum tensor, that is the Fourier transform of the two-point correlation,  $\mathbf{R}(\mathbf{r})$ , namely:

$$\Phi(\mathbf{k}) = \frac{1}{(2\pi)^3} \iiint_{-\infty}^{\infty} \exp(-i\mathbf{k} \cdot \mathbf{r}) \mathbf{R}(\mathbf{r}) d\mathbf{r} \quad (1.7)$$

where  $\mathbf{r}$  is the incremental vector,  $\mathbf{R}(\mathbf{r}) = \overline{\mathbf{u}(\mathbf{x})\mathbf{u}(\mathbf{x} + \mathbf{r})}$ ,  $\mathbf{x}$  is the generic point of location,  $\exp(-i\mathbf{k} \cdot \mathbf{r}) = \cos(\mathbf{k} \cdot \mathbf{r}) + i \sin(\mathbf{k} \cdot \mathbf{r})$  is the spatial Fourier mode and  $i$  is the imaginary unit (Pope, 2001).

In the hypothesis that the energy cascade occurs inviscidly and the energy spectrum,  $E(k) \sim \epsilon^{2/3} k^{-5/3}$ , coupling relation 1.5 and 1.4, leads to:

$$w_l \sim V \left( \frac{l}{L} \right)^{1/3} \quad (1.8)$$

which is a well-known result of Kolmogorov's theory (Frisch, 1995).

From these scaling laws, in the last decades the PTT was used in order to explain in a more physical and rigorous sense, classical formulae, diagrams and phenomena of applied hydraulics.

For example, Gioia & Bombardelli (2002) derived the Manning empirical formula by using the PTT, yielding the correct similarity exponent of Strickler scaling and justifying Manning's use of the hydraulic radius to characterise the geometry of the cross-section. Various authors used the conclusions found by Gioia & Bombardelli (2002) as the base for their conjectures. A summary of their work is reported in the following.

Gioia & Bombardelli (2005) obtained a theoretical formula via the PTT for the equilibrium scour depth of a hole generated by a 2D jet impinging on an erodible surface. The authors showed that, while the empirical formulae customarily used in applications contain numerous free exponents, the

theoretical formula contains a single one.

Bombardelli & Gioia (2006) continued the work by Gioia & Bombardelli (2005), deriving a theoretical formula for the equilibrium scour depth caused by an axisymmetric turbulent jet. Analogously to the case of Gioia & Bombardelli (2005), the resulting formula contains a single similarity exponent which, however, was never really corroborated by experimental data.

In 2006, Gioia & Chakraborty (2006) provided a theoretical explanation of the Nikuradse diagram using principles pertaining to the PTT. Among the notable results, the authors provided a link between spectral scaling in the inertial regime and flow resistance.

More recently, Manes & Brocchini (2015) investigated the scaling of the equilibrium scour depth at the base of a solid cylinder immersed within an erodible granular bed and impinged by a turbulent flow using the PTT. Manes & Brocchini (2015) also derived a predictive formula, that includes all the relevant non-dimensional parameters controlling the scouring, which, given its sound theoretical basis, should be free from scale issues.

Bonetti et al. (2017) presented a revision of the work by Gioia & Bombardelli (2002), showing that those authors employed several *ad hoc* scaling assumptions for the TKE dissipation rate  $\epsilon$ , and, although implicitly, for the mean velocity gradient adjacent to the roughness elements. Bonetti et al. (2017) questioned some assumptions made by Gioia & Bombardelli (2002) with several implications for the other works listed above and for future developments. In particular, the conclusions of Bonetti et al. (2017) will be used in this work to give a complete analysis of the problems treated in the next Chapters.

## 1.2 Revised phenomenological theory of turbulence

Bonetti et al. (2017) discussed several issues which remained unsolved in the Gioia & Bombardelli (2002) approach. In fact, some hypotheses of those authors were incompatible with the knowledge about the turbulent flow properties near the rough surface. This discussion is entirely reported in this Chapter, in order to give a general overview of the problem and to provide some necessary theoretical elements to face the arguments reported in the next Chapters.

The well-known Manning empirical equation (Manning, 1890) relates the cross-sectional averaged velocity,  $V$ , to the hydraulics radius,  $R$ , and the energy grade slope,  $S$ , through a roughness coefficient,  $n$ , as follows:

$$V = \frac{1}{n} R^{2/3} S^{1/2}. \quad (1.9)$$

In 2002, Gioia & Bombardelli presented a theoretical derivation the Manning formula. More importantly, using scaling arguments about the size of the eddies responsible of the momentum transport near roughness elements of size  $d$ , they provided a theoretical link between the Strickler scaling, i.e.,  $n \sim d^{1/6}$ , and the Kolmogorov  $k^{-5/3}$  inertial range scaling.

The unsolved issues of Gioia & Bombardelli (2002), reported in Bonetti et al. (2017), are summarized as follows: 1) they assumed that the eddies whose size exceeds the roughness dimension  $d$  do not contribute appreciably to the vertical velocity component near the roughness elements, but this hypothesis is not supported by experimental evidence (Raupach et al., 1991); 2) they considered that the Kolmogorov scaling (Kolmogorov, 1941) holds in proximity to the roughness surface, where the hypotheses of isotropy and



homogeneity of turbulence are not verified (for open-channel flows, see e.g., Poggi et al. (2002)); 3) they assumed that  $\epsilon$  scales as  $V^3/R$  and that the associated scaling constant is independent of the relative roughness,  $d/R$ , but this assumptions are incorrect, considering the results about the flow characteristics (Raupach et al., 1991). These issues are extensively discussed in §1.2, reporting the consideration of Bonetti et al. (2017).

The theoretical approach by Gioia & Bombardelli (2002) is now reported and discussed in view of the aforementioned criticisms. In a steady and uniform open-channel flow, the total shear stress  $\tau$  acting along the wetted perimeter can be computed from momentum balance principles, as follows:

$$\tau = \rho g R S \quad (1.10)$$

where  $\rho$  is the fluid density and  $g$  the gravitational acceleration. Bonetti et al. (2017) considered, for the sake of simplicity, an open channel with a rectangular cross-section having a water depth  $h$  and a breadth  $B$  and the roughness elements of size  $d$  uniformly distributed along the channel bed and walls. In rough flow condition,  $\tau$ , which is maximum along the direction perpendicular to the bed, can be also expressed as follows:

$$\tau = \rho u_*^2 \sim \rho \max(-\overline{u'w'}) \quad (1.11)$$

where  $u_*$  is the shear velocity,  $u'$  and  $w'$  are the fluctuations of the stream-wise,  $u$ , and bed-normal,  $w$ , velocity components, respectively, and the over-bar represents time averaging.

Starting from Eqs. 1.10 and 1.11, Gioia & Bombardelli (2002) analysed the dominant velocity scales that contribute to  $\max(-\overline{u'w'})$  at the top of the

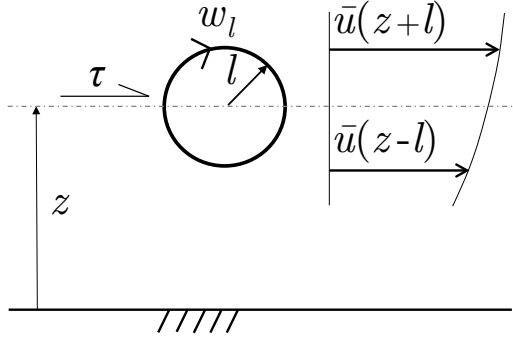


**Figure 1.2:** Sketch for the derivation of the turbulent shear stress.

roughness surface. In particular, they assumed that  $u' \sim V$ , as supported in a subsequent paper (Gioia et al., 2010). Following Gioia & Bombardelli (2002), at a distance  $z$  from the bed, the turbulent shear stresses produced by eddies at this elevation, transfer momentum across this zone (Fig. 1.2).

Thus, an eddy of size  $l$  transports fluid having horizontal momentum per unit volume of about  $\rho \bar{u}(z+l)$  and fluid with low horizontal momentum per unit volume equal to  $\rho \bar{u}(z-l)$ ; where  $\bar{u}(z \pm l)$  is the mean velocity at a distance  $z \pm l$  from the wall. Consequently, the eddy spans a momentum contrast of  $\rho [\bar{u}(z+l) - \bar{u}(z-l)] \approx 2\rho l d\bar{u}/dz$ . The rate of momentum transfer across the horizontal plane at elevation  $z$  is set by the normal velocity component, i.e., the eddy velocity,  $w_l$ . Therefore, the turbulent shear stress produced by an eddy of size  $l$  scales as:

$$\tau \sim \rho l \frac{d\bar{u}}{dz} w_l, \quad (1.12)$$

Hence,  $\tau(z) = -\overline{\rho u' w'} \sim \rho l (d\bar{u}/dz) w_l$ . At the top of the roughness elements,  $l \sim d$  and  $d\bar{u}/dz \sim V/d$ ; consequently,  $u' \sim V$ , as shown in Fig.

1.3. With respect to  $w'$ , Gioia & Bombardelli (2002) conjectured that, when the relative roughness is small, turbulent eddies smaller than  $d$  fit in the space between successive roughness elements. However, when these eddies are smaller than the size of the roughness elements, their characteristic velocities are negligible compared with the characteristic velocity of the eddies of size  $d$  (i.e.,  $w_d$ ). Thus, the eddies that contribute to the momentum exchange have size equal to  $d$  (i.e.,  $w_l \sim w_d$ ). From Eq. 1.11 and considering the Kolmogorov scaling for the inertial range [i.e.,  $w_d \sim (\epsilon d)^{1/3}$ ]; the parameter  $\epsilon$  can be interpreted as the TKE dissipation rate at the top of the roughness elements, namely,  $\epsilon(z = d)$ , one obtains:

$$\tau = \rho \max(-\overline{u'w'}) \sim \rho V w_d \sim \rho V (\epsilon d)^{1/3}. \quad (1.13)$$

However, Gioia & Bombardelli (2002) claimed that the local  $\epsilon$  scales as the bulk dissipation rate,  $\epsilon_b$ . This implies that:

$$\epsilon \sim \epsilon_b \sim \frac{V^3}{R}. \quad (1.14)$$

Combining relations 1.13 and 1.14, the Manning equation with the Strickler scaling was determined by Gioia & Bombardelli (2002) as follows:

$$V \sim \left(\frac{d}{R}\right)^{-1/6} \sqrt{gRS} \quad (1.15)$$

where the Strickler scaling is implicitly introduced with  $n \sim d^{1/6}$ .

The derivation by Gioia & Bombardelli (2002) contains some implicit assumptions which are discussed by Bonetti et al. (2017) and presented herein. The first assumption is relative to the estimation of  $u' \sim V$  or

implicitly the local mean velocity gradient  $\Gamma(z) = d\bar{u}(z)/dz \sim V/d$ . In particular, Fig. 1.3 provides a possible reason that, near the surface of the roughness elements,  $\Gamma$  results:

$$\Gamma(z = d) \sim \frac{V - 0}{d}, \quad (1.16)$$

where  $\bar{u} = 0$  within the roughness elements and the thickness of the roughness layer scales with  $d$ . Hence, Gioia & Bombardelli (2002) implicitly assumed that the proportionality constant  $\alpha_1$  that links  $\Gamma$  to  $V/d$  (i.e.,  $\Gamma(z = d) = \alpha_1 V/d$ ) is independent from  $d/R$ . This hypothesis is questionable in the vicinity of the roughness elements. At this location (i.e.,  $z \sim d$ ), the local mean velocity gradient can be assumed, as reported by Bonetti et al. (2017), to scale as  $d\bar{u}(z)/dz \sim u_*/d$ . This result, combined with relation 1.16, implies that  $\alpha_1$  must scale as the square root of the friction factor,  $f_d$  (i.e.,  $\alpha_1 \sim f_d^{1/2}$ ), which notoriously depends on the relative roughness,  $d/R$ , in turbulent flows.

The second assumption of Gioia & Bombardelli (2002) is related to the estimation of  $\epsilon$  at elevation  $z = d$ . With regards to this assumption, the local dissipation rate at the roughness tops can be determined as:

$$\epsilon(z = d) = \frac{\alpha_2^3 V^3}{R} \quad (1.17)$$

where  $\alpha_2$  is an *ad hoc* scaling function that links the local to the bulk dissipation rate at given  $z$  and  $d/R$ . Now, the local dissipation rate is  $\epsilon(z = d) = -\overline{u'w'}d\bar{u}(z)/dz \sim u_*^3/d$ , because  $d\bar{u}(z)/dz \sim u_*/d$ . Inserting this relation in relation 1.17, we obtain that  $\alpha_2 \sim (d/R)^{1/3} f_d^{1/2}$ , which also depends on  $d/R$ . Repeating the derivation by Gioia & Bombardelli (2002),

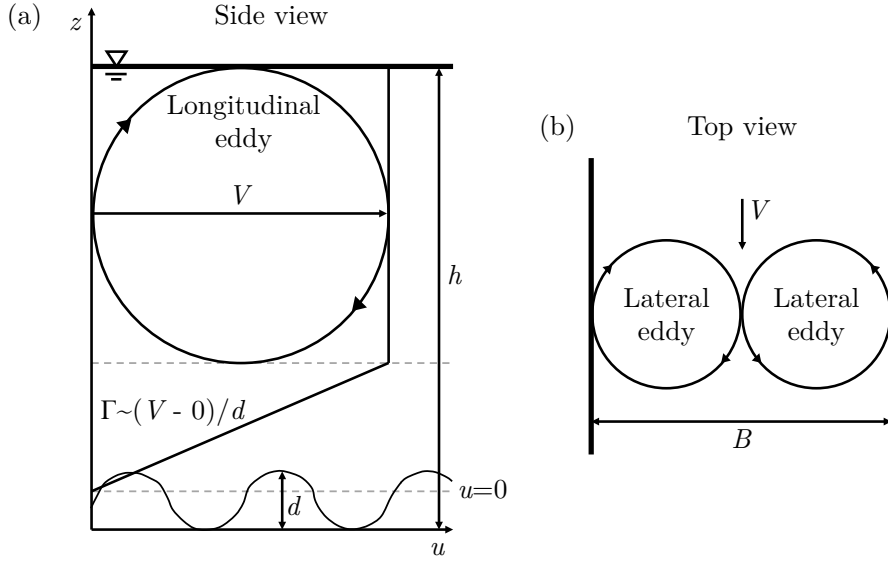


**Figure 1.3:** The link between  $\Gamma$  and the bulk variables  $V$ ,  $R$  and the roughness size  $d$  for a steady and uniform flow in an open channel with breadth  $B$  and water depth  $h$ .

the shear stress results:

$$\tau \sim \rho g R S \sim \rho V (\epsilon d)^{1/3} \sim \alpha_1 \alpha_2 \rho V^2 \left( \frac{d}{R} \right)^{1/3} \quad (1.18)$$

and, consequently:

$$V \sim (\alpha_1 \alpha_2)^{-1/2} \left( \frac{d}{R} \right)^{-1/6} \sqrt{g R S}. \quad (1.19)$$

The Strickler scaling in 1.19 is determined only if the product  $\alpha_1 \alpha_2$  is independent of  $d$  and/or  $R$ . From the previous algebraic steps,  $\alpha_1 \alpha_2 \sim (d/R)^{-1/3} f_d$ , which becomes constant only if the Strickler scaling is verified (i.e.,  $f_d \sim (d/R)^{1/3}$ ). As reported by Bonetti et al. (2017), this leads to a

circular argument: «Manning formula and the Strickler scaling can only be recovered if  $\alpha_1\alpha_2$  is a constant independent of  $d/R$ , but  $\alpha_1\alpha_2$  is independent of  $d/R$  only when the Strickler scaling applies».

Bonetti et al. (2017) concluded that the derivation of the Manning formula can be re-examined using an alternative approach based on the co-spectral budget (CSB) model, which allows relaxing many of the assumptions made by Gioia & Bombardelli (2002). In the next section, the CSB approach by Bonetti et al. (2017) is deepened with original considerations useful for the present work.

### 1.3 Co-spectral budget model and its developments

The momentum turbulent flux at a generic elevation  $z > d$ , at which the attached eddy hypothesis is valid (Bonetti et al., 2017), can be related to the integral of the co-spectrum as:

$$\overline{u'w'}(z) = - \int_0^\infty F_{wu}(k) dk \quad (1.20)$$

where  $F_{wu}$  is the co-spectrum between  $u'$  and  $w'$  (i.e., the real part of the Fourier transform of the cross-correlation function between  $u'$  and  $w'$ ). In the vicinity of the roughness elements,  $-\overline{u'w'}(z) \approx ghS \approx u_*^2$ . The related budget was given by Katul et al. (2013) and Katul & Manes (2014), as follows:

$$\frac{\partial F_{wu}(k)}{\partial t} + 2\nu k^2 F_{wu}(k) = G(k), \quad (1.21)$$

where  $t$  is time and:

$$G(k) = P_{wu}(k) + T_{wu}(k) + \Pi(k) \quad (1.22)$$

$P_{wu}(k) = \Gamma E_{ww}(k)$  being the covariance production term,  $E_{ww}(k)$  the turbulent energy spectrum of the vertical velocity,  $T_{wu}(k)$  the co-spectral flux-transfer term and  $\Pi(k)$  the velocity-pressure interaction term, which acts to decorrelate  $u'$  and  $w'$  (Pope, 2001).

Coupling Eqs. 1.21 and 1.22 and assuming inviscid (i.e.,  $2\nu k^2 F_{wu}(k)$  negligible) and steady flow conditions (i.e.,  $\partial F_{wu}(k)/\partial t$  and  $T_{wu}(k)$  negligible), the budget equation simplifies as:

$$\Gamma E_{ww}(k) + \Pi(k) = 0. \quad (1.23)$$

If the Rotta model (Rotta, 1962) is invoked for  $\Pi(k)$ :

$$\Pi(k) = -C_R \frac{F_{wu}(k)}{\tau_r(k)} - C_I P_{wu}(k), \quad (1.24)$$

where  $\tau_r(k) = \epsilon^{-1/3} k^{-2/3}$  is a wavenumber-dependent relaxation time scale assumed to vary only with  $k$  and  $\epsilon$ ,  $C_R \approx 1.8$  and  $C_I = 3/5$  (Pope, 2001), Eq. 1.23 becomes:

$$F_{wu}(k) = \frac{1}{A_\pi} \Gamma \epsilon^{-1/3} E_{ww}(k) k^{-2/3} \quad (1.25)$$

where  $A_\pi = C_R/(1 - C_I) \approx 4.5$ .

Combining Eqs. 1.20 and 1.25:

$$|\Gamma| \epsilon^{-1/3} = A_\pi \frac{-\overline{u'w'}}{I_k}, \quad (1.26)$$

where:

$$I_k = \int_0^{\infty} k^{-2/3} E_{ww}(k) dk \quad (1.27)$$

is an integral depending on  $k$ .

Assuming, as in Bonetti et al. (2017), a characteristic simplified spectrum shape (Fig. 1.4) and neglecting the exponential cut-off to viscous corrections (Pope, 2001), Eq. 1.26 becomes:

$$|\Gamma| \epsilon^{-1/3} = \frac{A_\pi \tau / \rho}{I_k}, \quad (1.28)$$

where:

$$I_k = \frac{E_{Kol}(K_a)}{K_c^p} \int_0^{K_c} k^p k^{-2/3} dk + E_{Kol}(K_a) \int_{K_c}^{K_a} k^{-2/3} dk + \int_{K_a}^{\infty} k^{-2/3} E_{Kol}(k) dk, \quad (1.29)$$

$K_c$  and  $K_a$  being the wavenumbers of the same order of the reciprocal of the large scale eddies (i.e., scaling as  $R$  or  $h$ ) and the sediment diameter  $d$ , respectively,  $E_{Kol} = C_0 \epsilon^{2/3} k^{-5/3}$  is the Kolmogorov spectrum,  $C_0$  is the universal Kolmogorov constant (Sreenivasan, 1995) and  $p$  the slope of  $E_{ww}/E_{Kol}(K_a)$  when  $k < K_c$ ;  $p \approx 8/3$  as suggested by Pope (2001).

From this equation Bonetti et al. (2017), firstly, assuming a simplified shape for the spectrum  $E_{ww}$  contained in Eq. 1.28, demonstrated that the CSB model allows deriving the Manning equation to be derived. Secondly, to generalize this approach, numerical solutions of the CSB model along the entire flow depth using different spectral shapes were carried out for a wide range of  $d/R$ . The derived equation furnish  $n$  values that agree with the



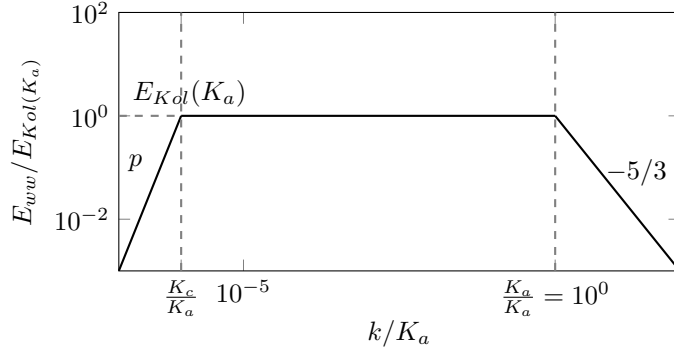


**Figure 1.4:** Scheme of the idealized dimensionless vertical velocity spectrum  $E_{ww}/E_{Kol}(K_a)$ .

values reported in the literature over seven decades of  $d$  variations. The numerical solutions of the CSB reproduce the Nikuradse data in the fully rough regime, thereby confirming that the Strickler scaling represents only an approximate fit for the friction factor associated with granular roughness.

In order to provide a complete analysis of the problems, presented in the next Chapters, Eq. 1.28 is further analysed. In particular, for the sake of generality, the power-law spectrum is complemented with an exponential cut-off to take into account viscous (i.e., dissipation range) effects, so that Eq. 1.29 becomes:

$$I_k = \frac{E_{Kol}(K_a)}{K_c^p} \int_0^{K_c} k^p k^{-2/3} dk + E_{Kol}(K_a) \int_{K_c}^{K_a} k^{-2/3} dk + \int_{K_a}^{\infty} k^{-2/3} E_{Kol}(k) \exp(-\beta k \eta) dk, \quad (1.30)$$

with  $K_a \sim 1/(d + 5\eta)$  and  $|\Gamma| = \alpha_1 V/(d + 5\eta)$ , where, according to Gioia & Chakraborty (2006),  $5\eta$  is the viscous sublayer thickness and  $d + 5\eta$  the size

of the largest eddy that fits the troughs among successive roughness elements covered by the viscous sublayer and  $\exp(-\beta k\eta)$  determines the shape of the dissipation range, where  $\beta = 2.1$  is a positive constant. From Eq. 1.28, the friction factor  $f_d$  results:

$$f_d = \frac{\tau}{\rho V^2} = \left[ \frac{C_o \epsilon^{2/3} K_a^{-5/3}}{K_c^p} \int_0^{K_c} k^{p-2/3} dk + \right. \\ \left. + C_o \epsilon^{2/3} K_a^{-5/3} \int_{K_c}^{K_a} k^{-2/3} dk + \right. \\ \left. + C_o \epsilon^{2/3} \int_{K_a}^{\infty} k^{-2/3} k^{-5/3} \exp(-\beta k\eta) dk \right] \frac{|\Gamma| \epsilon^{-1/3}}{A_\pi V^2}, \quad (1.31)$$

with  $E_{Kol}(k) = C_o \epsilon^{2/3} k^{-5/3}$ . Therefore:

$$f_d = \left[ \frac{K_a^{-5/3}}{K_c^p} \int_0^{K_c} k^{p-2/3} dk + K_a^{-5/3} \int_{K_c}^{K_a} k^{-2/3} dk + \right. \\ \left. + \int_{K_a}^{\infty} k^{-7/3} \exp(-\beta k\eta) dk \right] \frac{C_o |\Gamma| \epsilon^{1/3}}{A_\pi V^2}. \quad (1.32)$$

Since  $|\Gamma| = \alpha_1 V / (d + 5\eta)$  and  $\epsilon = \alpha_2^3 V^3 / R$ , Eq. 1.32 can be re-written as follows:

$$f_d = \left[ -\frac{3p}{p+1/3} (d+5\eta)^{5/3} R^{-1/3} + 3(d+5\eta)^{4/3} + \right. \\ \left. + \int_{1/(d+5\eta)}^{\infty} k^{-7/3} \exp(-\beta k\eta) dk \right] \frac{C_o \alpha_1 \alpha_2 (d+5\eta)^{-1} R^{-1/3}}{A_\pi}; \quad (1.33)$$

hence:

$$\begin{aligned}
f_d = & \left\{ -\frac{3p}{p+1/3} \left[ \left( \frac{d}{R} \right)^{2/3} + \left( 5 \frac{\eta}{R} \right)^{2/3} \right] + \right. \\
& \left. + 3 \left[ \left( \frac{d}{R} \right)^{1/3} + \left( 5 \frac{\eta}{R} \right)^{1/3} \right] + \right. \\
& \left. + (d+5\eta)^{-1} R^{-1/3} \int_{1/(d+5\eta)}^{\infty} k^{-7/3} \exp(-\beta k \eta) dk \right\} \frac{C_0 \alpha_1 \alpha_2}{A_\pi}
\end{aligned} \tag{1.34}$$

where:

$$\begin{aligned}
\frac{\eta}{R} = \left( \frac{\nu^3}{\epsilon} \right)^{1/4} \frac{1}{R} = \left( \frac{\nu^3 R}{\alpha_2^3 V^3} \right)^{1/4} \frac{1}{R} = \frac{1}{\alpha_2^{3/4}} \frac{\nu^{3/4}}{V^{3/4} R^{3/4}} = \\
= \alpha_2^{-3/4} Re^{-3/4},
\end{aligned} \tag{1.35}$$

$Re = RV/\nu$  being the Reynolds number, and:

$$\begin{aligned}
\frac{\eta}{d} = \left( \frac{\nu^3}{\epsilon} \right)^{1/4} \frac{1}{d} = \left( \frac{\nu^3 d}{u_*^3} \right)^{1/4} \frac{1}{d} = \frac{\nu^{3/4}}{u_*^{3/4} d^{3/4}} = \\
= \frac{R^{3/4}}{d} \frac{V^{3/4}}{u_*} \frac{\nu^{3/4}}{V^{3/4} R^{3/4}} = \left( \frac{d}{R} \right)^{-3/4} \left( \frac{u_*}{V} \right)^{-3/4} Re^{-3/4},
\end{aligned} \tag{1.36}$$

consequently:

$$\begin{aligned}
f_d = & \left\{ -\frac{3p}{p+1/3} \left[ \left( \frac{d}{R} \right)^{2/3} + 5^{2/3} \alpha_2^{-1/2} Re^{-1/2} \right] + \right. \\
& + 3 \left[ \left( \frac{d}{R} \right)^{1/3} + 5^{1/3} \alpha_2^{-1/4} Re^{-1/4} \right] + \\
& \left. + (d+5\eta)^{-1} R^{-1/3} \int_{1/(d+5\eta)}^{\infty} k^{-7/3} \exp(-\beta k \eta) dk \right\} \frac{C_0 \alpha_1 \alpha_2}{A_\pi}
\end{aligned} \tag{1.37}$$

and, after substituting the integration variable with  $x = k\eta$ , the integral of the previous equation becomes:

$$\int_{\eta/(d+5\eta)}^{\infty} \left( \frac{x}{\eta} \right)^{-7/3} \exp(-\beta x) \frac{1}{\eta} dx = \eta^{4/3} \int_{1/(d/\eta+5)}^{\infty} x^{-7/3} \exp(-\beta x) dx. \tag{1.38}$$

Hence, the friction factor can be computed as:

$$\begin{aligned}
f_d = & \left\{ -\frac{3p}{p+1/3} \left[ \left( \frac{d}{R} \right)^{2/3} + 5^{2/3} \alpha_2^{-1/2} Re^{-1/2} \right] + \right. \\
& + 3 \left[ \left( \frac{d}{R} \right)^{1/3} + 5^{1/3} \alpha_2^{-1/4} Re^{-1/4} \right] + \\
& \left. + (d+5\eta)^{-1} R^{-1/3} \eta^{4/3} \int_{1/(d/\eta+5)}^{\infty} x^{-7/3} \exp(-\beta x) dx \right\} \frac{C_0 \alpha_1 \alpha_2}{A_\pi};
\end{aligned} \tag{1.39}$$

therefore:

$$\begin{aligned}
f_d = & \left\{ -\frac{3p}{p+1/3} \left[ \left( \frac{d}{R} \right)^{2/3} + 5^{2/3} \alpha_2^{-1/2} Re^{-1/2} \right] + \right. \\
& \left. + 3 \left[ \left( \frac{d}{R} \right)^{1/3} + 5^{1/3} \alpha_2^{-1/4} Re^{-1/4} \right] + \right. \\
& \left. + \frac{\eta}{d+5\eta} \left( \frac{\eta}{R} \right)^{1/3} \int_{1/(f_d^{3/8} (\frac{d}{R})^{3/4} Re^{3/4+5})}^{\infty} x^{-7/3} \exp(-\beta x) dx \right\} \frac{C_0 \alpha_1 \alpha_2}{A_\pi}.
\end{aligned} \tag{1.40}$$

Consequently:

$$\begin{aligned}
f_d = & \left\{ -\frac{3p}{p+1/3} \left[ \left( \frac{d}{R} \right)^{2/3} + 5^{2/3} \alpha_2^{-1/2} Re^{-1/2} \right] + \right. \\
& \left. + 3 \left[ \left( \frac{d}{R} \right)^{1/3} + 5^{1/3} \alpha_2^{-1/4} Re^{-1/4} \right] + \right. \\
& \left. + \frac{1}{f_d^{3/8} (\frac{d}{R})^{3/4} Re^{3/4+5}} Re^{-1/4} \int_{1/(f_d^{3/8} (\frac{d}{R})^{3/4} Re^{3/4+5})}^{\infty} x^{-7/3} \exp(-\beta x) dx \right\} \frac{C_0 \alpha_1 \alpha_2}{A_\pi}
\end{aligned} \tag{1.41}$$

and, finally:

$$\begin{aligned}
f_d = & \left\{ -\frac{3p}{p+1/3} \left[ \left( \frac{d}{R} \right)^{2/3} + 5^{2/3} \alpha_2^{-1/2} Re^{-1/2} \right] + \right. \\
& \left. + 3 \left[ \left( \frac{d}{R} \right)^{1/3} + 5^{1/3} \alpha_2^{-1/4} Re^{-1/4} \right] + \right. \\
& \left. + \frac{1}{f_d^{3/8} \left( \frac{d}{R} \right)^{3/4} Re + 5Re^{1/4}} \int_{1/(f_d^{3/8} \left( \frac{d}{R} \right)^{3/4} Re^{3/4+5})}^{\infty} x^{-7/3} \exp(-\beta x) dx \right\} \frac{C_0 \alpha_1 \alpha_2}{A_\pi}.
\end{aligned} \tag{1.42}$$

From Eq. 1.42,  $\alpha_1 \alpha_2$  results:

$$\alpha_1 \alpha_2 = \frac{A_\pi}{C_0} \frac{f_d}{f_* \left( Re, \frac{d}{R}, f_d, \alpha_2 \right)}, \tag{1.43}$$

where:

$$\begin{aligned}
f_* \left( Re, \frac{d}{R}, \alpha_2 \right) = & \left\{ -\frac{3p}{p+1/3} \left[ \left( \frac{d}{R} \right)^{2/3} + 5^{2/3} \alpha_2^{-1/2} Re^{-1/2} \right] + \right. \\
& \left. + 3 \left[ \left( \frac{d}{R} \right)^{1/3} + 5^{1/3} \alpha_2^{-1/4} Re^{-1/4} \right] + \right. \\
& \left. + \frac{1}{f_d^{3/8} \left( \frac{d}{R} \right)^{3/4} Re + 5Re^{1/4}} \int_{1/f_d^{3/8} \left( \frac{d}{R} \right)^{3/4} Re^{3/4+5})}^{\infty} x^{-7/3} \exp(-\beta x) dx \right\},
\end{aligned} \tag{1.44}$$

$f_*$  being a function of  $Re$ ,  $d/R$ ,  $f_d$  and  $\alpha_2$  and, hence, of  $Re$ ,  $d/R$  and  $\alpha_2$ .

Considering that  $f_d$  is dependent on  $Re$  and  $d/R$ , from Eq. 1.43 one obtains:

$$\alpha_1 \alpha_2 = \frac{A_\pi}{C_0} \frac{f_d}{f_* \left( Re, \frac{d}{R}, \alpha_2 \right)}. \tag{1.45}$$

From Eq. 1.45 it is possible to see that the product between  $\alpha_1$  and  $\alpha_2$  depends on  $Re$ ,  $d/R$  and, implicitly,  $\alpha_2$ . In addition, the analysis indicates that the product  $\alpha_1\alpha_2$  is independent on the choice of the  $E_{ww}$  shape in the low wavenumber branch. Despite the fact that Eq. 1.45 does not have an analytical solution, important considerations can be drawn. In particular, Eq. 1.45 is valid for all the Nikuradse turbulent flow regimes (i.e., smooth, transitional and rough) and, under specific modifications, at least, it is possible to consider the extreme regimes (i.e., smooth and rough) separately.

### 1.3.1 Rough turbulent flow case

In the rough turbulent flow case, the Kolmogorov length scale is negligible with respect to the sediment size (i.e.,  $\eta/d \approx 0$ ) and Eq. 1.32 becomes:

$$f_d = \left[ \frac{C_o \epsilon^{2/3} K_a^{-5/3}}{K_c^p} \int_0^{K_c} k^{p-2/3} dk + C_o \epsilon^{2/3} K_a^{-5/3} \int_{K_c}^{K_a} k^{-2/3} dk \right] \frac{|\Gamma| \epsilon^{-1/3}}{A_\pi V^2}, \quad (1.46)$$

with  $K_a \sim 1/d$ , where  $d$  identified the elevation at which the logarithmic region in the rough case starts (Manes et al., 2007), and, hence, at which the attached eddy hypothesis is valid (Bonetti et al., 2017). After some algebraic steps, the friction factor results:

$$f_d = \left[ -\frac{3p}{p+1/3} \left(\frac{d}{R}\right)^{2/3} + \frac{15}{4} \left(\frac{d}{R}\right)^{1/3} \right] \frac{C_0 \alpha_1 \alpha_2}{A_\pi}, \quad (1.47)$$

and, considering  $p \approx 8/3$  (Pope, 2001),  $\alpha_1\alpha_2$  can be computed as follows:

$$\alpha_1\alpha_2 = \frac{A_\pi}{C_0} \frac{f_d}{\left[-\frac{8}{3} \left(\frac{d}{R}\right)^{2/3} + \frac{15}{4} \left(\frac{d}{R}\right)^{1/3}\right]}. \quad (1.48)$$

Considering the following formula for the assessment of the friction factor in rough pipes (Nikuradse, 1933):

$$f_d = \frac{1}{\left(1.74 + 2 \log \frac{d}{R}\right)^2}, \quad (1.49)$$

$\alpha_1\alpha_2$  can be calculated as a function of  $d/R$ , as shown in Fig. 1.5. Some speculation from this result can be done. From Eq. 1.47, the friction factor  $f_d$  is the sum of a term scaling as  $(d/R)^{1/3}$  and its square (i.e.,  $(d/R)^{2/3}$ ). Assuming  $\alpha_1\alpha_2$  as a constant and low relative roughness ( $d/R \ll 1$ ), then  $f_d \sim (d/R)^{1/3}$  and the Strickler scaling is recovered. Hence, deviations from the Strickler scaling can be ascribed to a combined effect of high relative roughness, at which  $(d/R)^{2/3}$  is no longer negligible, and  $\alpha_1\alpha_2$ . From Fig. 1.5 it is possible to see that the product  $\alpha_1\alpha_2$  is approximately constant for values of  $d/R$  less than 0.02, with a variation of about 5%. On the contrary, at high values of the relative roughness,  $\alpha_1\alpha_2$  varies of about 25%, within the range of data explored by Nikuradse as used in Fig. 1.5. Hence, it is possible to conclude that, for low values of the ratio between  $d$  and  $R$ , the term  $(d/R)^{2/3}$  is negligible with respect to  $(d/R)^{1/3}$  and there is no substantial variation of  $\alpha_1\alpha_2$ ; consequently, this is the condition to identify by the range where the Strickler scaling can be considered applicable.



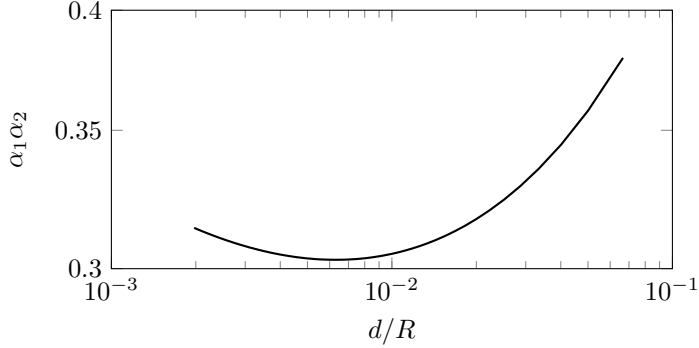


**Figure 1.5:**  $\alpha_1\alpha_2$  as a function of  $d/R$  in the rough turbulent flow case.

### 1.3.2 Smooth turbulent flow case

In the smooth turbulent flow case the roughness size  $d$  is negligible with respect to the largest eddy size (i.e.,  $d/R \approx 0$ ). Therefore, Eq. 1.32 becomes:

$$\begin{aligned}
 f_d = \frac{\tau}{\rho V^2} = & \left[ \frac{C_o \epsilon^{2/3} K_a^{-5/3}}{K_c^p} \int_0^{K_c} k^{p-2/3} dk + \right. \\
 & + C_o \epsilon^{2/3} K_a^{-5/3} \int_{K_c}^{K_a} k^{-2/3} dk + \\
 & \left. + C_o \epsilon^{2/3} \int_{K_a}^{\infty} k^{-2/3} k^{-5/3} \exp(-\beta k \eta) dk \right] \frac{|\Gamma| \epsilon^{-1/3}}{A_\pi V^2},
 \end{aligned} \tag{1.50}$$

with  $K_a \sim 1/(30\eta)$ , where  $30\eta$  identifies the elevation at which the logarithmic region in the smooth case starts (Nezu & Nakagawa, 1993), and, hence, at which the attached eddy hypothesis is valid (Bonetti et al., 2017). After some algebraic steps, the friction factor results:

$$f_d = \left[ -\frac{3p}{p+1/3} \alpha_2^{-1/2} Re^{-1/2} + \alpha_2^{-1/4} Re^{-1/4} \left( 3 \cdot 30^{4/3} + \int_{1/30}^{\infty} x^{-7/3} \exp(-\beta x) dx \right) \right] \frac{C_0 \alpha_1 \alpha_2}{30 A_\pi} \quad (1.51)$$

and, considering  $p \approx 8/3$  (Pope, 2001),  $\alpha_1 \alpha_2$  can be computed as follows:

$$\alpha_1 \alpha_2 = \frac{30 A_\pi}{C_0} \frac{f_d}{f_*(\alpha_2, Re)}, \quad (1.52)$$

where:

$$f_*(\alpha_2, Re) = -\frac{8}{3} \alpha_2^{-1/2} Re^{-1/2} + \alpha_2^{-1/4} Re^{-1/4} \left( 3 \cdot 30^{4/3} + \int_{1/30}^{\infty} x^{-7/3} \exp(-\beta x) dx \right). \quad (1.53)$$

Analogously to the rough turbulent flow case,  $f_d$  depends on the sum of a term scaling as  $Re^{-1/4}$  and its square,  $Re^{-1/2}$ . Therefore, the term  $Re^{-1/2}$  is negligible with respect to  $Re^{-1/4}$  and Eqs. 1.51 and 1.52 become, respectively:

$$f_d = \left[ -\frac{8}{3} Re^{-1/4} \left( 3 \cdot 30^{4/3} + \int_{1/30}^{\infty} x^{-7/3} \exp(-\beta x) dx \right) \right] \frac{C_0 \alpha_1 \alpha_2^{3/4}}{30 A_\pi} \quad (1.54)$$

and:

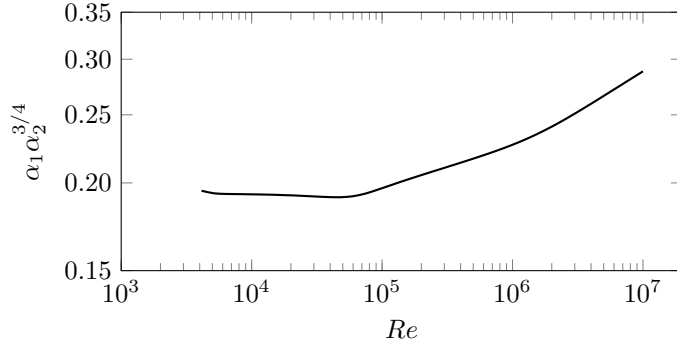


**Figure 1.6:**  $\alpha_1 \alpha_2^{3/4}$  as a function of  $Re$  in the smooth turbulent flow case.

$$\alpha_1 \alpha_2^{3/4} = \frac{30A\pi}{C_0} \frac{f_d}{\left[ Re^{-1/4} \left( 3 \cdot 30^{4/3} + \int_{1/30}^{\infty} x^{-7/3} \exp(-\beta x) dx \right) \right]}. \quad (1.55)$$

In Eq. 1.54 the friction factor,  $f_d$ , assuming that the second-order term (i.e.,  $Re^{-1/2}$ ) is negligible and  $\alpha_1 \alpha_2^{3/4}$  is not a function of  $Re$ , follows the Blasius scaling, namely (Nikuradse, 1933):

$$f_d \sim Re^{-1/4}, \quad (1.56)$$

which is known to be valid for  $Re < 10^5$ .

The dependence of  $\alpha_1 \alpha_2^{3/4}$  on  $Re$  is now explored using the original experimental data taken by Nikuradse and the Princeton group as interpolated by Yang & Joseph (2009) in Eq. 6, not reported here for the sake of brevity, of their paper on the derivation of friction factor predictive formulae for laminar, transition and turbulent flow in smooth and rough pipes.

## 1.4 Summary

The results presented herein have a lot of implications. The Gioia & Bombardelli (2002) theory, that is at the base of all the recent applications of the PTT in hydraulics, despite its significance, simplicity, elegance and appeal has some shortcomings. Bonetti et al. (2017) demonstrated that, assuming that the mean TKE dissipation rate and  $V^3/R$  are linked by a scaling function,  $\alpha_2$  is not a constant. Secondly, the mean velocity gradient at the roughness tops does not scale as  $V/d$ , as reported by Gioia & Bombardelli (2002), and the associated scaling function,  $\alpha_1$ , is also not a constant but a function of  $d/R$ .

In this Chapter, the theoretical developments and criticism to Gioia & Bombardelli (2002) are presented and extended by relaxing the assumption of fully rough conditions.

Besides providing interesting results on the origin of the Blasius and Strickler scaling, this Chapter also provides a complete theoretical framework that will be used in the next Chapter that deals with local scouring around cylindrical piers and abutments.

## Chapter 2

# Near-bed eddy scales and clear-water local scouring around vertical cylinders

### 2.1 Introduction

As is known, when an open-channel flow impinges on a vertical obstacle (e.g. a bridge pier), a three-dimensional vortex system forms and triggers an erosion phenomenon in the vicinity of the sediment bed, which is usually referred to as local scouring. Quantifying the size of the local scour hole is crucial for the design and risk assessment of many hydraulic structures (Melville & Coleman, 2000). Therefore, over the past 50 years, a lot of research has been oriented to find a predictive formula that allowed for the evaluation of the scour depth (Dey, 2014) for a given set of variables (geometry, position and orientation of the structure with respect to the flow

direction, sediment size and design flow conditions). In particular, efforts have been targeted to work out predictive formulae for the so-called equilibrium scour depth, which is defined as the maximum depth of the scour hole forms at the base of a structure impinged by a steady flow, after that the erosion process has reached an equilibrium phase. Towards this end, researchers have mainly adopted an empirical approach that involves coupling dimensional analysis with data-fitting procedures. Unfortunately, this approach is associated with many shortcomings. Firstly, the problem of scour is governed by a large number of non-dimensional parameters, whose effects are difficult to identify and isolate in experiments. Secondly, empirically-derived formulae lack of almost any physical basis and, as a consequence, their validity is often limited to the experimental data they have been developed from. Therefore, since most of the available data on local scour were obtained from laboratory experiments, it is likely that empirical formulae suffer from significant scale effects when applied to real engineering problems (Melville & Coleman, 2000; Ettema et al., 2011).

In order to overcome such difficulties, Manes & Brocchini (2015) recently proposed a different approach, which combines theoretical arguments with considerations taken from empirical evidence, to develop a better understanding of the physics of local scouring around structures. In particular, while an operational formula for local scour prediction was not proposed, Manes & Brocchini (2015) theoretically derived scaling relations between the normalized local scour depth at equilibrium and other non-dimensional parameters governing the problem. Such relations were then corroborated by experimental data taken from the literature. Since the proposed scaling relations were derived from physical arguments, these are, in principle, free

from scale issues. Hence, they represent an ideal basis to develop universal (i.e. scale-independent) formulae for local scour prediction.

The aim of the present Chapter is indeed to build upon the theoretical approach proposed by Manes & Brocchini (2015) in order to derive a predictive formula for local scour. Towards this end, the work by Manes & Brocchini (2015) requires to be significantly extended. In particular, Manes & Brocchini (2015) based their entire analysis on one key assumption, whereby momentum transport near the sediment-water interface was dominated by eddies belonging to the inertial range and scaling with the sediment diameter. In the present Chapter, the Manes & Brocchini (2015) approach will be extended to the case of momentum transport being dominated by near-wall eddies belonging to the dissipation and production ranges. This is relevant because sediment beds encountered in both field and laboratory are often composed of fine (e.g., sand) and very coarse (e.g., gravel, cobbles) sediment grains, where momentum transport may indeed be strongly driven by eddies pertaining to the aforementioned ranges of scales. With respect to Manes & Brocchini (2015), the present Chapter also provides a more in-depth theoretical analysis, which accounts for the effects of important scaling functions linking local to global variables, which were neglected in Manes & Brocchini (2015). Finally, the aforementioned theoretical insights allow for the development of a new formula for the prediction of local scour occurring around vertical cylinders in clear-water conditions and for uniform sediments.

The Chapter is organized as follows: § 2.2 provides the Manes & Brocchini (2015) theory revisited to account for dissipation- and production-range eddy effects; § 2.3 presents a general formula to predict the maximum scour depth at equilibrium in clear-water conditions; § 2.4 shows a practical appli-

cation of the presented formula; § 2.5 reports a summary of the main results and conclusions.

## 2.2 A revisited theory

As reported in the previous Chapter, when a turbulent open-channel flow impinges on a cylindrical isolated structure lying on an erodible bed, a complex flow field develops in the form of a downflow, a horseshoe vortex system, a wake vortex system and a surface roller (Melville & Coleman, 2000; Ettema et al., 2011; Dey, 2014) (Fig. 1(a)).

The downflow and the horseshoe vortex are the main responsible of local scour as they contribute to generate strong shear stresses at the junction between the structure and the sediment bed. In clear-water conditions (i.e., for  $0.5 < U/U_c < 1$  as reported by Breusers et al. (1977)) and for steady impinging flows, the high shear stresses generated by the horseshoe vortex contribute to erode the bed and to form a scour hole, which progressively deepens until an equilibrium condition is achieved. While there is no general consensus on the exact definition of equilibrium (see Manes & Brocchini (2015) for a review of this issue), it is fair to say that it is reached when the shear stress within the scour hole,  $\tau$ , approaches the critical shear stress,  $\tau_c$ , for the inception of sediment motion (Ettema et al., 2011).

In fact, as already hypothesized by Gioia & Bombardelli (2005), although Shields (1936) considered that the sediment motion is scattered, the experimental identification of the threshold for the inception of sediment motion can be defined for a single grain and, consequently, also in a limited bed surface, as in the case of a local scour hole.



Following Manes & Brocchini (2015), the analysis presented herein focuses on the deepest point of the scour hole, which is commonly observed right upstream to the pier (Raudkivi & Ettema, 1983), provided that the ratio between flow depth,  $h$ , and pier diameter is greater than 0.2, as it occurs in most relevant applications (Ettema et al., 2011). At this location and in equilibrium conditions, the local bed slope is known to be zero and therefore the critical shear stress,  $\tau_c$ , can be considered independent from slope effects (Unger & Hager, 2007; Kirkil et al., 2008).

The shear stress at the sediment-water interface,  $\tau$ , can be estimated as reported by Gioia et al. (2010) and, following Bonetti et al. (2017), in relation 1.12 the mean velocity gradient  $d\bar{u}/dz$  can be estimated as:

$$\frac{d\bar{u}}{dz} = \alpha_1 \frac{V}{l}. \quad (2.1)$$

The scaling function  $\alpha_1$ , that is once again an *ad hoc* scaling function to link local and global velocity gradients over the bed-normal direction, is unknown for the case of localized vortices scouring an erodible surface. However, some information can be borrowed from the recent work by Bonetti et al. (2017), who addressed the case of uniform and rough-bed open-channel flows. Bonetti et al. (2017) pointed out that  $\alpha_1$  scales as the square root of the friction factor, which, in the fully-rough regime, is a function only of the ratio between the characteristic length scale of large eddies,  $L$ , and the sediment diameter,  $d$ . In general, relaxing the assumption of the fully-rough regime, viscosity effects may be not negligible, and therefore  $\alpha_1$  may also depend on the Reynolds number or, equivalently, on the roughness Reynolds number, which expresses the ratio between the roughness diameter and the

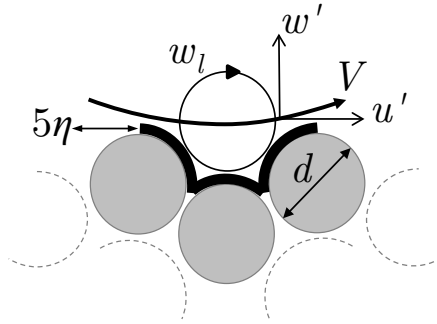


**Figure 2.1:** Simple illustration of the interplay between eddies of scale  $l = d + 5\eta$  and large-scale eddies.  $V$  is the characteristic velocity of large-scale eddies (i.e., eddies scaling with  $L$ ) and  $w_l$  is the characteristic velocity of eddies scaling with  $l$ ;  $5\eta$  is the thickness of the viscous sublayer (Gioia & Chakraborty, 2006).

viscous sub-layer thickness, here quantified as  $d/\eta$  (Fig. 2.1).

As clarified by Bonetti et al. (2017), the local mean dissipation rate,  $\epsilon$ , can be related to the bulk dissipation rate,  $\epsilon_b$ , via an *ad hoc* function,  $\alpha_2$ , as follows:

$$\epsilon = \alpha_2^3 \epsilon_b = \alpha_2^3 \frac{V^3}{L}. \quad (2.2)$$

Analogously to  $\alpha_1$ , even  $\alpha_2$  is an unknown scaling function. For the case of uniform open-channel flows, Bonetti et al. (2017) argued that  $\alpha_2$  depends on the relative roughness (here expressed as  $L/d$ ) and the friction factor, meaning that, as for  $\alpha_1$ , also  $\alpha_2$  may depend on  $L/d$  and  $d/\eta$ .

Following Manes & Brocchini (2015), the characteristic velocity of the horseshoe vortex,  $V$ , can be estimated from energetic considerations, which can be summarized as follows. The bulk dissipation rate can be interpreted

as the energy per unit time and unit mass (i.e., power,  $P$ , per unit mass,  $M$ ) of large-scale eddies, namely,  $\epsilon_b = P/M$ . Manes & Brocchini (2015) argued that  $M$  scales as  $M \sim \rho L^3$  and the power  $P$  can be expressed as the work per unit time of the drag force exerted by the flow on the portion of the structure exposed to scour. In turn, this can be quantified as the product between such drag force,  $F = 0.5\rho C_d a L U^2$ , and  $U$ , where  $C_d$  is the drag coefficient and  $aL$  the frontal area of the pier exposed to scour. Therefore, from Eq. 2.2:

$$\epsilon = \alpha_2^3 \frac{V^3}{L} = \frac{0.5\rho C_d a L U^3}{\rho L^3} \quad (2.3)$$

and, hence, the characteristic velocity,  $V$ , scales as:

$$V \sim U \left( \frac{C_d a}{L} \right)^{1/3}. \quad (2.4)$$

Coupling relations 1.12 and 2.4 and Eq. 2.1, the shear stress,  $\tau$ , can be estimated as:

$$\tau \sim \rho \alpha_1 U \left( \frac{C_d a}{L} \right)^{1/3} w_l. \quad (2.5)$$

In equilibrium conditions, the horseshoe vortex is commonly assumed to be fully-buried within the scour hole (Manes & Brocchini, 2015), therefore,  $L$  approaches the equilibrium scour depth,  $y_{se}$ . In addition, as the scour depth increases, the shear stresses acting on the scour hole surface decrease, until they reduce to the value of the critical shear stress for the inception of sediment motion,  $\tau_c = \theta(\rho_s - \rho)gd$ , where  $\rho_s$  is the sediment density,  $g$  the gravity acceleration and  $\theta$  the Shields mobility parameter (Baker, 1980;

Kothyari et al., 1992). Therefore:

$$\theta = \frac{\tau}{\tau_c} = \frac{\tau}{(\rho_s - \rho)gd} \sim \alpha_1 \frac{\rho}{\rho_s - \rho} \frac{U \left( \frac{C_{da}}{y_{se}} \right)^{1/3} w_l}{gd}. \quad (2.6)$$

Relation 2.6 can be used to predict the equilibrium scour depth,  $y_{se}$ . Towards this end, a key requirement is to know the Shields mobility parameter,  $\theta$ , and its dependence on the sediment and flow characteristics, which is now discussed to explain the rationale underpinning the next two sections of the present Chapter.

This approach is similar to the semi-analytical models of Baker (1980), Kothyari et al. (1992), Dey (1999) and Guo (2014), that link the maximum equilibrium scour depth with the shear stress acting below to the horseshoe vortex. In these models, it is considered that the shear stress or the eroded sediment discharge, determined with empirical formulae, decrease as the scour depth increases. With the PTT, this empiricism is overcome by a physically-based relation between  $y_{se}$  and  $\tau$ .

According to the sediment transport theory, when bed slope effects can be neglected, the Shields mobility parameter depends on the relative roughness and the roughness Reynolds number (Buffington & Montgomery, 1997). For the phenomenon of local scouring, these parameters can be defined as  $y_{se}/d$  and  $d/\eta$ , respectively, where the Kolmogorov length scale,  $\eta$ , can be estimated as:

$$\eta = \left( \frac{\nu^3}{\epsilon} \right)^{1/4} = \left( \frac{\nu^3 y_{se}}{\alpha_2^3 V^3} \right)^{1/4} \sim \left( \frac{\nu^3 y_{se}^2}{\alpha_2^3 U^3 C_{da}} \right)^{1/4}. \quad (2.7)$$

However, both the relative roughness  $y_{se}/d$  and the parameter  $d/\eta$  de-

pend on  $y_{se}$ . This makes it difficult to derive an explicit predictive equation for  $y_{se}$  and, most of all, to isolate and identify the effects of the two parameters on  $\theta$ . Hence, as suggested by Manes & Brocchini (2015), since the equilibrium scour depth is known to belong to the range from  $a$  to  $3a$ , it is convenient to replace  $y_{se}/d$  with  $a/d$ , so that it is possible to say that  $\eta$  (relation 2.8) scales as:

$$\eta \sim \left( \frac{\nu^3 a}{\alpha_2^3 C_d U^3} \right)^{1/4}. \quad (2.8)$$

According to the incipient motion theory (Buffington & Montgomery, 1997), when both  $d/\eta$  and  $a/d$  tend to infinity, self-similarity is reached and  $\theta$  tends to a constant value. This condition is consistent with the assumption that  $d$  falls in the inertial sub-range of length scales, as investigated by Manes & Brocchini (2015). When  $d/\eta$  or  $a/d$  attain smaller values, then near-bed momentum transport may begin to be influenced by either dissipation- or production-range eddies, respectively. This means that self-similarity is lost and there is need to find a functional relation between  $\theta$ ,  $d/\eta$  and  $a/d$ . As outlined by Manes & Brocchini (2015), the effects of  $a/d$  on  $\theta$  are significant only when  $a/d < 20$ . On the contrary, viscosity effects may be not negligible over a wide range of  $d/\eta$  values (this is also observed in open-channel flows over flat beds for  $1 < d/\eta < 1000$ ; see Buffington & Montgomery (1997); Shields (1936)).

In order to identify and isolate the effects of  $d/\eta$  and  $a/d$  on  $\theta$ , the next two sections are organized as follows: § 2.2.1 addresses the functional dependence of  $\theta$  and  $\tau$  on  $d/\eta$  when  $a/d > 20$ , hypothesizing that the  $d/\eta$  effects can be reasonably isolated; § 2.2.2 presents the functional dependence

of  $\theta$  and  $\tau$  on  $a/d$  for  $a/d < 20$ , where the  $d/\eta$  effects may still be not negligible, but can be taken into account by exploiting the outcomes of § 2.2.1.

### 2.2.1 $d/\eta$ effects

For small values of  $d/\eta$ , the shear stress,  $\tau$ , and its dimensionless form,  $\theta$ , are influenced by viscosity and momentum transport is dominated by eddies of scale  $l$  belonging to the dissipation range. Following the seminal work by Gioia and co-workers (Bombardelli & Gioia, 2006; Gioia & Chakraborty, 2006), the characteristic velocity of these eddies can be found from the integration of a turbulence-spectrum model within the dissipation range. However, this approach is not straightforward, because integration needs to be performed numerically. Furthermore, currently-available spectral models (e.g., the Pao spectrum, see Pope (2001)) fail to reproduce important features occurring at the crossover between inertial and dissipation scales, such as the so-called bottleneck effect (Katul et al., 2015). Therefore, in this Chapter  $w_l$  is obtained from a structure-function model, namely the Batchelor structure function, which overcomes the aforementioned limitations (Lohse & Müller-Groeling, 1995).

The second order Batchelor structure function, which describes turbulence properties within the inertial and the dissipation ranges, reads as:

$$\frac{D(l)}{v_\eta^2} = \frac{l^2/3\eta^2}{[1 + (1/3b)^{3/2}(l/\eta)^2]^{1-\xi/2}}, \quad (2.9)$$

where  $\xi = 2/3$  and  $b \approx 5$ . The second order velocity structure function in Eq. 2.9 will be used to compute the characteristic velocity fluctuation of

eddies of size  $l$ . In fact, within a phenomenological context, the velocity scale  $w_l$  could or should be interpreted as the velocity difference along a distance equal to  $2l$ , which can be predicted from the second-order velocity structure function computed at a distance  $2l$  (Katul & Manes, 2014), i.e.:

$$w_l = \sqrt{D(l)}. \quad (2.10)$$

Coupling Eq. 2.10 and relation 2.6, the shear stress can be estimated as:

$$\tau \sim \rho \alpha_1 U \left( \frac{C_d a}{L} \right)^{1/3} \sqrt{D(l)}. \quad (2.11)$$

It is now interesting to make some observations on the effects of viscosity on the shear stress,  $\tau$ . Such effects can be considered through the ratio between the shear stress generated by near-wall eddies pertaining to the dissipation range (i.e., computed from relation 2.11) and the shear stress that would be generated assuming that  $d$  belongs to the inertial range and the flow is in the fully-rough regime (i.e.,  $l \approx d$  and  $w_l \approx w_d$ , as in Manes & Brocchini (2015)). Relation 2.5 indicates that this ratio scales as  $w_l/w_d$ , where  $w_d$  can be easily estimated from the Kolmogorov second-order structure function,  $D_{Kol}$ , as  $w_d = \sqrt{D_{Kol}(d)}$ , where  $D_{Kol}(d)$  in dimensionless form reads as:

$$\frac{D_{Kol}(d)}{v_\eta^2} = C_0 \left( \frac{d}{\eta} \right)^{2/3}, \quad (2.12)$$

and  $C_0$  is a universal constant approximately equal to 2 (Saddoughi & Veeravalli, 1994; Frisch, 1995).

Fig. 2.2 reports the ratio  $w_l/w_d = \sqrt{D(l)}/\sqrt{D_{Kol}(d)}$  as estimated using Eqs. 2.9 and 2.12 as a function of different  $d/\eta$ . When  $d/\eta$  is very large, the

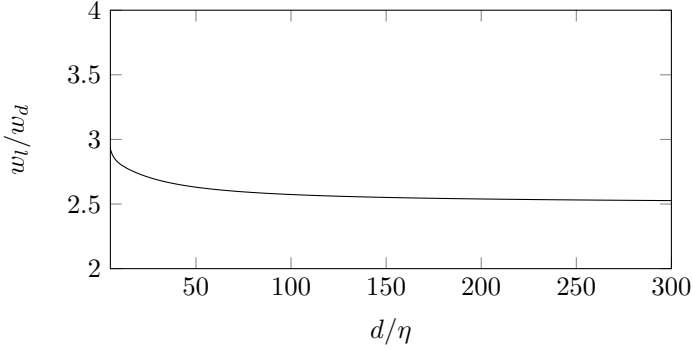


**Figure 2.2:** Ratio  $w_l/w_d$  as a function of  $d/\eta$ .

ratio  $w_l/w_d$  tends asymptotically to a constant, which makes sense because viscous effects must become negligible for large values of  $d/\eta$ . More interestingly, within the range  $5 < d/\eta < 300$  (which covers conditions consistent with experimental data),  $w_l/w_d$  varies of about 13%. It should be noted that, even in perfectly-controlled conditions of uniform turbulent flows over flat beds, errors of 13% are well within the experimental uncertainty associated with the identification of incipient motion conditions or, in other words, in quantifying the critical shear stress. This means that replacing  $w_l$  with  $w_d$  is an acceptable simplification and hence:

$$w_l \approx w_d = \sqrt{D_{Kol}(d)} \sim (\epsilon d)^{1/3}. \quad (2.13)$$

Combining Eq. 2.2 and relation 2.4 and imposing equilibrium conditions (i.e.,  $L = y_{se}$ ) leads to:

$$w_d \sim \alpha_2 U \left( \frac{C_d a}{y_{se}} \right)^{1/3} \left( \frac{d}{y_{se}} \right)^{1/3}. \quad (2.14)$$

Finally, an expression of  $\theta$  can be obtained by combining relations 2.14



and 2.11:

$$\theta \sim \alpha_1 \alpha_2 \frac{\rho}{\rho_s - \rho} \frac{U^2}{gy_{se}} \left( \frac{C_d a}{d} \right)^{2/3}. \quad (2.15)$$

According to Manes & Brocchini (2015), when  $a/d > 20$ ,  $\theta$  should be a function of  $d/\eta$  only. However, as already discussed, the product  $\alpha_1 \alpha_2$ , whose scaling is unknown, may retain dependence on  $a/d$ . Whether this is the case or not can be explored only from experimental data. Towards this end, the aforementioned simplification (i.e.,  $w_l \approx w_d$ ) allows merging  $\alpha_1, \alpha_2, \theta$  and the scaling constant in relation 2.15 in a new Shields mobility function,  $f_1$ :

$$f_1 = \frac{\rho}{\rho_s - \rho} \frac{U^2}{gy_{se}} \left( \frac{C_d a}{d} \right)^{2/3}, \quad (2.16)$$

whose dependence on  $d/\eta$  and  $a/d$  can be investigated quite easily from experimental data. Without such simplification,  $\theta$  would retain an implicit dependence on  $\alpha_2$  through  $w_l$  and  $\eta$  (see relations 2.8 and 2.11 and Eqs. 2.9 and 2.10), which would be very difficult to investigate and would add a greater level of uncertainty to the whole analysis.

The experimental data provided by Ettema (1980), Ettema et al. (2006), Mignosa (1980), Yanmaz & Altinbilek (1991), Dey et al. (1995) and Shepard et al. (2004) (consisting of 169 tests in total) are now used to derive  $f_1$  via Eq. 2.16. These experimental data-sets refer to circular piers and uniform sediments in clear-water condition and were chosen as they cover a wide range of roughness Reynolds numbers (i.e.,  $d/\eta$ ), which is quite rare in the literature. Table 2.1 summarises the most important laboratory conditions related to the aforementioned studies.

**Table 2.1:** Experimental range of used data-sets:  $h$  is the flow depth,  $B$  the channel breadth,  $Fr = U/\sqrt{gh}$  the flow Froude number,  $Re_a = Ua/\nu$  the pier Reynolds number. All the experiments were carried out using uniform sand of density  $\rho_s = 2650 \text{ kg/m}^3$ , except Mignosa (1980) experiments that were carried out using uniform synthetic sediment of density  $\rho_s = 1180 \text{ kg/m}^3$ .

Data-set	$U$ (m/s)	$a$ (m)	$d$ (mm)	$h$ (m)	$a/B$
Ettrema (1980)	0.18÷1.34	0.02÷0.40	0.24÷7.80	0.02÷1.00	0.02÷0.15
Ettrema et al. (2006)					
Mignosa (1980)	0.13÷0.18	0.02÷0.05	2.6	0.12÷0.13	0.05÷0.10
Yamamaz & Altinbilek (1991)	0.15÷0.36	0.47÷0.67	0.84÷1.07	0.08÷0.17	0.07÷0.10
Dey et al. (1995)	0.17÷0.26	0.57÷0.76	0.56÷0.58	0.35÷0.50	0.07÷0.10
Sheppard et al. (2004)	0.29÷0.70	0.11÷0.91	0.22÷2.90	0.17÷1.90	0.01÷0.15
	$h/a$	$a/d$ (m)	$Fr_a$ (m)	$Fr$ (m)	$Re_a$
Ettrema (1980)	0.20÷21.00	4÷1000	0.17÷2.53	0.07÷1.00	10000÷260000
Ettrema et al. (2006)					
Mignosa (1980)	2.60÷4.70	20÷22	0.19÷0.28	0.12÷0.17	3000÷9000
Yamamaz & Altinbilek (1991)	1.80÷3.5	43÷80	0.20÷0.55	0.13÷0.29	7000÷24000
Dey et al. (1995)	0.46÷0.88	98÷292	0.20÷0.35	0.29÷0.37	9000÷20000
Sheppard et al. (2004)	0.19÷11.50	136÷414	0.10÷0.39	0.07÷0.38	32000÷690000

In order to explore the dependence of  $f_1$  on  $d/\eta$  it is necessary to compute  $\eta$  from experimental data. Relation 2.8 indicates that this is possible only if the scaling function  $\alpha_2$  is known, and this is not the case. We are therefore forced to adopt the same approach as Manes & Brocchini (2015), where  $\alpha_2$  was considered as a constant, so that a surrogate of the Kolmogorov length scale,  $\eta_1$  (which approximates  $\eta$ ), can be computed as follows:

$$\eta_1 = \alpha_2^{3/4} \eta = \left( \frac{\nu^3 a}{C_d U^3} \right)^{1/4}. \quad (2.17)$$

Fig. 2.3 shows that, with the exception of very few points, experimental data nicely collapse on curves, which, after a careful analysis, were observed to show no obvious dependence on  $a/d$ , meaning that  $f_1$  is a function of  $d/\eta_1$  only. More interestingly, such curves resemble the classical Shields diagram (especially the data gathered by Ettema and co-workers, which cover the widest range of  $d/\eta_1$ ), displaying a minimum that separates a decreasing side from an increasing one that, in turn, mirror the transitionally-smooth and transitionally-rough regimes, respectively. This result is encouraging, as it is consistent with paradigms of sediment incipient motion theory. In fact, in local scour studies, the equilibrium scour depth is actually found when sediment-incipient-motion conditions occur within the scour hole. Since the analysis presented herein applies to sediment grains located at the bottom of the scour hole, where local slope effects are negligible, and as reported above, there is no reason why incipient motion conditions should not follow, at least qualitatively, the classical behaviour observed by Shields and subsequent works in uniform open channel flows (see, e.g., Buffington & Montgomery (1997)).

The curves shown in Fig. 2.3 are well described by the following equation,

$$f_1 = F_1 \left\{ 0.22 \left( \frac{d}{\eta_1} \right)^{-0.6} + 0.06 e^{\left[ -17.77 \left( \frac{d}{\eta_1} \right)^{-0.6} \right]} \right\}, \quad (2.18)$$

where  $F_1 = 56$  in Fig. 2.3(a),  $F_1 = 34$  in Fig. 2.3(b).

Eq. 2.18 retains the same mathematical expression as the well-known Brownlie equation (Brownlie, 1981) (originally derived to fit the Shields data), except for some free parameters that were tuned to obtain an *ad hoc* fit of the experimental data. Furthermore, it was necessary to introduce a parameter  $F_1$  to compensate for the different definitions of equilibrium scour depths used by the authors of the references where the experimental data-sets were taken from. In fact, in the experiments by Ettema (1980) and Ettema et al. (2006) equilibrium conditions were considered to be reached when no significant change of the scour depth was observed over a fixed period of four hours, whereas Mignosa (1980), Yanmaz & Altinbilek (1991), Dey et al. (1995) and Sheppard et al. (2004) considered the concept of equilibrium as an asymptotic condition. As also pointed out by Manes & Brocchini (2015), these two different definitions account for discrepancies in the estimation of the equilibrium scour depth exceeding 30%. This justifies why the two data-sets reported in Fig. 2.3 were not merged to derive a universal fitting function, as discrepancies associated with different definitions of equilibrium scour depth can add fictitious scatter that, in turn, may hide important trends.

It should be noted that the scatter in Fig. 2.3 is anyway not negligible and the choice of using a fitting curve with a shape resembling the Shields curve was made somewhat on purpose to retain consistency with incipient

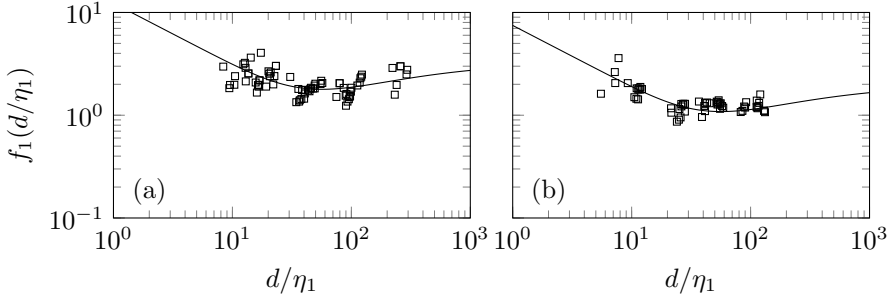


**Figure 2.3:** Dependence of  $f_1$  on  $d/\eta_1$ . Data by (a) Ettema (1980) and Ettema et al. (2006) and (b) Mignosa (1980), Yanmaz & Altinbilek (1991), Dey et al. (1995) and Sheppard et al. (2004).

motion theory. In fact there is no real statistical evidence for Eq. 2.18 to be the best fitting curve. For example, the ratios between the sum of least square residuals associated with Eq. 2.18 and a line of constant  $f_1$  are 0.83 and 0.45 for Fig. 2.3(a) and (b), respectively. This is encouraging, as it means that Eq. 2.18 performs better than the line of constant  $f_1$ , but differences are small and more data points are needed to carry out a robust statistical analysis. This is particularly true for the data-set by Ettema and co-workers reported in Fig. 2.3(a).

Another interesting point of discussion arises from the comparison between Figs. 2.3 and 2.2, which may suggest for an apparent contradiction. In Fig. 2.2 we argued that viscous effects (i.e., dependence on  $d/\eta$ ) are negligible on dictating the shear stress at the sediment-water interface, yet, viscous effects (i.e., dependence on  $d/\eta_1$ ) are significant for  $f_1$  (i.e., where  $f_1$  can be interpreted as a Shields mobility parameter or, equivalently, a non-dimensional critical shear stress) over the entire range of  $d/\eta_1$  reported in Fig. 2.3. One may argue that if viscosity effects are negligible for the

shear stress so should be for  $f_1$  as the two quantities are closely linked. This apparent contradiction is actually perfectly in line with classical paradigms of turbulent flow resistance and incipient motion theory. In fact, in turbulent flows over granular surfaces, viscous forces affect flow resistance until the roughness Reynolds number  $Re_*$  reaches the value of 70, beyond which the flow is in the fully-rough regime. On the contrary, a vast number of incipient motion studies in turbulent open channel flows indicates that the critical shear stress retains  $Re_*$  dependence up to  $Re_* = 400$ , i.e., an order of magnitude more (Buffington & Montgomery, 1997). This means that the occurrence of the fully-rough regime (i.e., negligible viscous effects on flow resistance) does not necessarily imply that incipient-motion conditions are free from  $Re_*$  effects, which is precisely what is argued (and observed) in the present Chapter.

### 2.2.2 $a/d$ effects

Manes & Brocchini (2015) demonstrated that the theoretical framework must be modified for  $a/d < 20$  to include the effects of large-scale eddies, namely eddies that belong to the production range of the turbulence spectrum. In these conditions,  $d/\eta$ , owing to the fact that  $\eta$  increases when  $a$  increases (see e.g., Eq. 2.8), is usually very large, meaning that near-bed momentum transport is dominated by eddies scaling with  $d$  (i.e., viscous effects on  $\tau$  are small), which however is large enough to be comparable with  $a$ . We define the characteristic velocity of such eddies as  $w_d^P$ , where the superscript  $P$  indicates that  $d$  belongs to the production range of scales. Hence, relation 2.6 can be rewritten as:

$$\theta \sim \alpha_1 \frac{\rho}{\rho_s - \rho} \frac{U \left( \frac{C_d a}{y_{se}} \right)^{1/3} w_d^P}{gd}. \quad (2.19)$$

In order to estimate the appropriate velocity scale  $w_d^P$ , it is necessary to employ a model as done for  $w_l$  in the previous section. However, contrary to small-scale turbulence, large-scale eddies are strongly flow-dependent and no universal spectral or structure function formulation exists, that describes how energy is distributed among scales within the production range. Anyway, it is possible to demonstrate that the difference between  $w_d^P$  and  $w_d$ , i.e., a velocity scale that assumes  $d$  belonging to the inertial range, is not significant in scouring flows or, alternatively, that a model for the precise distribution of energy among scales in the production range is not required for the estimation of the shear stress  $\tau$  acting within a scour hole.

Towards this end, let us start defining the velocity scale  $w_d^P$  in terms of the energy spectrum function  $E(k)$ :

$$w_d^{P2} = \int_{k_d}^{\infty} E(k) dk, \quad (2.20)$$

where  $k = 2\pi/l$  is the wavenumber,  $l$  is the length scale of the mode (i.e., of a turbulent scale of motion) and  $k_d = 2\pi/d$  is the wavenumber corresponding to a turbulent length scale  $d$ . We make use of the von Kármán spectrum (Pope, 2001) as a mathematical basis to derive a spectral shape that is appropriate for turbulent flows within scour holes. Therefore,  $E(k)$  can be taken as follows:

$$E(k) = C\epsilon^{2/3} k^{-5/3} \exp(-\beta\eta k) \left[ 1 + \frac{\gamma}{(ky_{se})^2} \right]^\delta, \quad (2.21)$$

where  $C\epsilon^{2/3}k^{-5/3}$  is the Kolmogorov spectrum and  $C = 1.5$  is considered as a universal constant (see Pope (2001));  $\exp(-\beta\eta k)$  and  $[1 + \gamma/(ky_{se})^2]^\delta$  are dimensionless correction functions that describe the dissipation and the production range, respectively;  $\beta$ ,  $\gamma$  and  $\delta$  are dimensionless constants. The function  $\exp(-\beta\eta k)$  determines the shape of the dissipation range of the spectrum. Similarly,  $[1 + \gamma/(ky_{se})^2]^\delta$  controls the shape of the production range. Since  $d$  belongs to the production range, it seems reasonable to neglect viscous effects, so that Eq. 2.20 becomes:

$$w_d^{P2} \approx \int_{k_d}^{\infty} \epsilon^{2/3} k^{-5/3} \left[ 1 + \frac{\gamma}{(ky_{se})^2} \right]^\delta dk, \quad (2.22)$$

The velocity scale  $w_d$  can be computed by simply assuming  $[1 + \gamma/(ky_{se})^2]^\delta = 1$ , as follows:

$$w_d^2 = \int_{k_d}^{\infty} \epsilon^{2/3} k^{-5/3} dk. \quad (2.23)$$

The ratio  $w_d^P/w_d$  can be therefore computed as:

$$\frac{w_d^P}{w_d} = \left\{ \frac{\int_{k_d}^{\infty} \epsilon^{2/3} k^{-5/3} \left[ 1 + \frac{\gamma}{(ky_{se})^2} \right]^\delta dk}{\int_{k_d}^{\infty} \epsilon^{2/3} k^{-5/3} dk} \right\}^{1/2}, \quad (2.24)$$

which, after changing the integration variable,  $x = ky_{se}$ , becomes:

$$\frac{w_d^P}{w_d} = \left[ \frac{\int_{y_{se}k_d}^{\infty} x^{-5/3} \left( 1 + \frac{\gamma}{x^2} \right)^\delta dx}{\int_{y_{se}k_d}^{\infty} x^{-5/3} dx} \right]^{1/2}. \quad (2.25)$$

Pope (2001) reports that, for  $\gamma = 6.783$  and  $\delta = -17/6$ , the model spectrum nicely fits grid-turbulence data and respects the constraint  $TKE =$



$\int_0^\infty E(k) dk$ , where  $TKE$  is the turbulent kinetic energy. For turbulent flows within scour holes, the exact shape of the model spectrum is unknown. However, it can be speculated that an appropriate candidate should retain at least one key characteristic, namely it should peak at scales commensurate to  $y_{se}$  or, equivalently, at  $ky_{se} \approx 2\pi \approx 6.3$  (Chang et al., 2013). Fig. 2.4(a) shows that the von Kármán spectrum (plotted in pre-multiplied form to better identify the peak) computed with  $\gamma = 6.783$  and  $\delta = -17/6$  retains this property and, therefore, represents a reasonable model to estimate  $w_d^P$  in Eq. 2.25.

Since the equilibrium scour depth is always greater than at least one sediment diameter (i.e.,  $y_{se}/d > 1$ ), the lower limit of the integrals in Eq. 2.25 cannot be smaller than  $y_{se}k_d = 2\pi$ . Therefore, the portion of the model spectrum that is of interest for scour flows lies in the range  $y_{se}k_d > 2\pi$ , i.e., at non-dimensional wavenumbers greater than the one associated with the spectrum peak. Since such a peak is very close to the beginning of the inertial range, it is reasonable to expect that the ratio  $w_d^P/w_d$  must be very close to one for any value of  $y_{se}k_d > 2\pi$ . This is confirmed by Fig. 2.4(b), where  $w_d^P/w_d$  was obtained by solving numerically the integrals in Eq. 2.25. Overall, it is possible to conclude that, as far as the shear stress  $\tau$  is concerned, the exact shape of the energy spectrum in the production range is totally irrelevant in scouring flows or, equivalently, that the production-range correction to the energy spectrum function can be neglected for the computation of  $w_d^P$ , which can be therefore calculated as:

$$w_d^P \approx w_d = \left( \int_{y_{se}k_d}^{\infty} \epsilon^{2/3} k^{-5/3} dk \right)^{1/2}. \quad (2.26)$$

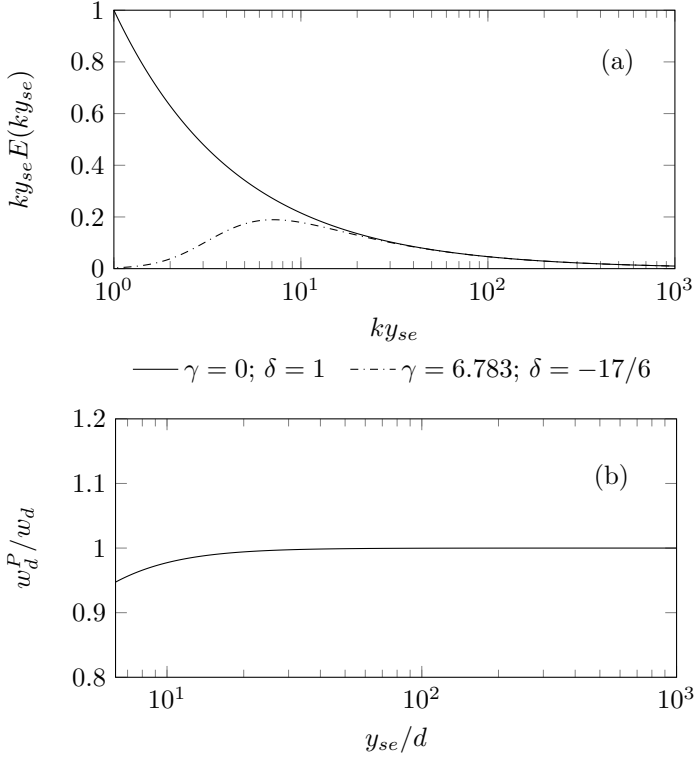


**Figure 2.4:** (a) The von Kármán spectrum (dash-dotted line) and the Kolmogorov spectrum (solid line) in premultiplied form; (b)  $w_d^P/w_d$  as a function of  $y_{se}/d$ .

Using Eq. 2.2 and after some algebra:

$$w_d^P \sim \alpha_2 V \left( \frac{d}{y_{se}} \right)^{1/3} \sim \alpha_2 U \left( \frac{C_{da}}{y_{se}} \right)^{1/3} \left( \frac{d}{y_{se}} \right)^{1/3}. \quad (2.27)$$

Therefore, after combining relations 2.27 and 2.19 the following relation for  $\theta$  is obtained:

$$\theta \sim \alpha_1 \alpha_2 \frac{\rho}{\rho_s - \rho} \frac{U^2}{gy_{se}} \left( \frac{C_{da}}{d} \right)^{2/3}. \quad (2.28)$$

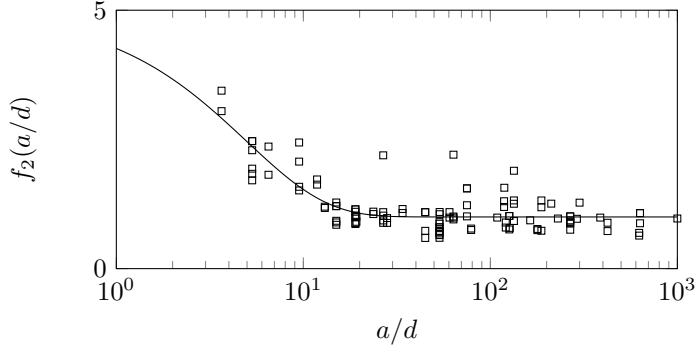


**Figure 2.5:** Function  $f_2$ ; data by Ettema (1980) and Ettema et al. (2006).

In order to isolate and identify the effects of  $a/d$ , the Shields mobility parameter,  $\theta$ , in relation 2.28 is divided by  $f_1$ , as per Eq. 2.18. Merging  $\theta$ ,  $\alpha_1, \alpha_2$  and the scaling constant in relation 2.28 in a function  $f_2$  leads to:

$$f_2\left(\frac{a}{d}\right) = \frac{\frac{\rho}{\rho_s - \rho} \frac{U^2}{g y_{se}} \left(\frac{C_d a}{d}\right)^{2/3}}{f_1\left(\frac{d}{\eta}\right)}. \quad (2.29)$$

The experimental data by Ettema (1980) and Ettema et al. (2006), which do have  $a/d \leq 20$ , are now used to derive the function  $f_2(a/d)$  via Eq. 2.29 (Fig. 2.5). The solid line represents an *ad hoc* fit of the empirical points and corresponds to the following equation:

$$f_2 = 1 + 6e^{-\frac{1}{5} \frac{a}{d}}. \quad (2.30)$$

Fig. 2.5 shows that  $f_2$  (which can be also interpreted as a sort of Shields' mobility parameter) decreases with increasing  $a/d$  until  $a/d > 20$ , where it reaches a plateau. This is in accord with the Melville equation for  $y_{se}$  (Ettema et al., 2011) and implies that lower values of relative roughness are associated

with higher values of critical shear stress, which is also observed in canonical experiments of incipient motion in turbulent and uniform open-channel flows (Mueller et al., 2005; Buffington & Montgomery, 1997). However, as a note of caution, it should be also noted that when  $d$  becomes comparable to the size of the pier diameter,  $a$ , the scour hole is usually rather small (Ettema, 1980) so much so that the horseshoe vortex may be not fully-buried in the scour hole, which is an important hypothesis of the whole theoretical framework presented herein. Therefore, the decreasing trends of  $f_2$  vs  $a/d$  observed in Fig. 2.5 may be a lumped effect of different causes.

### 2.3 A predictive formula for the clear-water maximum local scour depth at a vertical cylinder

A final formula for clear-water local scour is now presented for the computation of  $y_{se}$  and its performance is tested against predictions made with the original Manes & Brocchini (2015) approach. Merging Eqs. 2.16 and 2.29 leads to:

$$\frac{\rho}{\rho_s - \rho} \frac{U^2}{gy_{se}} \left( \frac{C_d a}{d} \right)^{2/3} = f \left( \frac{d}{\eta_1}, \frac{a}{d} \right), \quad (2.31)$$

where, recalling Eqs. 2.18 and 2.30, and hypothesizing that  $f(d/\eta_1, a/d)$  is equal to the product between  $f_1(d/\eta_1)$  and  $f_2(a/d)$ :

$$f \left( \frac{d}{\eta_1}, \frac{a}{d} \right) = F_1 \left\{ 0.22 \left( \frac{d}{\eta_1} \right)^{-0.6} + 0.06 e^{\left[ -17.77 \left( \frac{d}{\eta_1} \right)^{-0.6} \right]} \right\} \left( 1 + 6 e^{-\frac{1}{5} \frac{a}{d}} \right). \quad (2.32)$$

Clearly, Eq. 2.32 can be used as a predictive formula for  $y_{se}$  as:

$$y_{se} = \frac{\frac{\rho}{\rho_s - \rho} \frac{U^2}{g} \left( \frac{C_{da}}{d} \right)^{2/3}}{f \left( \frac{d}{\eta_1}, \frac{a}{d} \right)}, \quad (2.33)$$

where, for consistency with  $f_2$ , which was derived entirely from the data-set of Ettema and co-workers,  $F_1$  should be taken as  $F_1 = 49$ .

In order to show the improvements of the present approach with respect to the original Manes & Brocchini (2015), Figs. 2.6(a-b) present a comparison between the measured  $y_{se_m}$  and computed  $y_{se_c}$  equilibrium scour depths, using either the original or the revisited Manes & Brocchini (2015) approach. Fig. 2.6 shows recognizably that the new approach allows for a much better interpretation of the data-sets, which collapse on the perfect agreement line with a coefficient of determination  $R^2 = 0.94$ , which is greater than that obtained by applying the original Manes & Brocchini (2015) theory ( $R^2 = 0.84$ ).

Furthermore, panels (c) and (d) of Fig. 2.6 show the correlation between the measured maximum scour depth at equilibrium and the computed maximum scour depth at equilibrium using the leading methods for scour depth prediction contained in the recent report by Ettema et al. (2011). In particular, panel (c) reports the scour depth estimations,  $y_{se_c}$ , computed using the Richardson and Davis method (E. V. Richardson et al., 1993) ( $R^2 = 0.85$ ), whereas panel (d) reports  $y_{se_m}$  computed using the Sheppard and Melville method (Melville (1997) and Sheppard & Miller Jr (2006)) ( $R^2 = 0.95$ ). Figure 2.6 clearly shows that the proposed new formula, when tested against experimental data, leads to scatter levels that are comparable to that obtained using the empirical formula of Sheppard and Melville method and

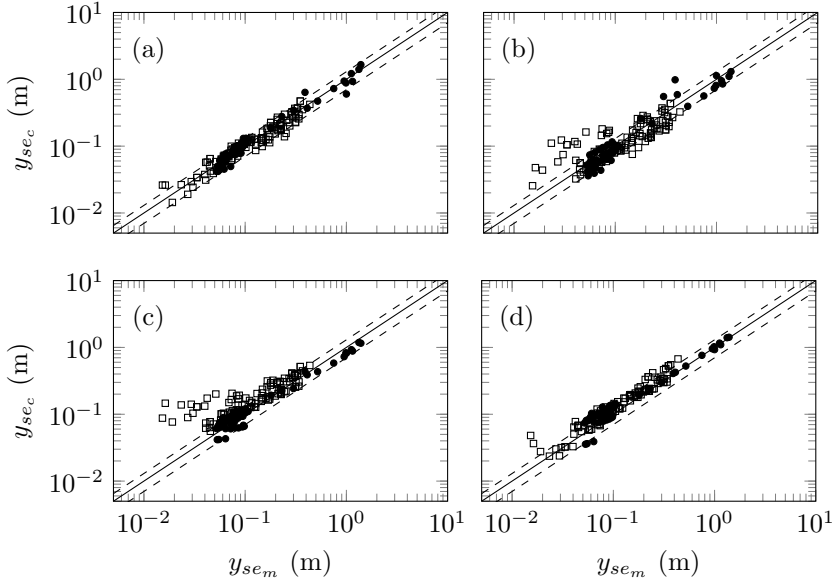


**Figure 2.6:** Computed ( $y_{sec}$ ) vs measured ( $y_{sem}$ ) scour depths at equilibrium; (a)  $y_{sec}$  from the revisited Manes & Brocchini (2015) theory; (b)  $y_{sec}$  from the original Manes & Brocchini (2015) formulation; (c)  $y_{sec}$  from the Richardson and Davis method (E. V. Richardson et al., 1993); (d)  $y_{sec}$  from the Sheppard and Melville method (Melville (1997) and Sheppard & Miller Jr (2006)); data is taken from Ettema (1980), Ettema et al. (2006) (black squares) and Mignosa (1980), Yanmaz & Altinbilek (1991), Dey et al. (1995) and Sheppard et al. (2004) (full black circles). The solid lines represent the perfect agreement between measured and computed values, whereas the dashed lines represent the associated  $\pm 30\%$  error bounds.

even lower to that of Richardson and Davis method.

As a final comment, it is worth pointing out that Eq. 2.33 predicts finite scour depths regardless of the magnitude of the impinging velocity  $U$ . This goes against experimental evidence, which shows that local scour occurs only if  $0.5 < U/U_c < 1$ . This condition (which essentially requires that local

scour will actually occur) represents therefore an important pre-requisite for the applicability of Eq. 2.33 for local scour prediction.

## 2.4 Example of application

An example of application is presented. A stream flowing in a channel with rectangular cross-section has the following characteristics:

- design discharge:  $Q = 1000 \text{ m}^3/\text{s}$ ;
- channel slope:  $S_0 = 0.007$ ;
- channel width:  $B = 125 \text{ m}$ ;
- sediment characteristic diameters:  $d_{50} = 40 \text{ mm}$ ;  $d_{90} = 130 \text{ mm}$ ;
- density of the sediment:  $\rho_s = 2650 \text{ Kg/m}^3$ ;
- pier diameter:  $a = 4 \text{ m}$ .

*Calculation:*

- Manning roughness coefficient:  $n = 0.0122d_{90}^{1/6} \text{ s/m}^{1/3}$ ;
- water depth:  $Q = \frac{1}{n}Bh \left( \frac{Bh}{B+2h} \right)^{2/3} S_0^{1/2} \Rightarrow h = 1.805 \text{ m}$ ;
- hydraulic radius:  $R = \frac{Bh}{B+2h} = 1.754 \text{ m}$ ;
- cross-sectional average velocity  $U = \frac{Q}{Bh} = 4.432 \text{ m/s}$ ;
- shear velocity:  $u_*\sqrt{gRS_0} = 0.347 \text{ m/s}$ ;
- shear Reynolds number  $Re_* = \frac{du_*}{\nu} = 1279$ ;

- $\frac{d}{\eta_1} = Re_*^{3/4} = 214$ ;
- scour depth (Eq. 2.33)  $y_{se} = 9.87$  m.

## 2.5 Conclusions

The aim of the present Chapter was to recast the Manes & Brocchini (2015) approach within a more rigorous and general theoretical framework and to derive a formula that, with respect to the original Manes & Brocchini (2015) formulation, can predict effectively the equilibrium scour depth for vertical cylinders under clear-water steady flows.

The main results of the proposed analysis can be summarized as follows:

i) regardless of whether near-bed eddies pertain to the dissipation or production range, the shear stress acting within the scour hole can be estimated fairly well by means of the original formulation proposed by Manes & Brocchini (2015) (provided that the scaling functions  $\alpha_1$  and  $\alpha_2$  are also taken into account), whereby near-bed eddies scale with the sediment diameter and belong to the inertial range;

ii) contrary to the shear stress, equilibrium conditions are strongly affected by the nature and scale of near-bed eddies. In particular, viscosity effects, which contribute to identify the characteristic length,  $l$ , and velocity scale,  $w_l$ , of such eddies (see Eq. 2.9), are significant for a wide range of  $d/\eta_1$ . Such effects are taken into account through function  $f_1$  (Eq. 2.18);

iii) when near-bed eddies pertain to the production range (i.e., for  $a/d < 20$ ), the equilibrium conditions strongly depend on the relative roughness  $a/d$ , as described by function  $f_2$  (Eq. 2.30);

iv) interestingly, the effects of viscosity and relative roughness on dic-



tating incipient motion conditions in local scour holes mirror those observed for flat sediment beds underlying uniform and turbulent open-channel flows (i.e., in canonical incipient motion studies);

v) when functions  $f_1$  and  $f_2$  are combined in Eq. 2.32, the agreement between measured and computed equilibrium scour depths is better than that in Manes & Brocchini (2015) and comparable with (and in some instances better than) that of existing empirical formulae.

With respect to point v), it should be pointed out that the proposed formula cannot be considered as “operational”, as its applicability is still limited to cylindrical piers, clear-water and uniform-sediment conditions and is therefore incomplete. Moreover, this Chapter, despite mentioning the issue of the link between laboratory data and field data cannot deal with it completely owing to lack of field data on local scour. In fact, the formulae for the equilibrium scour depth assessment overestimate  $y_{se}$  and this could be due to scale effects (Ettema et al., 2011). However, it represents an important first step towards the development of a physically-based and hence universal (i.e., free from scale issues as reported by Gioia & Bombardelli (2005) and Manes & Brocchini (2015)) formula for local scour prediction.



## Chapter 3

# Local scour around bridge abutments and the phenomenology of turbulence

### 3.1 Introduction

Analogously to the pier case, when an open-channel flow impinges on a bridge abutment a three-dimensional vortex system forms and triggers an erosion phenomenon in the vicinity of the sediment bed (Fig 1(b)). As reported in the previous Chapter, recently Manes & Brocchini (2015) derived a new scaling law for the maximum local scour depth at equilibrium around cylindrical structures, such as bridge piers, surrounded by turbulent open-channel flows overlying erodible beds. This approach, that is scale-independent and clarifies the contribution of the dimensionless groups to scouring, can be now extended to the case of abutments, in which the scour-

ing mechanism could be different. In fact, as reported by Melville (1997), the scour depth at an abutment is acknowledged to be less than that at a pier with the same width, owing to the channel wall retardation effects on the flow. Furthermore, various classical studies by Melville & Raudkivi (1977), Kwan (1988) and Melville & Raudkivi (1996) confirmed the similarity of the flow field within the scour hole at piers and abutments with the same transversal length extends into the channel only for a short distance, with respect to the flow depth. In fact, the vortex system generating the maximum scour depth along the centreline at the upstream face of a pier produces a scour depth reasonably uniform and similar to that at piers along the upstream face of short abutments (Melville, 1997). For long abutments, Kwan (1984) identified two flow regions: 1) a principal spiral flow, near the channel centreline, that is the main and unique responsible of the scouring process; 2) a secondary counter-rotating flow, formed at the junction between the bridge abutment and the channel bank. This quiescent fluid zone can be considered to demarcate the surface of an “effective” abutment, because the fluid within this area does not affect the scour process. Owing to this premise, new developments for the abutments case have to be done, because the scaling law cannot be directly obtained; and the Manes & Brocchini (2015) theory needs some adjustments to be applied. For this reason, a revisited theory for scouring at bridge abutments has to be elaborated, in order to discuss the geometric properties of the scour hole, and subsequently validate on the basis of experimental data. The theory will be presented in §3.2, whereas §3.3 provides the details of an original experimental campaign carried out to validate the theoretical hypotheses. Finally, §3.4 reports the results of the theory application and §3.5 the final discussion and possible

future investigations.

## 3.2 Theoretical background

Analogously to the pier case, when a turbulent open-channel flow interacts with a bridge abutment embedded in a mobile bed a complex flow field develops in the form of a downflow, a primary vortex system, a wake vortex system and a surface roller (Ettema et al., 2010; Dey, 2014) (Fig. 1(b)).

The downflow and the primary vortex are the main responsables of local scouring, owing to the fact that they contribute to generate strong shear stresses at the junction between the structure and the sediment bed. In clear-water conditions (i.e., for  $0.5 < U/U_c < 1$ , as reported by Breusers et al., 1977) and for steady impinging flows, the high shear stresses generated by the primary vortex contribute to erode the bed sediment and to form a scour hole, which progressively increases its size, until an equilibrium condition is achieved. The equilibrium condition is reached when the shear stress within the scour hole,  $\tau$ , approaches the critical shear stress for the inception of sediment motion,  $\tau_c$  (Ettema et al., 2010).

Following the approach of the previous Chapter, the analysis presented herein focuses on the deepest point of the scour hole, which is commonly observed at abutment nose, i.e., at the upstream corner of abutment (Radice et al., 2009). As reported in the previous Chapter, at this location and in equilibrium conditions, the local bed slope is known to be zero and therefore the critical shear stress,  $\tau_c$ , can be considered independent from slope effects (Unger & Hager, 2007; Kirkil et al., 2008).

The shear stress at the sediment-water interface,  $\tau$ , can be estimated

with relation 1.12, as reported by Gioia et al. (2010). In the abutment case, the scaling function  $\alpha_1$ , which appears in Eq. 2.5, keeps the same meaning as in the pier case, whereas  $V$  is the characteristic velocity of large-scale primary vortices.

As in the cases of open-channel or pipe flow and scouring phenomena,  $\alpha_1$  scales as the square root of the friction factor, which, in the fully-rough regime, is a function only of the ratio between the characteristic length scale of large eddies,  $L$ , and the sediment diameter,  $d$ . Relaxing the assumption of fully-rough regime,  $\alpha_1$  may also depend on the Reynolds number or, equivalently, on the roughness Reynolds number, here defined as  $d/\eta$ .

In addition, the local mean dissipation rate,  $\epsilon$ , can be related to the bulk dissipation rate,  $\epsilon_b$ , via the same *ad hoc* function,  $\alpha_2$ , as in Eq. 2.3.

Analogously to  $\alpha_1$ , even  $\alpha_2$  depends on the relative roughness,  $L/d$ , and the friction factor, meaning that, as for  $\alpha_1$ , also  $\alpha_2$  may depend on  $L/d$  and  $d/\eta$ .

Following Manes & Brocchini (2015), the characteristic velocity of the primary vortex,  $V$ , can be estimated from energetic considerations, as already done for the horseshoe vortex in the pier case. In fact, the bulk dissipation rate can be interpreted as the energy per unit time and unit mass (i.e., power,  $P$ , per unit mass,  $M$ ) of large-scale eddies, namely,  $\epsilon_b = P/M$ . Manes & Brocchini (2015), in the pier case, supposed that  $M$  scales as  $\rho L^3$ . This hypothesis, which is closely related to the scour volume and lies outside the PTT, is not needed if an original experimental dataset is available, in particular if the scour volumes are known. Therefore, considering the primary vortex fully embedded in the equilibrium scour hole (Raudkivi & Ettema, 1983),  $M$  scales as  $\rho V_{scour}$ , where  $V_{scour}$  is the scour hole volume

upstream to the abutment, namely, the volume of the primary vortex. The power,  $P$ , can be still expressed as the work per unit time of the drag force exerted by the flow on the structure portion exposed to scour. In turn, it can be quantified as the product between the average approaching flow velocity,  $U$ , and the drag force,  $F = 0.5\rho C_d b_{eff} L U^2$ , where  $b_{eff}$  is the aforementioned effective transversal width of the abutment and  $b_{eff} L$  the frontal area of the abutment directly exposed to scour. In the abutment case, and in particular for long abutments, the length scale  $b_{eff}$  has a blurry definition, because part of the abutment drag work is spent to generate a recirculation counter-rotating region (with bed-normal vorticity), that occurs in proximity of the bank-abutment junction (Kwan, 1984; Melville, 1997). Therefore, in simple terms it is necessary to define a  $b_{eff}$  that allows a drag work partitioning which captures the energy of the primary vortex only. Towards this end, a natural candidate for  $b_{eff}$  is the abutment width minus the size of the aforementioned counter-rotating region, unknown a priori. Hence, from Eq. 2.3:

$$\epsilon = \alpha_2^3 \frac{V^3}{L} = \alpha_2^3 \frac{0.5\rho C_d b_{eff} L U^3}{\rho V_{scour}} \quad (3.1)$$

and the characteristic velocity,  $V$ , scales as:

$$V \sim U \left( \frac{C_d b_{eff} L^2}{V_{scour}} \right)^{1/3}. \quad (3.2)$$

Coupling relations 1.12 and 3.2 and Eq. 2.1, the shear stress,  $\tau$ , can be estimated as follows:

$$\tau \sim \rho \alpha_1 U \left( \frac{C_d b_{eff} L^2}{V_{scour}} \right)^{1/3} w_l. \quad (3.3)$$

From the previous Chapter, it is obtained that, for small values of  $d/\eta$ , the  $w_l$  coming from a structure-function model (Eq. 2.9) can be approximated as  $w_d$  (Eq. 2.13); also for low values of relative roughness, when the rate of momentum transfer,  $w_l$ , is indicated as  $w_d^P$ , it is approximately equal to  $w_d$  (Eq. 2.26):

$$w_l \approx w_d \sim (\epsilon d)^{1/3}. \quad (3.4)$$

Inserting Eq. 3.1 into the previous relation, one obtains:

$$w_l \approx w_d \sim \alpha_2 U \left( \frac{C_d b_{eff} L d}{V_{scour}} \right)^{1/3}. \quad (3.5)$$

Therefore, inserting relation 3.5 in 3.3, the shear stress,  $\tau$ , results:

$$\tau \sim \alpha_1 \alpha_2 \rho U^2 \left( \frac{C_d b_{eff} L^2}{V_{scour}} \right)^{2/3} \left( \frac{d}{L} \right)^{1/3} \quad (3.6)$$

In clear-water and uniform flow conditions,  $L$  approaches the equilibrium scour depth  $y_{se}$  (because, analogously to the horseshoe vortex, the primary vortex is commonly assumed to be fully-buried within the scour hole), and the wall shear stress,  $\tau$ , approaches the critical shear stress corresponding to the onset of sediment mobility and transport,  $\tau_c = \theta(\rho_s - \rho)gd$  (Shields, 1936). Hence:

$$\alpha_1 \alpha_2 \rho U^2 \left( \frac{C_d b_{eff} y_{se}^2}{V_{scour}} \right)^{2/3} \left( \frac{d}{y_{se}} \right)^{1/3} = \theta(\rho_s - \rho)gd \quad (3.7)$$

and, after some algebraic passages:

$$\frac{V_{scour}^{2/3} g}{y_{se} U^2} = \frac{\alpha_1 \alpha_2}{\theta} \frac{\rho}{\rho_s - \rho} C_d^{2/3} \left( \frac{b_{eff}}{d} \right)^{2/3}. \quad (3.8)$$



As reported in the previous Chapter, the ratio  $\theta/(\alpha_1\alpha_2)$  is a function of the relative roughness, that in the abutment case is represented by  $b_{eff}/d$  and  $d/\eta_1$ . Consequently, Eq. 3.8 can be modified as follows:

$$\frac{V_{scour}^{2/3}g}{y_{se}U^2} = \frac{\frac{\rho}{\rho_s - \rho} C_d^{2/3} \left(\frac{b_{eff}}{d}\right)^{2/3}}{f\left(\frac{d}{\eta_1}, \frac{b_{eff}}{d}\right)}. \quad (3.9)$$

Note that it would be useful to know a closure equation for the volume of scour in order to use Eq. 3.9 for the  $y_{se}$  assessment. The novelty of the above revisited theory with respect to that for the pier case is the presence of the effective length  $b_{eff}$  and the scour volume  $V_{scour}$  in the maximum scour depth predictive formula. In fact, in the pier theory  $b_{eff}$  is simply the pier diameter, whereas, from dimensional considerations,  $V_{scour}$  is considered as proportional to  $y_{se}^3$ . For this reason, an *ad hoc* experimentation is requested in order to validate Eq. 3.9.

### 3.3 Experimental setup and procedure

The experiments were carried out at the *Laboratorio "Grandi Modelli Idraulici"* (GMI), *Università della Calabria*, Italy. In the next subsection, the experimental facilities and procedures are reported.

#### 3.3.1 Facilities

The experiments were conducted in a recirculating 1 m wide, 0.8 m deep, 18 m long horizontal flume with rectangular cross-section. Fig. 3.1(a) gives an overall view of the installation. The flume inlet consisted of a stilling tank, an uphill slipway, a perforated-pipe diffuser, a fine grid and a honeycomb to



**Figure 3.1:** Flume details; (a) picture of the installation; (b) honeycomb and details of the triangular pipes.

damp the residual pump vibrations. The honeycomb was made by polycarbonate triangular pipes and was 40 cm long (Fig. 3.1(b)). An adjustable tailgate was placed at the outlet in order to set the water depth. The water depth was measured with a point gauge with a decimal Vernier (accuracy of 0.1 mm) .

At the outlet, water was accumulated in a downstream tank, from which it fell in a restitution channel, where another honeycomb and a Bazin weir, with an accuracy of 2%, were placed to measure the discharge before pumping it again towards the flume inlet. The Bazin weir available at the *Lab. GMI* has the following characteristics: height measured starting from the



**Figure 3.2:** Bazin weir used to measure the discharge.

bed  $p_w = 0.35$  m, measured length of the weir crest  $L_w = 0.995$  m, thickness of the plate equal to 5 mm, thickness of the crest of the plate equal to 1.5 mm. The Bazin weir is allocated at the end of the restitution channel, which is 15 m long, 1 m wide and 1 m deep. The Bazin weir used in the experiments is depicted in Fig. 3.2.

In order to measure the water head, a piezometer was connected to the restitution channel, 50 cm upstream of the Bazin weir, and a point gauge with decimal Vernier (accuracy of 0.1 mm) was used to measure the level inside it (Fig. 3.3). Another point gauge with decimal Vernier was installed in the restitution channel and was used to assess the zero level,  $z_0$ , i.e., the water level reached in the piezometer when it is corresponding to the Bazin crest.

The discharge was determined with the formula proposed by Kindsvater & Carter (1959):

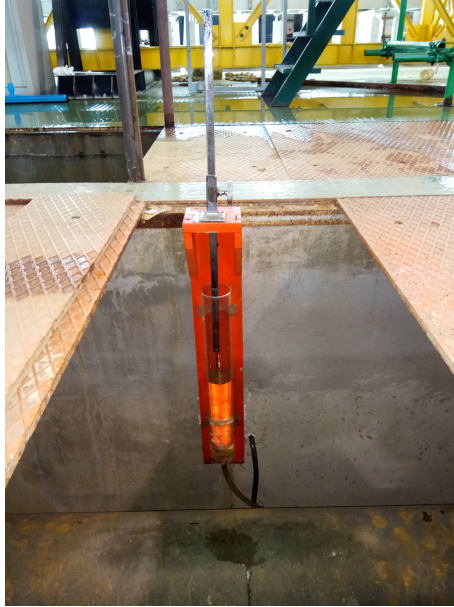


**Figure 3.3:** Point gauge fitted with decimal Vernier placed in the piezometer.

$$Q = C_e L_{we} h_{we}^{3/2} \quad (3.10)$$

where  $Q$  is expressed in  $\text{m}^3/\text{s}$ ,  $C_e$  the effective discharge coefficient computed as  $1.78 + 0.22(h_w/p_w)$ , expressed in  $\text{m}^{1/2}/\text{s}$ ,  $h_w$  the head measured above the weir crest using the point gauge,  $L_{we}$  the effective length of weir crest equal to  $L_w + 0.001$  m and  $h_{we}$  the effective head measured above the weir crest, equal to  $h_w + 0.001$  m.

The water level, measured with the point gauge inside the piezometer, must be referred to weir crest. To determine the reference “zero” value, the following preliminary procedure should be performed:

- a hydrostatic condition is to be obtained in which the water level in

the restitution channel is equal to that in the piezometer;

- the elevation of the weir crest is to be measured with the point gauge with decimal Vernier installed on a gantry placed on the walls of the restitution channel ( $h_c$ );
- the elevation of the water surface is to be measured with the aforementioned point gauge by moving the gantry 50 cm upstream to the weir crest ( $h_{c50}$ );
- the piezometer water level is to be measured with the point gauge inside the piezometer ( $h_{p,in}$ , where the subscript “*in*” indicates “initial”).

The “zero” value of the Bazin weir is obtained as follows:

$$z_0 = h_{p,in} + h_c - h_{c50}. \quad (3.11)$$

In order to determine the water head above the crest during the runs,  $h_w$ , it is only necessary to measure the level of the free surface in the piezometer connected to the restitution channel, indicated as  $h_{p,run}$ :

$$h_w = h_{p,run} - z_0. \quad (3.12)$$

In the flume a 2.5 m long, 30 cm deep recess box was located at about 11.5 m from the inlet. The recess box was filled in with 4 uniform sediments (i.e., with the geometric standard deviation,  $\sigma_g = (d_{84}/d_{16})^{0.5} < 1.5$  as reported by Dey & Sarkar (2006)) having different median diameter  $d_{50}=0.69$  mm (coarse sand),  $d_{50}=1.53$  mm (very coarse sand),  $d_{50}=2.82$  mm (very fine gravel) and  $d_{50}=4.81$  mm (fine gravel)(Lane (1947); Fig. 3.4).

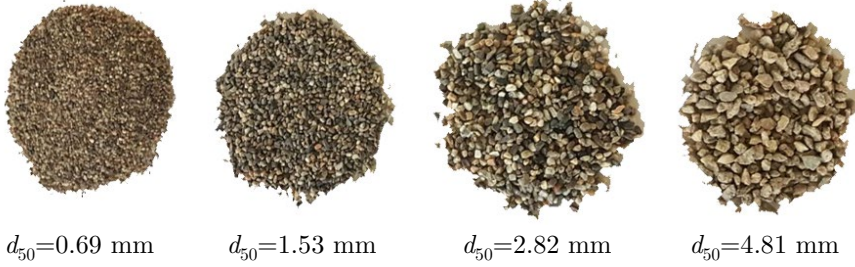


**Figure 3.4:** Uniform sediments used in the recess box.

In order to reach a fully developed turbulence at the recess box location, the flume bed upstream to the recess box was divided in 4 reaches, each one constituted by a 2.5 cm thick layer of uniform sediment, with progressively decreasing roughness and a median diameter  $d_{50}=17.98$  mm (coarse gravel),  $d_{50}=10.55$  mm (medium gravel),  $d_{50}=6.49$  mm (fine gravel) and  $d_{50}=4.81$  mm (fine gravel) (Lane (1947); Fig. 3.5).

Sixteen runs (named as Run 1 to Run 16) were carried out by using 4 Plexiglas<sup>®</sup> abutments of different transversal length ( $b=15, 20, 25$  and  $30$  cm, respectively), thickness of 5 cm and height of 70 cm (Fig. 3.6).

Furthermore, an Acoustic Doppler Velocimeter (ADV) down-looking probe with four beams (Nortek Vectrino<sup>®</sup>) and with an automatic movement system (the Traverse System by HR Wallingford Ltd., UK), shown in Fig. 3.7, was used to capture: 1) spatially distributed flow field measurements with an accuracy of 5% (assessed in previous works), a sampling frequency of 100 Hz and the duration of a single sampling of 180 s, for a total number of 18000 samples. Each sampling volume was 5.5 mm long with a 6 mm diameter ( $\approx 155$  mm<sup>3</sup>) (Fig. 3.8); 2) bed elevations with 0.1 mm of accuracy; 3) the temperature measured with an integrated thermometer with an

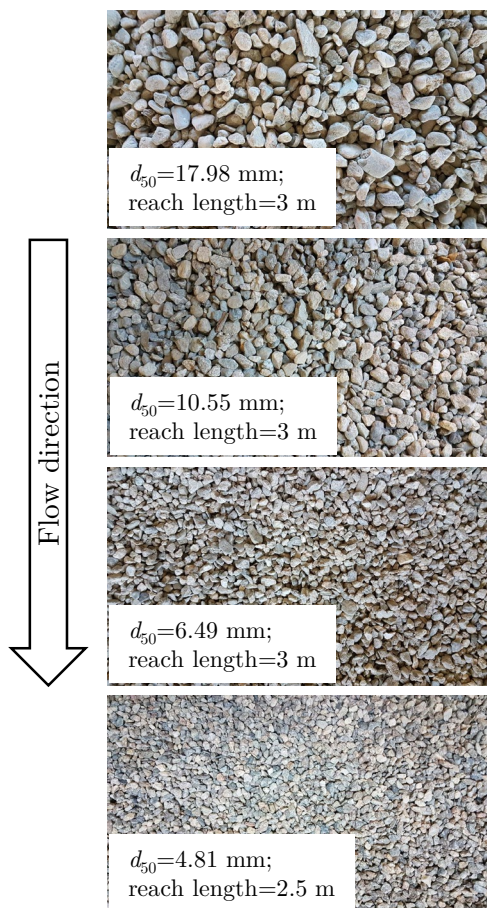


**Figure 3.5:** Flume bed upstream to the recess box divided in 4 reaches.

accuracy of 0.1 °C. The spatial coordinate of the Traverse System has an accuracy of 0.1 mm.

### 3.3.2 Preliminary tests

A series of preliminary tests was conducted in order to verify the condition of fully developed turbulence at the recess box location. First of all, the turbulence intensity was computed as follows:

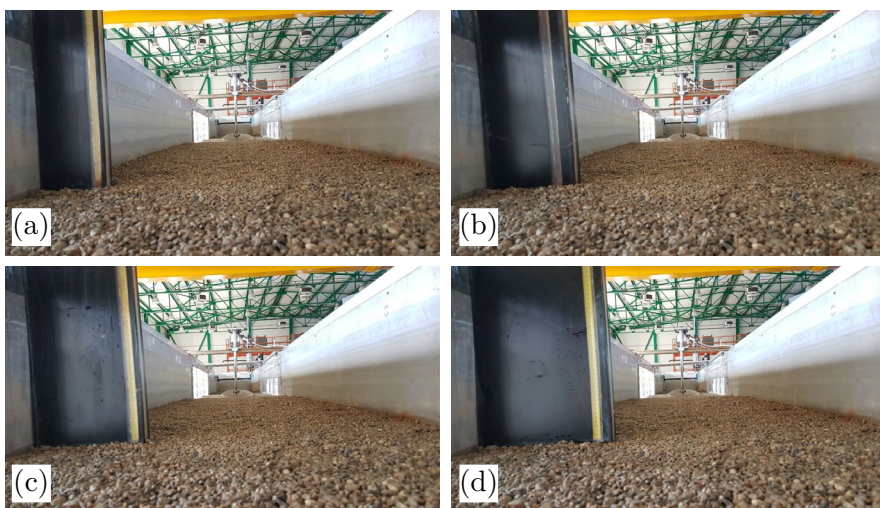


**Figure 3.6:** Abutment models: (a)  $b = 15$  cm, (b)  $b = 20$  cm, (c)  $b = 25$  cm and (d)  $b = 30$  cm.

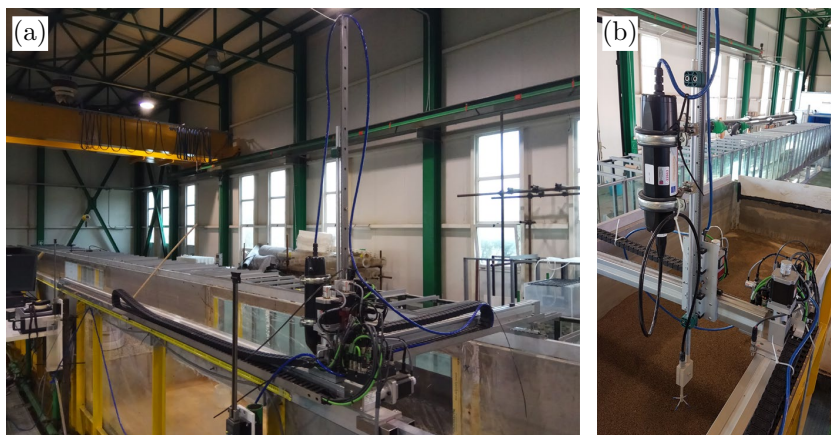


**Figure 3.7:** (a) Traverse System; (b) ADV down-looking probe.

$$T_u = \frac{u_{rms}}{U} \cdot 100 \quad (\%) \quad (3.13)$$



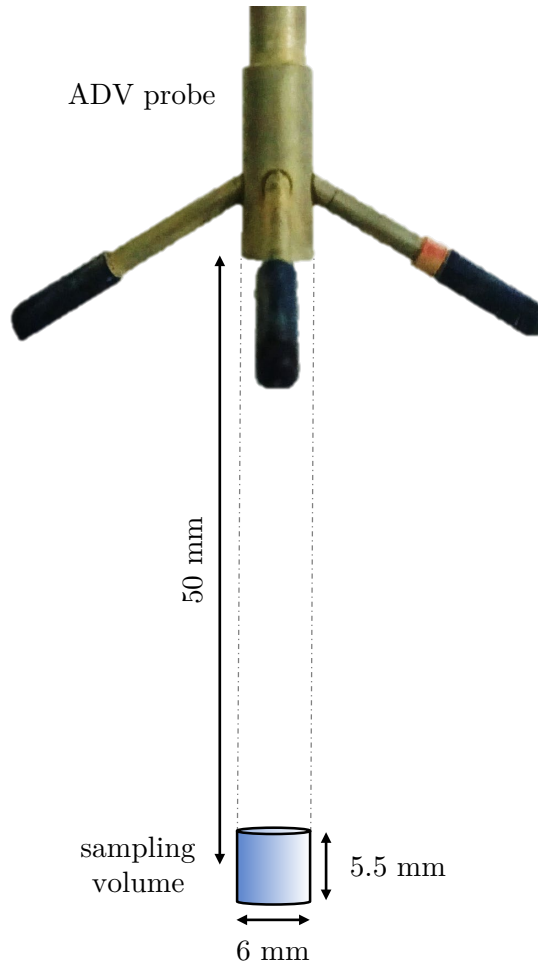


**Figure 3.8:** ADV probe and sampling volume.

where  $u_{rms}$  is the root mean square (rms) of streamwise velocity component. The turbulence intensity was calculated taking an ADV measure near the inlet out of the turbulent boundary layer (at a half of the water depth and 0.5 m downstream of the honeycomb). In such position, the velocity signal is an indicator of the incoming turbulence generated by the pump-inlet pipe

system. Firstly, the values of  $T_u$  were computed in a configuration without any tool to reduce the incoming turbulence; secondly, in a configuration compound by a perforated-pipe diffuser, a fine grid and a honeycomb. The  $T_u$  resulted equal to 16.91% and 3.68%, respectively. The second configuration presents an acceptable value of  $T_u$ . Furthermore, as reported in a previous work done in the same laboratory flume (Coscarella et al., 2017), the similarity in the velocity profiles was observed 4 m downstream of the inlet and typically open-channel flow statistics was found 50 cm upstream to the sediment box location. Hence, the sediment box is far enough to guarantee the complete dissipation of the incoming turbulence, which is replaced by the turbulence generated by the rough bed.

### 3.3.3 Design of the runs

In the present study, the runs were designed in order to ensure, for a flow depth of 15 cm measured at a distance of about 1 m upstream to the abutment, a flow intensity  $U/U_c = 0.90$  or  $0.75$ , respectively, depending on the median diameter of the bed material in the recess box. The experimental conditions are reported in Tab. 3.1 where the critical velocity for the inception of sediment motion,  $U_c$ , was assessed preliminarily from classical empirical formulae (Goncharov (1964), Eq. 3.14; Neill (1968), Eq. 3.15; Garde (1968), Eq. 3.16):

$$U_c = 1.07 \left( \frac{\rho_s - \rho}{\rho} g d_{95} \right)^{0.5} \log \left( 8.8 \frac{h}{d_{95}} \right) \quad (3.14)$$

where subscript 95 denotes the percentage finer;

$$U_c = 1.41 \left( \frac{\rho_s - \rho}{\rho} g d_{50} \right)^{0.5} \left( \frac{h}{d_{50}} \right)^{1/6}; \quad (3.15)$$

$$U_c = \left( \frac{\rho_s - \rho}{\rho} g d_{50} \right)^{0.5} \log \left( 0.5 \frac{h}{d_{50}} + 1.63 \right). \quad (3.16)$$

A more accurate estimation of  $U_c$  was also carried out by direct observation of the threshold of the inception of sediment motion. In this case, a test series was performed for all the particle sizes and without abutments. In these tests the tailgate was raised up and, after measuring the discharge,  $Q$ , it was slowly decreased until the approach flow depth of 15 cm was achieved in the channel. In fact, all the Runs presented in Tab. 3.1 were performed with  $h = 15$  cm and different approach velocities. After each observation, the discharge was increased and the tailgate was again pushed down to regulate the 15 cm approach flow depth.

All the tests were carried out in clear-water conditions ( $U < U_c$ ).

### 3.3.4 Experimental procedure

At the beginning of each experiment, the first phase consisted in the bed preparation, positioning the abutment model and then levelling the bed. After filling the recess box with sediments, the bed was compacted manually and then an aluminum bar and a trowel were used to level the sediment bed at the same elevation of the false floors.

Starting the experiment is a delicate phase, since during the first part of the experiments the scouring rate at the abutment is high. In order to avoid bed disturbances, the flume was filled in slowly by using a hose with a discharge of about 2 l/s.

Table 3.1: Experimental conditions.

Run	$d_{50}$ (mm)	$\sigma_g$	$b$ (m)	$h$ (m)	$\rho_s$ (kg/m <sup>3</sup> )	$Q$ (l/s)	$U$ (m/s)	$U_c$ (m/s)	$U/U_c$
1	0.69	1.38	0.30	0.15	2660	30.5	0.295	0.328	0.90
2	0.69	1.38	0.25	0.15	2660	32.8	0.295	0.328	0.90
3	0.69	1.38	0.20	0.15	2660	35.0	0.295	0.328	0.90
4	0.69	1.38	0.15	0.15	2600	37.3	0.295	0.328	0.90
5	1.53	1.24	0.30	0.15	2680	40.3	0.395	0.438	0.90
6	1.53	1.24	0.25	0.15	2680	43.3	0.395	0.438	0.90
7	1.53	1.24	0.20	0.15	2680	46.4	0.395	0.438	0.90
8	1.53	1.24	0.15	0.15	2680	49.5	0.395	0.438	0.90
9	2.82	1.42	0.30	0.15	2670	42.0	0.414	0.544	0.75
10	2.82	1.42	0.25	0.15	2670	45.2	0.414	0.544	0.75
11	2.82	1.42	0.20	0.15	2670	48.5	0.414	0.544	0.75
12	2.82	1.42	0.15	0.15	2670	51.8	0.414	0.544	0.75
13	4.81	1.18	0.30	0.15	2710	49.5	0.493	0.662	0.75
14	4.81	1.18	0.25	0.15	2710	53.3	0.493	0.662	0.75
15	4.81	1.18	0.20	0.15	2710	57.2	0.493	0.662	0.75
16	4.81	1.18	0.15	0.15	2710	61.2	0.493	0.662	0.75

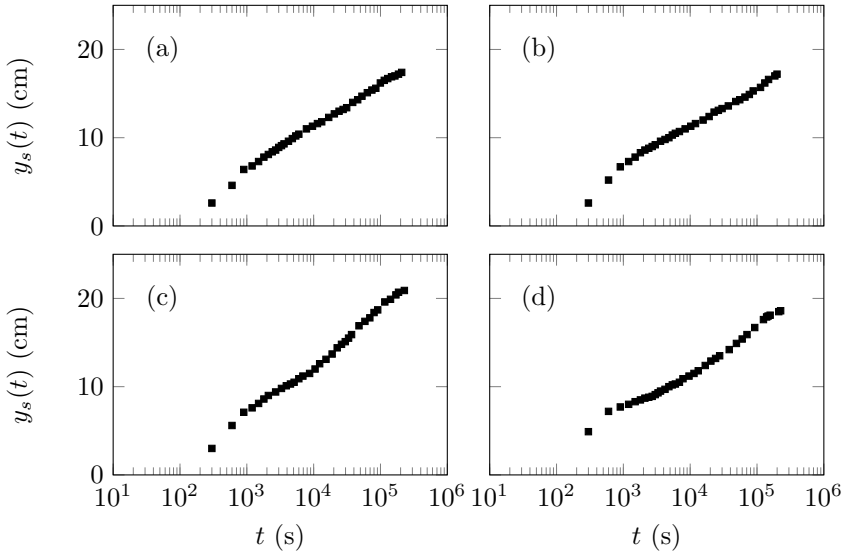


**Figure 3.9:** Time evolution of the scour depth  $y_s(t)$  for: (a) Run 1; (b) Run 2; (c) Run 3; (d) Run 4.

The ADV was used to acquire the bed elevations in order to investigate the maximum scour depth evolution over time. The ADV probe was placed at the expected maximum scour depth location, i.e., approximately at the abutment upstream corner (Melville & Coleman, 2000), as observed in preliminary tests. In order to guarantee equilibrium conditions, according to Coleman et al. (2003) procedure, the test duration was set as the time at which the rate of maximum scour depth reduces to 5% of the abutment transverse length in 24 h. The maximum scour depth evolution over time,  $y_s$ , is plotted as a function of time,  $t$ , in Figs. 3.9-3.12.

To estimate the maximum scour depth,  $y_{se}$ , and the scour volume,  $V_{scour}$ , at the end of all runs, the topography of the eroded surface was digitised using a photogrammetric technique. The choice of this technique, with respect

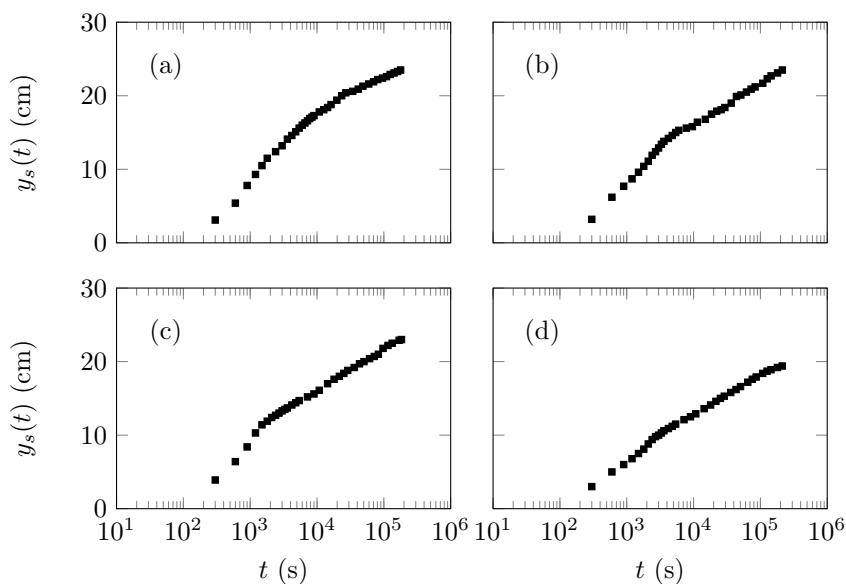


**Figure 3.10:** Time evolution of the scour depth  $y_s(t)$  for: (a) Run 5; (b) Run 6; (c) Run 7; (d) Run 8.

to the 3D laser scanning, is due to its velocity in processing the 3D model, despite that, as reported below, a 3D laser scanning must be realized in order to assign spatial coordinate to photogrammetric 3D model (Baltsavias, 1999). This technique is based on the principle that a 3D model reconstruction can be obtained from still images. Moreover, the process is based on the possibility that the photographs can be taken from any position, providing that the surface to be reconstructed is visible on at least two photographs.

In this work, the Agisoft PhotoScan<sup>®</sup> was used for fully automated image alignment and 3D model reconstruction. The photographs were taken using a Nikon<sup>®</sup> D3000 camera with a Nikon<sup>®</sup> AF-S DX Zoom-Nikkor 18-55 mm lens (Fig. 3.13(a)). The procedure for the bed surface acquisition consisted in the following steps:

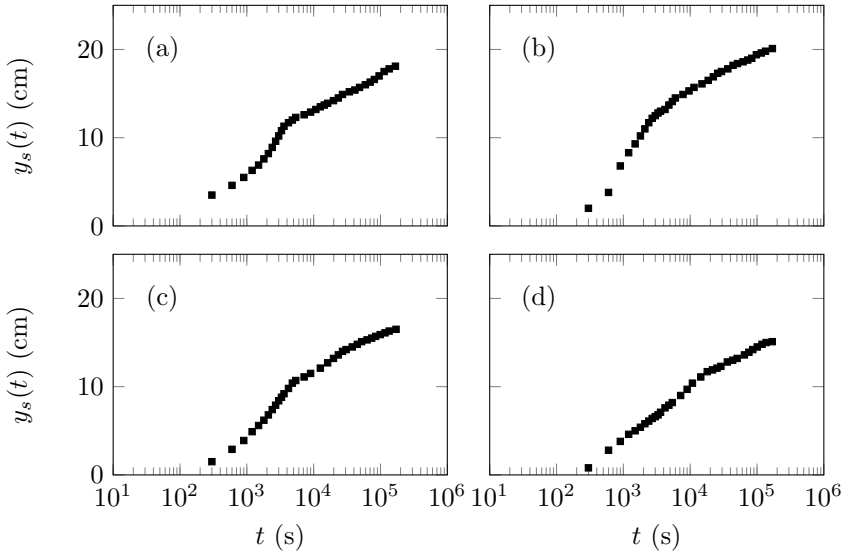


**Figure 3.11:** Time evolution of the scour depth  $y_s(t)$  for: (a) Run 9; (b) Run 10; (c) Run 11; (d) Run 12.

- photogrammetric targets (Fig. 3.13(b)) were placed on the internal side of the channel walls;
- four sets of photographs were taken, specifically from the left and right channel wall and in both the upstream and downstream directions, with camera positions oriented with an angle of about  $45^\circ$  with respect to the vertical direction, looking downwards at the scour hole; 25 photographs with spacing of 10 cm were approximately taken for each set;
- the photographs were uploaded on Agisoft PhotoScan<sup>®</sup>, that searches for common points of photogrammetric targets on photographs and matches them, as well as finds the position of the camera for each picture and refines camera calibration parameters. As a result, a sparse

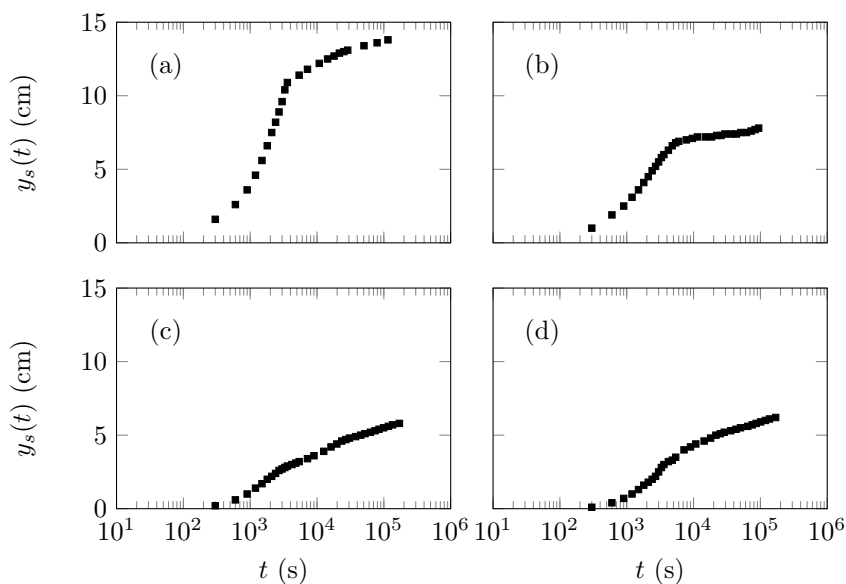


**Figure 3.12:** Time evolution of the scour depth  $y_s(t)$  for: (a) Run 13; (b) Run 14; (c) Run 15; (d) Run 16.

point cloud and a set of camera positions are formed (Fig. 3.14);

- dense point cloud is built by the software based on the estimated camera positions and pictures themselves; dense point cloud may be edited, for example eliminating the points out the scour surface (Fig. 3.15);
- the channel was scanned by using the Laser Scanner **Leica ScanStation P20<sup>®</sup>** with an accuracy of 1 mm (Fig. 3.13(c)); in fact, the laser scanning, which is characterized by space coordinates, was used to scale the 3D dense cloud derived from the photogrammetric software;
- the mesh was built (Fig. 3.16); **Agisoft PhotoScan<sup>®</sup>** reconstructs a 3D polygonal mesh representing the object surface, based on the dense cloud. The 3D polygonal meshes of all Runs are reported in



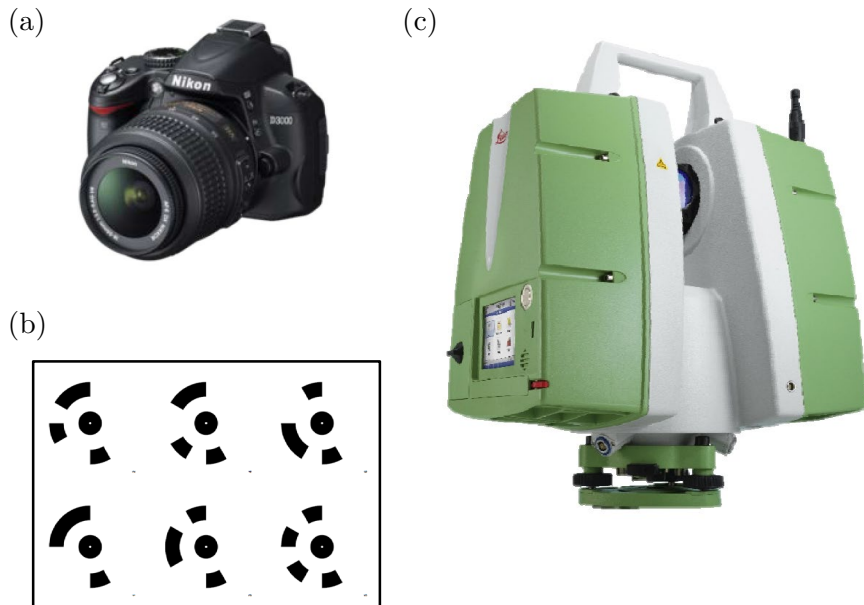


**Figure 3.13:** (a) Nikon<sup>®</sup> D3000 camera with a Nikon<sup>®</sup> AF-S DX Zoom-Nikkor 18-55 mm lens; (b) photogrammetric targets; (c) Laser Scanner Leica ScanStation P20<sup>®</sup>.

Figs. 3.17-3.32.

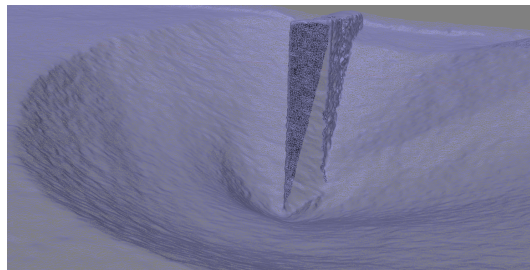


**Figure 3.16:** Example of wireframe view of a 3D polygonal mesh detail.

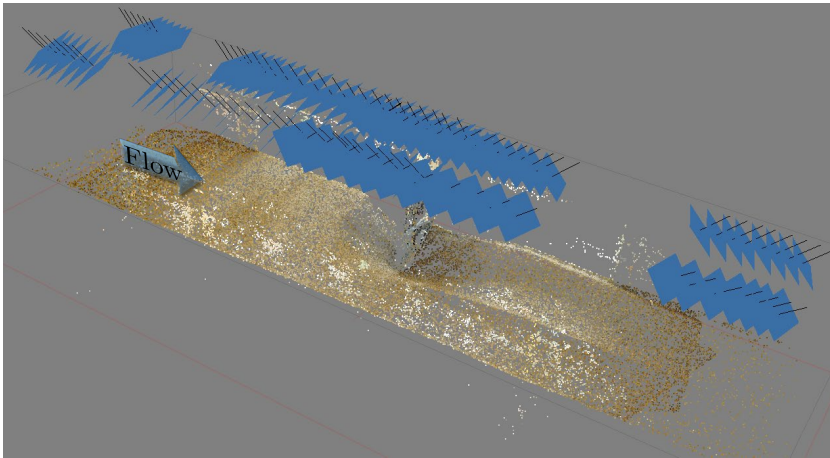


**Figure 3.14:** Example of 3D sparse point cloud of eroded bed captured through photogrammetric technique. The camera positions are identified by blue polygons.

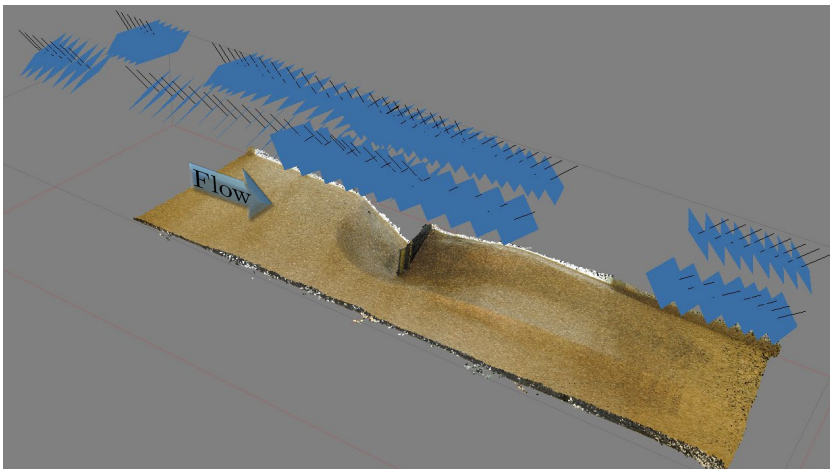


**Figure 3.15:** Example of 3D edited dense point cloud of eroded bed captured through photogrammetric technique. The camera positions are identified by blue polygons.



Figure 3.17: 3D polygonal mesh of Run 1.

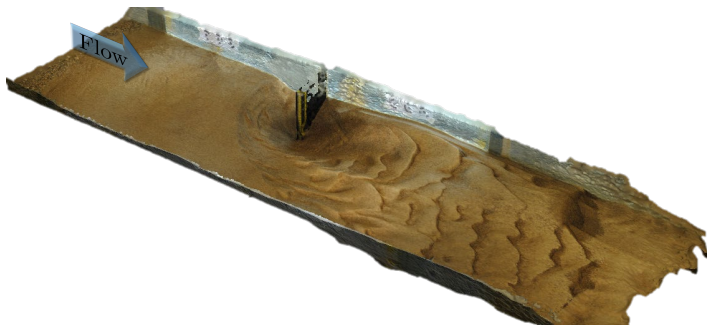


Figure 3.18: 3D polygonal mesh of Run 2.



Figure 3.19: 3D polygonal mesh of Run 3.



Figure 3.20: 3D polygonal mesh of Run 4.



Figure 3.21: 3D polygonal mesh of Run 5.



Figure 3.22: 3D polygonal mesh of Run 6.



Figure 3.23: 3D polygonal mesh of Run 7.



Figure 3.24: 3D polygonal mesh of Run 8.

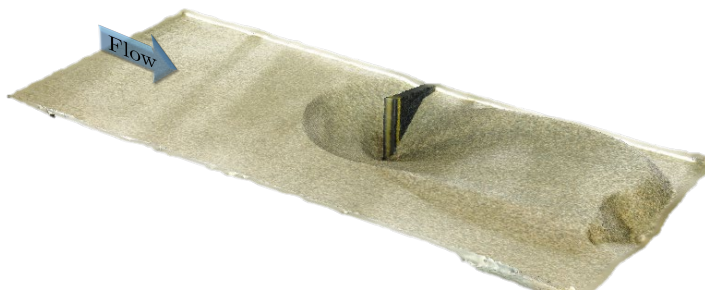


Figure 3.25: 3D polygonal mesh of Run 9.



Figure 3.26: 3D polygonal mesh of Run 10.



Figure 3.27: 3D polygonal mesh of Run 11.



Figure 3.28: 3D polygonal mesh of Run 12.



**Figure 3.29:** 3D polygonal mesh of Run 13.



**Figure 3.30:** 3D polygonal mesh of Run 14.



**Figure 3.31:** 3D polygonal mesh of Run 15.



**Figure 3.32:** 3D polygonal mesh of Run 16.

- finally, the data were transferred to a uniform grid with a sampling distance of 5 mm by using the software **Rhinoceros**<sup>®</sup>. Thus, a **Matlab**<sup>®</sup> code was developed to analyse the bed surface topography and, in particular, to measure  $V_{scour}$  and  $y_{se}$ .

Figs. 3.33 to 3.48 show the contourlines of the equilibrium scour holes for Runs 1 to 16, respectively.



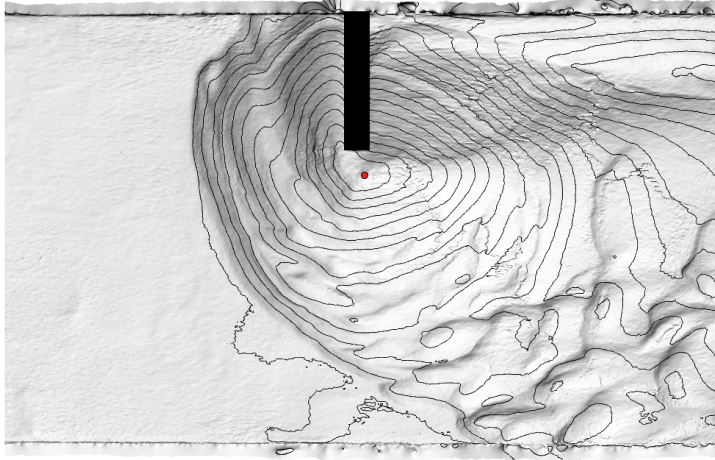


**Figure 3.33:** Plan view of the 3D models and contours of the bed surface topography for Run 1. The red point and the black rectangle indicate the position of the maximum scour depth,  $y_{se}$ , and of the abutment, respectively. Analogously for Figs. 3.34 to 3.48.

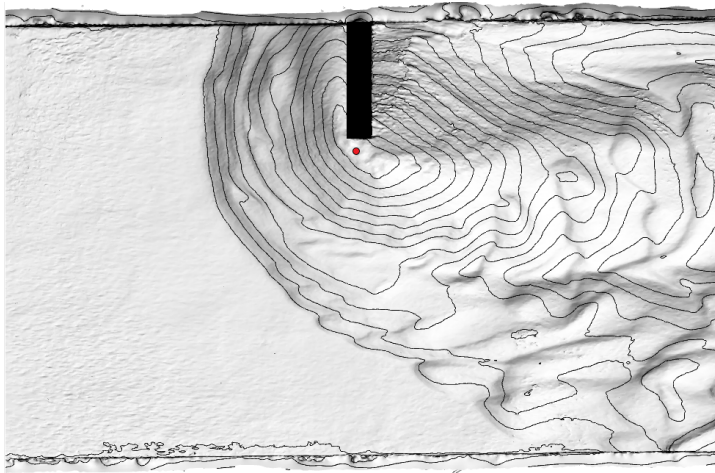


**Figure 3.34:** Plan view of the 3D models and contours of the bed surface topography for Run 2.

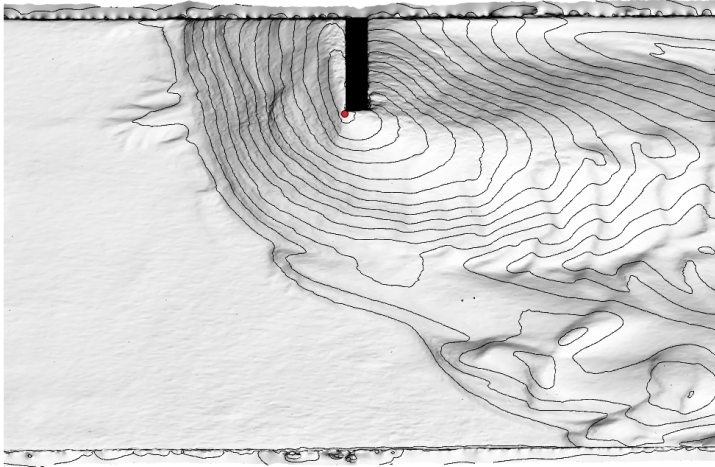


**Figure 3.35:** Plan view of the 3D models and contours of the bed surface topography for Run 3.

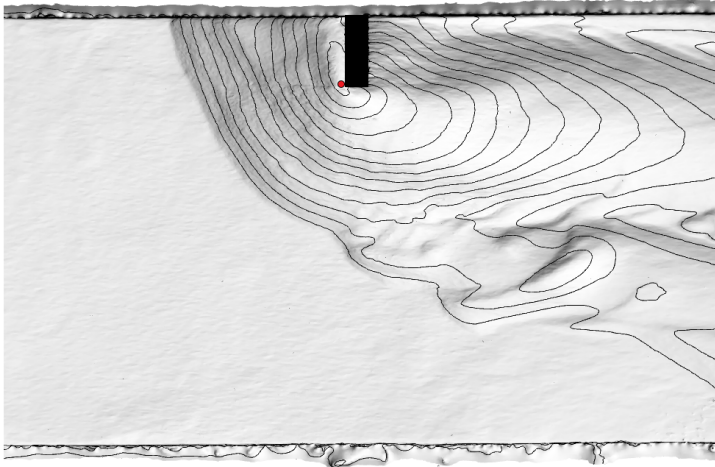


**Figure 3.36:** Plan view of the 3D models and contours of the bed surface topography for Run 4.

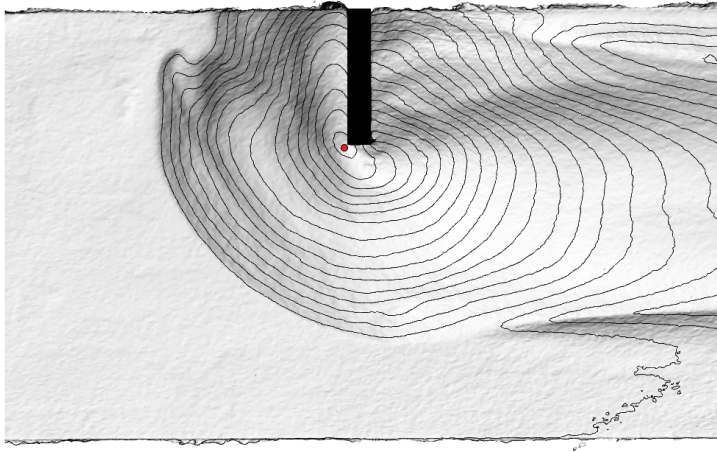


**Figure 3.37:** Plan view of the 3D models and contours of the bed surface topography for Run 5.

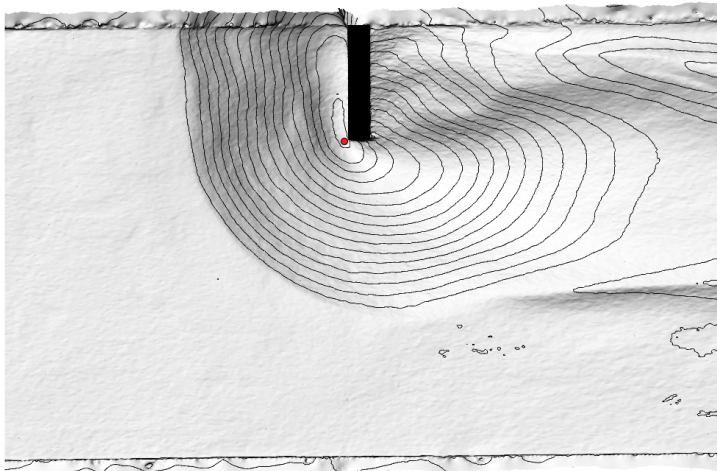


**Figure 3.38:** Plan view of the 3D models and contours of the bed surface topography for Run 6.

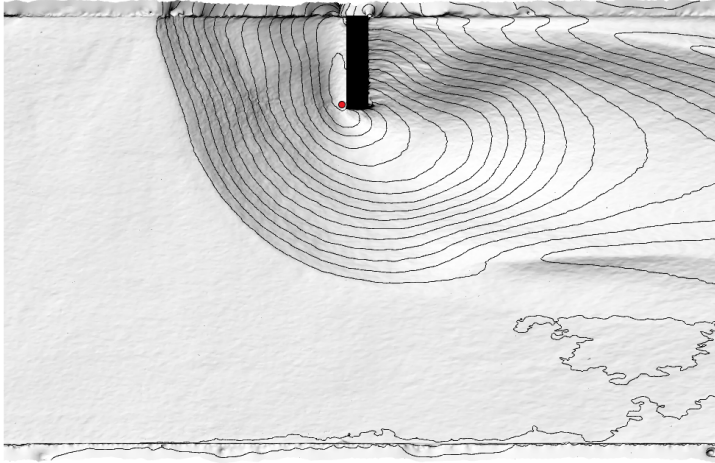


**Figure 3.39:** Plan view of the 3D models and contours of the bed surface topography for Run 7.

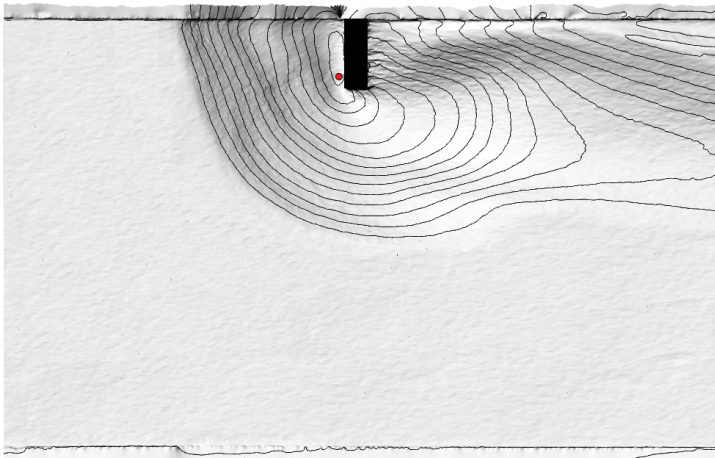


**Figure 3.40:** Plan view of the 3D models and contours of the bed surface topography for Run 8.

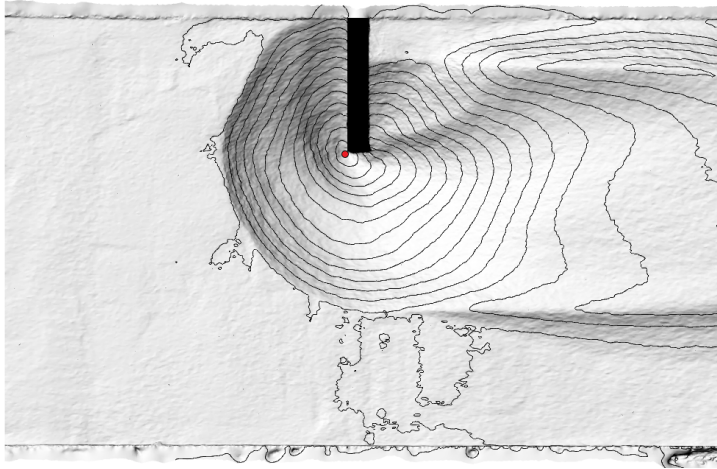


**Figure 3.41:** Plan view of the 3D models and contours of the bed surface topography for Run 9.

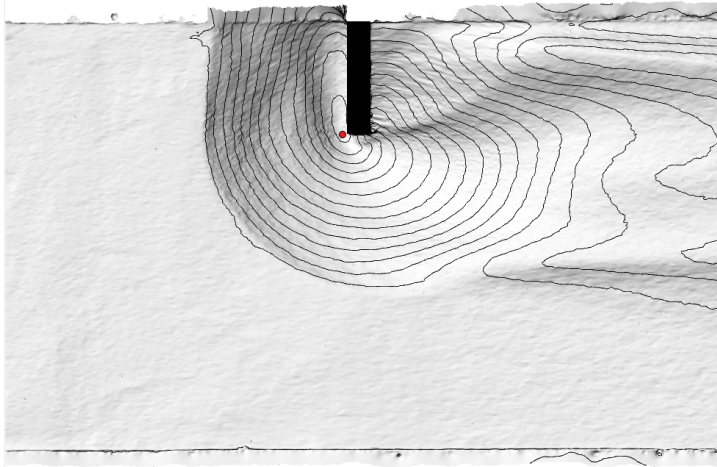


**Figure 3.42:** Plan view of the 3D models and contours of the bed surface topography for Run 10.

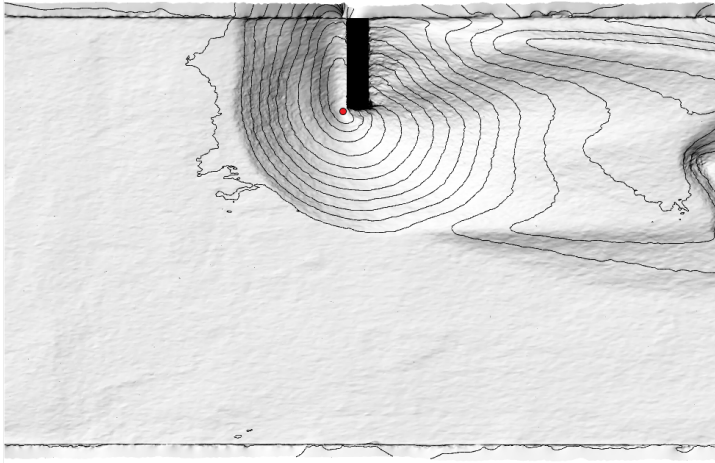


**Figure 3.43:** Plan view of the 3D models and contours of the bed surface topography for Run 11.

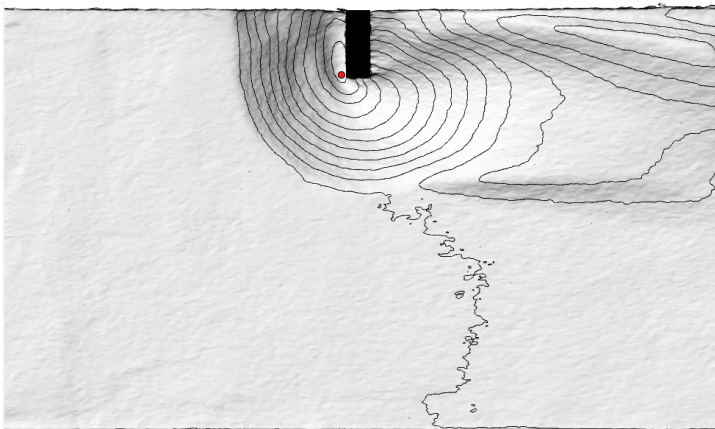


**Figure 3.44:** Plan view of the 3D models and contours of the bed surface topography for Run 12.

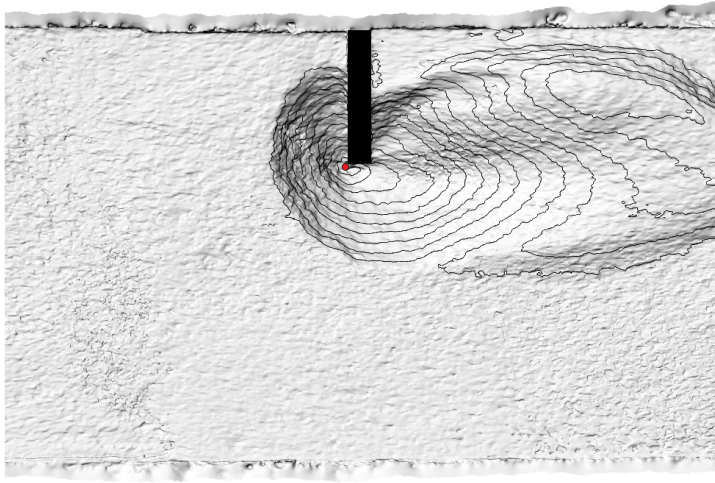


**Figure 3.45:** Plan view of the 3D models and contours of the bed surface topography for Run 13.

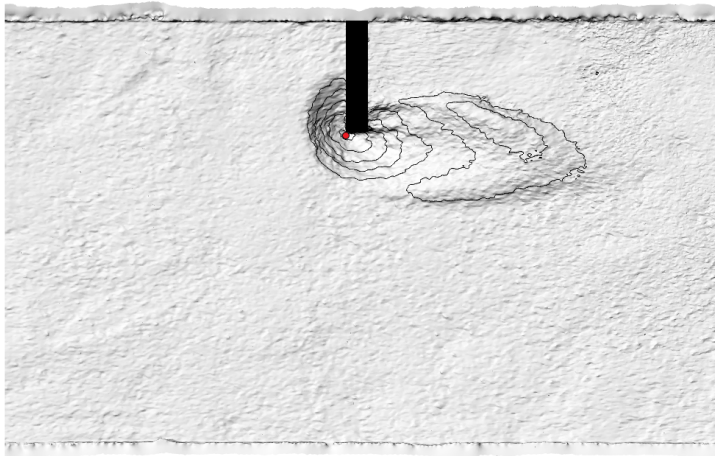


**Figure 3.46:** Plan view of the 3D models and contours of the bed surface topography for Run 14.

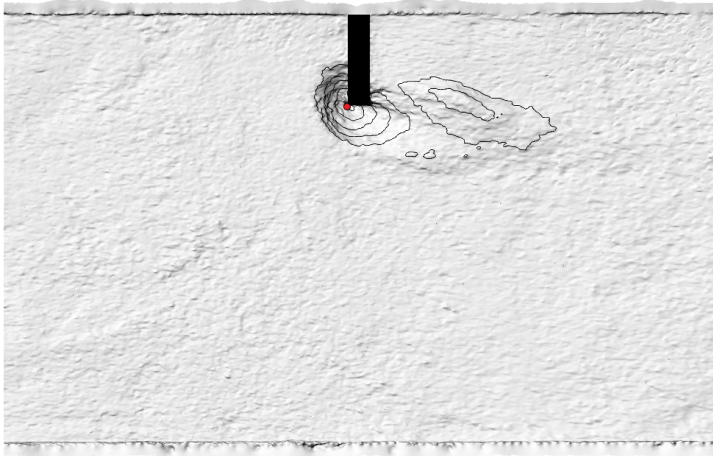


**Figure 3.47:** Plan view of the 3D models and contours of the bed surface topography for Run 15.

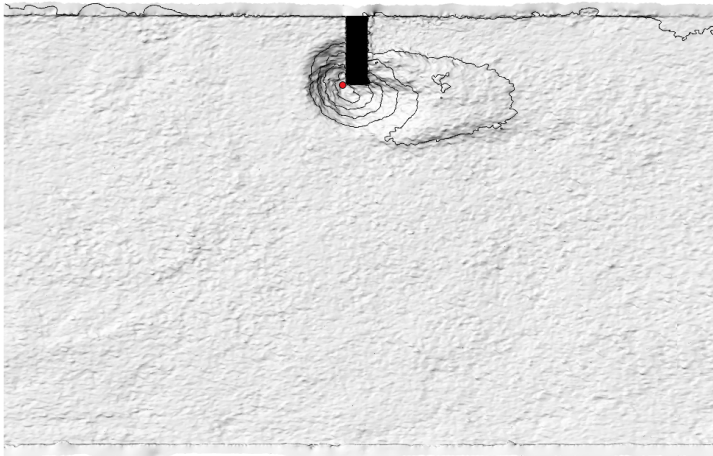


**Figure 3.48:** Plan view of the 3D models and contours of the bed surface topography for Run 16.

The experimental characteristics in equilibrium conditions are reported in Tab. 3.2.



**Table 3.2:** Experimental characteristics in equilibrium conditions;  $t$  is time to equilibrium,  $T$  the average temperature during the run,  $\nu$  the kinematic viscosity computed as a function of  $T$  (expressed in °C) as  $[1.14 - 3.1 \cdot 10^{-2}(T - 15) + 6.8 \cdot 10^{-4}(T - 15)^2] \cdot 10^{-6}$  m<sup>2</sup>/s (Julien, 1998).

Run	$y_{se}$ (m)	$V_{scour}$ (m <sup>3</sup> )	$t$ (min)	$T$ (°C)	$\nu$ (m <sup>2</sup> /s)
1	0.196	0.0021	3460	20.57	$0.988 \cdot 10^{-6}$
2	0.191	0.0072	3320	17.10	$1.077 \cdot 10^{-6}$
3	0.220	0.0139	3790	20.18	$0.997 \cdot 10^{-6}$
4	0.197	0.0114	3760	18.82	$1.031 \cdot 10^{-6}$
5	0.225	0.0023	2970	20.75	$1.012 \cdot 10^{-6}$
6	0.249	0.0051	3550	22.27	$0.987 \cdot 10^{-6}$
7	0.241	0.0221	3060	20.62	$0.951 \cdot 10^{-6}$
8	0.217	0.0192	3540	19.59	$0.984 \cdot 10^{-6}$
9	0.192	0.0030	2790	17.55	$1.065 \cdot 10^{-6}$
10	0.201	0.0150	2830	17.27	$1.073 \cdot 10^{-6}$
11	0.165	0.0220	2850	16.92	$1.083 \cdot 10^{-6}$
12	0.167	0.0170	2820	16.42	$1.097 \cdot 10^{-6}$
13	0.153	0.0060	1920	16.64	$1.091 \cdot 10^{-6}$
14	0.075	0.0104	2430	17.29	$1.073 \cdot 10^{-6}$
15	0.058	0.0254	2820	16.92	$1.083 \cdot 10^{-6}$
16	0.062	0.0167	2820	16.43	$1.097 \cdot 10^{-6}$

Eq. 3.9 was tested by taking  $b_{eff}$  as either the total width of the abutment (i.e.,  $b$ ) or, as already discussed, the same width minus the counter-rotating recirculation region width (i.e.,  $b_r$ ), which was retrieved from the flow field measurements performed with the ADV down-looking probe. In fact, at equilibrium conditions and for each abutment a  $xy$ -grid of measure, with streamwise  $x$  and spanwise  $y$  axis resolution equal to 10% of the transversal length of the abutment, was captured at an elevation from the initial bed equal to 7.5 cm (i.e.,  $0.5h$ ).

Prior to the analysis of the ADV data, it was necessary to proceed with spike detection. Firstly, the ADV raw data were pre-filtered discarding the

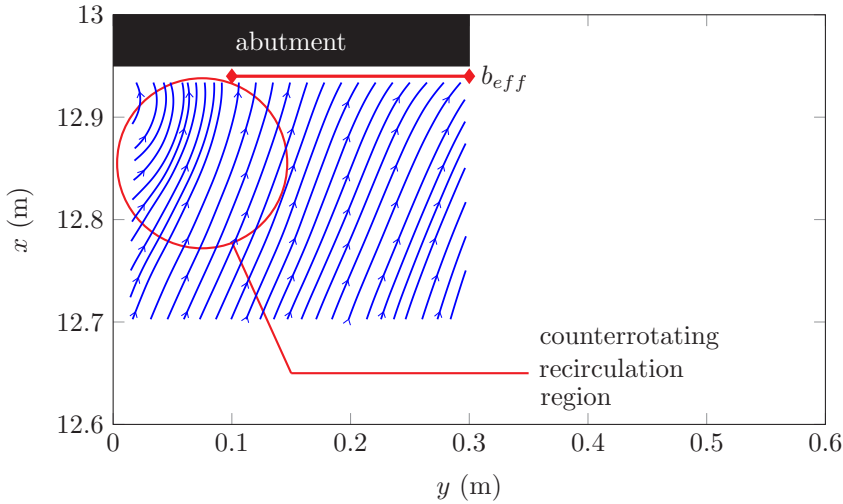


**Figure 3.49:** Example of a flow field measured with an ADV down-looking probe upstream to an abutment ( $x$  and  $y$  are the streamwise and spanwise coordinates measured from the inlet and the left side of the flume, respectively).

values with correlation lower than 70%; secondly, the contaminated velocity record was cleaned using the phase-space thresholding method and each spike was replaced with cubic polynomial through 12 points on either side of itself (Goring & Nikora, 2002). An example of  $xy$ -plane flow field at equilibrium conditions, used to calculate the dimension of the counter-rotating recirculation region,  $b_r$ , is reported in Fig 3.49. All analyses have been made with an *ad hoc* developed `Matlab`<sup>®</sup> code.

### 3.4 Results and discussion

Eq. 3.9 is to be validated with the results of the experimental campaign. Several considerations can be formulated on the function  $f$  of Eq. 3.9. In

particular, as reported in Chapter 2, for the pier scouring  $f$  is a combined function of  $d/\eta_1$  and  $a/d$ . The dependence on  $d/\eta_1$  is typical of a Shields diagram, conversely,  $f$  as a function of  $a/d$  has an increasing branch for  $a/d < 20$  and a constant branch for  $a/d > 20$ . In the abutment case,  $f$  is a function of  $d/\eta_1$  and  $b_{eff}/d$ .

For the present experiments, the values of the ratio  $b_{eff}/d$ , for  $b_{eff}$  considered as the total with  $b$  or as the total width minus the recirculation region  $b_r$ , are more than 20, implying that  $f$  can be considered as a constant for the relative roughness  $b_{eff}/d$ . Instead, the value  $d/\eta_1$ , remembering that

$$\eta_1 = \left( \frac{\nu^3 b_{eff}}{C_d U^3} \right)^{1/4} \quad (3.17)$$

and considering once again  $b_{eff}$  as  $b$  or  $b - b_r$ , varies between 10 and 150. Considering Fig. 2.3 and reasonably hypothesising that the same trend would occur in the abutment case, the variability of the function in this range of  $d/\eta_1$  is practically negligible. For this reason the function  $f$ , applied to the present experimental campaign, can be considered as a constant. Therefore, Eq. 3.9 becomes:

$$\frac{V_{scour}^{2/3} g}{y_{se} U^2} \sim \frac{\rho}{\rho_s - \rho} C_d^{2/3} \left( \frac{b_{eff}}{d} \right)^{2/3}. \quad (3.18)$$

In order to furnish a formula directly usable for the assessment of the equilibrium maximum scour depth, it is hypothesised, in the first instance and as reported in the previous Chapter, that  $V_{scour} \sim y_{se}^3$ . Therefore relation 3.18 becomes:

$$\frac{y_{se} g}{U^2} \sim \frac{\rho}{\rho_s - \rho} C_d^{2/3} \left( \frac{b_{eff}}{d} \right)^{2/3}. \quad (3.19)$$

The linear dependence of  $y_{se}g/U^2$  on  $C_d$  cannot be tested, because this parameter is, in general, practically constant and its range of validity is too small to verify the occurrence of a law with a good confidence. Instead, the proposed scaling for the product between  $\rho/(\rho_s - \rho)$  and  $(b_{eff}/d)^{2/3}$  can be extensively validated from experimental data. Note that the parameter  $\rho/(\rho_s - \rho)$  has a low influence compared to  $(b_{eff}/d)^{2/3}$ .

As reported above, the formula is validated using, firstly,  $b_{eff}$  equal to the total width of the abutment (Fig. 3.50(a)) and, secondly,  $b_{eff}$  as the same width minus the size of the recirculation region estimated from the flow field upstream to the obstacle (Fig. 3.50(b)).

Analysing Fig. 3.50, it is possible to conclude that the proposed scaling law holds for high values of the abscissa. For low values, the normalised scour depth is over-predicted by the theoretical model. Step back, with the purpose of validating the proposed theory, the scaling law is analysed without the hypothesis on the scour volume (i.e.,  $V_{scour} \sim y_{se}^3$ ). The ratio  $V_{scour}^{2/3}g/(y_{se}U^2)$  is, hence, plotted in Fig. 3.51 as a function of  $\rho/(\rho_s - \rho) \cdot (b_{eff}/d)^{2/3}$ . The experimental data agrees very well with the proposed theory with a coefficient of determination  $R^2$  equal to 0.95 and 0.94 in the case of  $b_{eff} = b$  (panel a) and  $b_{eff} = b - b_r$  (panel b), respectively. Moreover, the experimental points fall in the  $\pm 25\%$  error bounds that has a magnitude comparable with the formula proposed in the previous Chapter for the scour at piers and, hence, with the classical empirical formula for engineering applications.

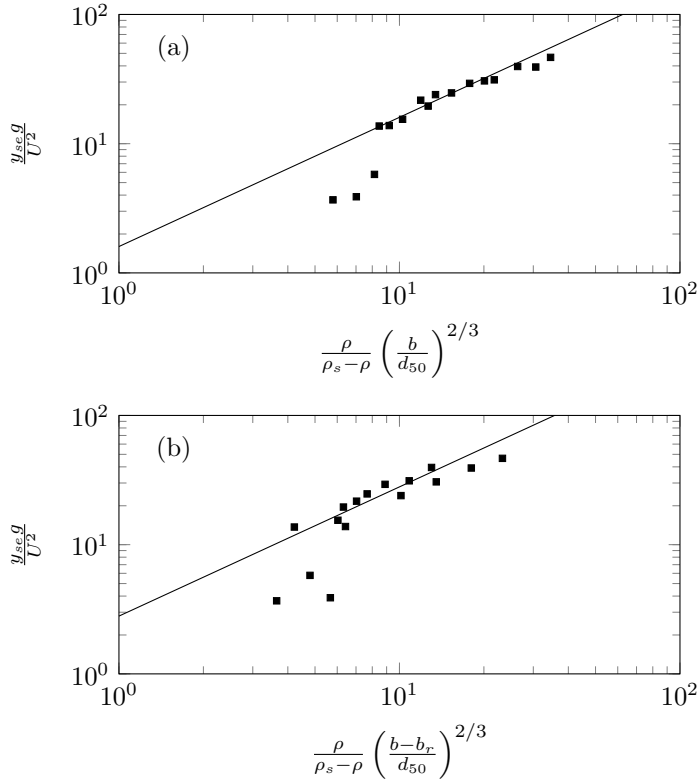


**Figure 3.50:** Dimensionless scour depths  $y_{se}g/U^2$  versus  $\rho/(\rho_s - \rho) \cdot (b_{eff}/d_{50})^{2/3}$ ; (a) considering  $b_{eff} = b$ , (b) considering  $b_{eff} = b - b_r$ . The solid line represents the linear law of relation 3.19.

### 3.5 Discussion and future investigation

This Chapter was devoted to an application of the PTT to local scouring at a bridge abutment. A scaling law (Eq. 3.18) for the assessment of equilibrium maximum scour volume and depth was found and successively validated with an experimental campaign. Unfortunately, in Eq. 3.18 both the scour volume and the scour depth are present, making, at least for now, its applicability impractical. As reported above, the reason whereby this is

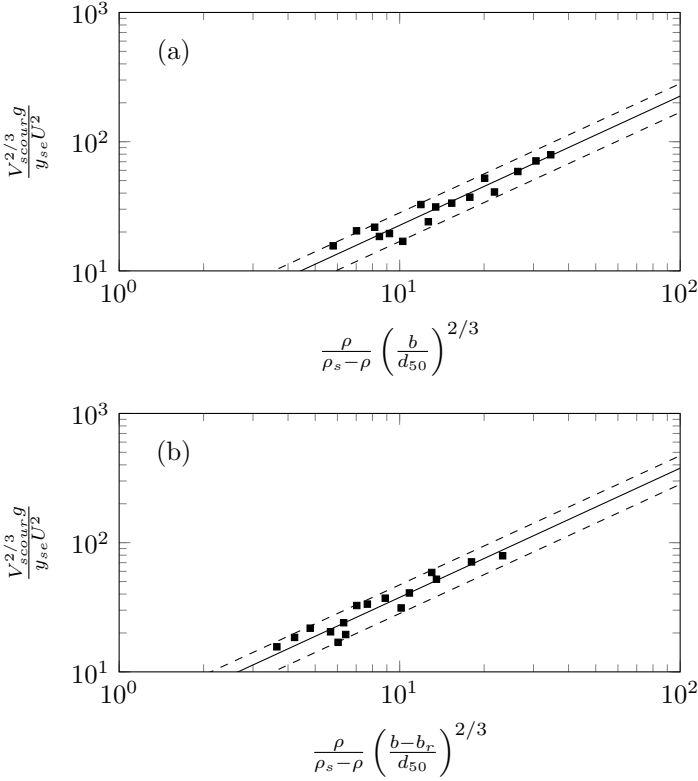


**Figure 3.51:** Dimensionless scour depths  $V_{scour}^{2/3} g / (y_{se} U^2)$  versus  $\rho / (\rho_s - \rho) \cdot (b_{eff} / d_{50})^{2/3}$ ; (a) considering  $b_{eff} = b$ , (b) considering  $b_{eff} = b - b_r$ . The solid line represents the linear law of relation 3.18 and the dashed lines the associated  $\pm 25\%$  error bounds.

evinced is imputable to a different scaling law between the volume and the scour depth with respect to the pier case (i.e.,  $V_{scour} \sim y_{se}^3$ , where the symbol  $\sim$  signify “not scales as”). More specifically, observing Fig. 3.50, it can be noted that some points, with low values of the abscissa, do not follow the theoretical law found under the hypothesis that  $V_{scour} \sim y_{se}^3$ . By comparing the scour hole shapes of the runs in which the hypothesis  $V_{scour} \sim y_{se}^3$

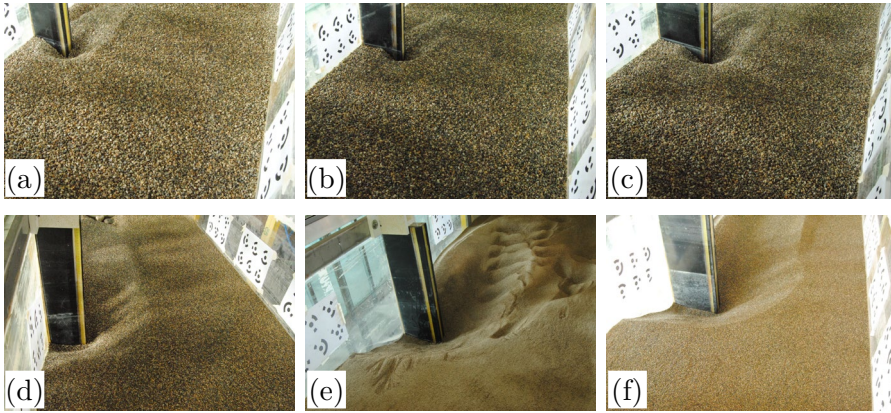


**Figure 3.52:** Scour hole shape for: (a) Run 16; (b) Run 15; (c) Run 14; (d) Run 12; (e) Run 3; (f) Run 5.

was respected with those of the runs in which it was not, a main difference emerges. Specifically, comparing the pictures in Figs. 3.52(a, b, c), referred to the runs in which  $V_{scour} \approx y_{se}^3$ , with those in Figs. 3.52(d, e, f), referred to the runs in which  $V_{scour} \sim y_{se}^3$ , one can see that, in the first cases, the upstream part of the scour hole does not reach the left wall, whereas, in the second cases, it does and, consequently, as reported by Melville (1997), is confined owing to the channel bank. Owing to the fact that the proportionality between  $V_{scour}$  and  $y_{se}^3$  is a condition not considered inside the PTT, the theory can be extended to the abutment case.

As in Manes & Brocchini (2015), the principal aim of the present Chapter is not to propose another predictive formula for engineering applications, but an approach that combines the PTT with considerations taken from empirical evidence of local scouring around abutments. In the future, as done in the previous Chapter for the case of local scour at piers, a complete model suitable for the esteem of the equilibrium scour depth at bridge abutments

should be developed. In particular, to do this, the following improvements must be done: (1) to consider a broad range of the parameter  $d/\eta_1$  in the experiments in order to evaluate viscous effects; (2) to analyse the link between  $V_{scour}$  and  $y_{se}$  as a function of the experimental parameters in order to find a predictive formula for  $y_{se}$ ; (3) to demonstrate, with a wide range of experiments, if the recirculation region has a real influence on the scouring phenomenon; (4) to vary the shape of the abutment in order to analyse the effects of the drag coefficient  $C_d$ .



# Conclusions

In the previous Chapters, the PTT has been applied to the scouring at structures. The aim of this doctoral thesis is to propose new developments that combine theoretical arguments with empirical considerations, to understand the physics of local scouring phenomenon around structures and, therefore, to furnish new strategies for the development of general predictive models that are founded more on physical rather empirical reasons.

The work of Bonetti et al. (2017), that has revised the Gioia & Bombardelli (2002) theory about the theoretical derivation for the well-known empirical laws in hydraulics (e.g., the Manning equation and the associated Strickler scaling for the roughness coefficient  $n$ ) was revised by Bonetti et al. (2017), as reported in Chapter 1. The results presented herein have a lot of implications: in fact, the Gioia & Bombardelli (2002) theory, that was at the base of all the recent applications of the PTT in hydraulics, must be modified in future works. In particular, the assumption that the local TKE dissipation rate scales as  $V^3/R$  and the hypothesis that the mean velocity gradient at the roughness crests scales as  $V/d$  must be revised. In fact, in the first case the scaling laws include the scaling function  $\alpha_2$ , whereas in the second case, the scaling function  $\alpha_1$ ; both the scaling functions depend on

$Re$  and  $d/L$ . In addition, starting from the results of Bonetti et al. (2017) and performing original analytical passages, was find useful results about the correct application of the PTT in hydraulics and turbulence research, in particular in the field of scouring.

Manes & Brocchini (2015) approach was recasted within a more rigorous and general theoretical framework to derive a predictive formula for the equilibrium maximum scour depth at piers under clear-water steady flows. It was demonstrated that, regardless of whether near-bed eddies pertain to the dissipation or production range, the shear stress acting within the scour hole can be estimated relatively well by means of the original formulation proposed by Manes & Brocchini (2015) (provided that the scaling functions  $\alpha_1$  and  $\alpha_2$  are also taken into account), whereby near-bed eddies scale with the sediment diameter and belong to the inertial range. Furthermore, in equilibrium conditions, contrarily to the shear stress, the critical shear stress is strongly affected by the nature and scale of near-bed eddies. In particular, viscosity effects, which contribute to identify the characteristic length,  $l$ , and the velocity scale,  $w_l$ , of such eddies (see Eq. 2.9), are significant for a wide range of  $d/\eta_1$ . Such effects are taken into account through function  $f_1$  (Eq. 2.18), whereas, when near-bed eddies pertain to the production range (i.e., for  $a/d < 20$ ), the equilibrium conditions strongly depend on the relative roughness  $a/d$ , as described by function  $f_2$  (Eq. 2.30). Finally, when functions  $f_1$  and  $f_2$  are combined in Eq. 2.32, the agreement between measured and computed equilibrium maximum scour depths is better than that in Manes & Brocchini (2015) and comparable with that of existing empirical formulae. With respect to Eq. 2.32, its applicability is still limited to cylindrical piers, clear-water and uniform-sediment conditions and is, there-

fore, incomplete. However, it represents an important first step towards the development of a physically-based and hence universal (i.e., free from scale issues) formula for local scour prediction. Further investigations should be done considering different pier shapes and orientations of the structure with respect to the flow direction, which have influence on the drag coefficient,  $C_d$ , and for the cases of non-uniform grain size distribution and live-bed conditions.

Finally, the PTT has been applied to the scouring at bridge abutments. Starting from the pier scour theory, a new approach for the abutment scouring has been proposed on the base of different scour mechanisms at piers and abutments. In fact, as reported by Melville & Raudkivi (1977), Kwan (1988), Melville & Raudkivi (1996) and Melville (1997), the scour depth at the abutment is acknowledged to be less than that at the pier with the same width, owing to the channel wall retardation effects on the flow. In addition, the similarity of the flow field can be found within the scour hole around piers and abutments with the same transversal length extending into the channel only for a short distance, with respect to the flow depth. Conversely, for long abutments, the classical scientific literature has identified two flow regions: 1) a principal spiral flow, near the channel centreline, that is the main and unique responsible of the scouring process; 2) a secondary counter-rotating flow, formed at the junction between the bridge abutment and the channel bank. This quiescent fluid zone can be considered to demarcate the surface of an “effective” abutment, because the fluid within this area does not affect the scour process. This observation was considered in the theoretical approach that led to the scaling law for the maximum equilibrium scour volume and depth in Eq. 3.18. This scaling law, that was

validated with an experimental campaign, presents the issue of its impracticability for the assessment of  $y_{se}$  owing to the presence of both equilibrium scour volume and maximum scour depth; nevertheless, it could help for future investigations. In fact, as in Manes & Brocchini (2015), the principal aim of the last Chapter is not to propose another predictive formula for engineering applications, but, instead, to propose the approach that combines the PTT with considerations taken from empirical evidence of local scouring around abutments. In the future, as done for the case of local scour at piers in Chapter 2, a complete model suitable for the estimation of the equilibrium maximum scour depth at bridge abutments should be developed. As reported in Chapter 3, to do this, some improvements must be performed.

Hence, this study provides a physical view into hydraulics problems and in particular in the scouring phenomenon occurring at bridge piers and abutments by elucidating the interaction between the localised turbulence and the sediment particles. The proposed concepts, founded on the latest results of PTT, could be further used to analyse many other practical problems, which involve the fluid-sediment interaction, with the improvements suggested above, and for other scouring mechanisms, as well as for pressurised pipe flows and open-channel flows.

# References

- Ali, S. Z., & Dey, S. (2018). Impact of phenomenological theory of turbulence on pragmatic approach to fluvial hydraulics. *Physics of Fluids*, 30(4), 045105.
- Baker, C. (1980). Theoretical approach to prediction of local scour around bridge piers. *Journal of Hydraulic Research*, 18(1), 1–12.
- Baltsavias, E. P. (1999). A comparison between photogrammetry and laser scanning. *ISPRS Journal of photogrammetry and Remote Sensing*, 54(2-3), 83–94.
- Bombardelli, F. A., & Gioia, G. (2006). Scouring of granular beds by jet-driven axisymmetric turbulent cauldrons. *Physics of fluids*, 18(8), 088101.
- Bonetti, S., Manoli, G., Manes, C., Porporato, A., & Katul, G. (2017). Manning’s formula and strickler’s scaling explained by a co-spectral budget model. *Journal of Fluid Mechanics*, 812, 1189–1212.
- Breusers, H., Nicollet, G., & Shen, H. (1977). Local scour around cylindrical piers. *Journal of Hydraulic Research*, 15(3), 211–252.

- Brownlie, W. R. (1981). Prediction of flow depth and sediment discharge in open channels.
- Buffington, J. M., & Montgomery, D. R. (1997). A systematic analysis of eight decades of incipient motion studies, with special reference to gravel-bedded rivers. *Water Resources Research*, *33*(8), 1993–2029.
- Chang, W.-Y., Constantinescu, G., Lien, H.-C., Tsai, W.-F., Lai, J.-S., & Loh, C.-H. (2013). Flow structure around bridge piers of varying geometrical complexity. *Journal of Hydraulic Engineering*, *139*(8), 812–826.
- Coleman, S. E., Lauchlan, C. S., & Melville, B. W. (2003). Clear-water scour development at bridge abutments. *Journal of Hydraulic Research*, *41*(5), 521–531.
- Coscarella, F., Servidio, S., Ferraro, D., Carbone, V., & Gaudio, R. (2017). Turbulent energy dissipation rate in a tilting flume with a highly rough bed. *Physics of Fluids*, *29*(8), 085101.
- Davidson, P. (2015). *Turbulence: an introduction for scientists and engineers*. Oxford University Press.
- Dey, S. (1999). Time-variation of scour in the vicinity of circular piers. *Proceedings of the Institution of Civil Engineers-Water Maritime and Energy*, *136*(2), 67–75.
- Dey, S. (2014). *Fluvial hydrodynamics*. Springer.
- Dey, S., Bose, S. K., & Sastry, G. L. (1995). Clear water scour at circular piers: a model. *Journal of Hydraulic Engineering*, *121*(12), 869–876.

- Dey, S., & Sarkar, A. (2006). Scour downstream of an apron due to submerged horizontal jets. *Journal of hydraulic engineering*, 132(3), 246–257.
- Ettema, R. (1980). *Scour at bridge piers*. (Tech. Rep.).
- Ettema, R., Kirkil, G., & Muste, M. (2006). Similitude of large-scale turbulence in experiments on local scour at cylinders. *Journal of Hydraulic Engineering*, 132(1), 33–40.
- Ettema, R., Melville, B. W., & Constantinescu, G. (2011). *Evaluation of bridge scour research: Pier scour processes and predictions*.
- Ettema, R., Nakato, T., & Muste, M. (2010). *Estimation of scour depth at bridge abutments*.
- Frisch, U. (1995). *Turbulence: the legacy of an kolmogorov*. Cambridge University Press.
- Garde, R. (1968). Initiation of motion on a hydrodynamically rough surface—critical velocity approach. *Journal of Irrigation and Power*, 27(3), 271–282.
- Gioia, G., & Bombardelli, F. (2002). Scaling and similarity in rough channel flows. *Physical review letters*, 88(1), 014501.
- Gioia, G., & Bombardelli, F. A. (2005). Localized turbulent flows on scouring granular beds. *Physical review letters*, 95(1), 014501.
- Gioia, G., & Chakraborty, P. (2006). Turbulent friction in rough pipes and the energy spectrum of the phenomenological theory. *Physical review letters*, 96(4), 044502.

- Gioia, G., Guttenberg, N., Goldenfeld, N., & Chakraborty, P. (2010). Spectral theory of the turbulent mean-velocity profile. *Physical review letters*, *105*(18), 184501.
- Goncharov, V. (1964). Dynamics of channel flow. *Israel Programme for Scientific Translation*, Moscow.
- Goring, D. G., & Nikora, V. I. (2002). Despiking acoustic doppler velocimeter data. *Journal of Hydraulic Engineering*, *128*(1), 117–126.
- Guo, J. (2014). Semi-analytical model for temporal clear-water scour at prototype piers. *Journal of Hydraulic Research*, *52*(3), 366–374.
- Julien, P. Y. (1998). *Erosion and sedimentation*. Cambridge University Press.
- Katul, G. G., & Manes, C. (2014). Cospectral budget of turbulence explains the bulk properties of smooth pipe flow. *Physical Review E*, *90*(6), 063008.
- Katul, G. G., Manes, C., Porporato, A., Bou-Zeid, E., & Chamecki, M. (2015). Bottlenecks in turbulent kinetic energy spectra predicted from structure function inflections using the von Kármán-Howarth equation. *Physical Review E*, *92*(3), 033009.
- Katul, G. G., Porporato, A., Manes, C., & Meneveau, C. (2013). Co-spectrum and mean velocity in turbulent boundary layers. *Physics of Fluids*, *25*(9), 091702.



- Kindsvater, C. E., & Carter, R. W. (1959). Discharge characteristics of rectangular thin-plate weirs. *Transactions of the American Society of Civil Engineers*, 124(1), 772–801.
- Kirkil, G., Constantinescu, S. G., & Ettema, R. (2008). Coherent structures in the flow field around a circular cylinder with scour hole. *Journal of Hydraulic Engineering*, 134(5), 572–587.
- Kolmogorov, A. N. (1941). The local structure of turbulence in incompressible viscous fluid for very large reynolds numbers. In *Dokl. akad. nauk sssr* (Vol. 30, pp. 299–303).
- Kothiyari, U. C., Garde, R. C. J., & Ranga Raju, K. G. (1992). Temporal variation of scour around circular bridge piers. *Journal of Hydraulic Engineering*, 118(8), 1091–1106.
- Kwan, T. (1984). Study of abutment scour.
- Kwan, T. (1988). A study of abutment scour.
- Lane, E. W. (1947). Report of the subcommittee on sediment terminology. *Eos, Transactions American Geophysical Union*, 28(6), 936–938.
- Lohse, D., & Müller-Groeling, A. (1995). Bottleneck effects in turbulence: scaling phenomena in r versus p space. *Physical review letters*, 74(10), 1747.
- Manes, C., & Brocchini, M. (2015). Local scour around structures and the phenomenology of turbulence. *Journal of Fluid Mechanics*, 779, 309–324.

- Manes, C., Pokrajac, D., & McEwan, I. (2007). Double-averaged open-channel flows with small relative submergence. *Journal of Hydraulic Engineering*, *133*(8), 896–904.
- Manning, R. (1890). On the flow of water in open channels and pipe. *Trans. Inst. Civil Eng. Ireland*, *20*(7), 161–207.
- Melville, B. W. (1992). Local scour at bridge abutments. *Journal of Hydraulic Engineering*, *118*(4), 615–631.
- Melville, B. W. (1997). Pier and abutment scour: integrated approach. *Journal of hydraulic Engineering*, *123*(2), 125–136.
- Melville, B. W., & Coleman, S. E. (2000). *Bridge scour*. Water Resources Publication.
- Melville, B. W., & Raudkivi, A. J. (1977). Flow characteristics in local scour at bridge piers. *Journal of Hydraulic Research*, *15*(4), 373–380.
- Melville, B. W., & Raudkivi, A. J. (1996). Effects of foundation geometry on bridge pier scour. *Journal of Hydraulic Engineering*, *122*(4), 203–209.
- Mignosa, P. (1980). *Fenomeni di erosione locale alla base delle pile dei ponti*. Master degree, Department of hydraulic and Hydraulic structure, Politecnico di Milano.
- Mueller, E. R., Pitlick, J., & Nelson, J. M. (2005). Variation in the reference shields stress for bed load transport in gravel-bed streams and rivers. *Water Resources Research*, *41*(4).
- Neill, C. (1968). Note on initial movement of coarse uniform bed-material. *Journal of Hydraulic Research*, *6*(2), 173–176.

- Nezu, I., & Nakagawa, H. (1993). Turbulence in open channels. *IAHR/AIRH Monograph. Balkema, Rotterdam, The Netherlands*.
- Nikuradse, J. (1933). Strömungsgesetze in rauhen röhren.
- Poggi, D., Porporato, A., & Ridolfi, L. (2002). An experimental contribution to near-wall measurements by means of a special laser doppler anemometry technique. *Experiments in Fluids*, 32(3), 366–375.
- Pope, S. B. (2001). *Turbulent flows*. IOP Publishing.
- Radice, A., Ballio, F., & Porta, G. (2009). Local scour at a trapezoidal abutment: Sediment motion pattern. *Journal of Hydraulic Research*, 47(2), 250–262.
- Raudkivi, A. J., & Ettema, R. (1983). Clear-water scour at cylindrical piers. *Journal of Hydraulic Engineering*, 109(3), 338–350.
- Raupach, M., Antonia, R., & Rajagopalan, S. (1991). Rough-wall turbulent boundary layers. *Applied mechanics reviews*, 44(1), 1–25.
- Richardson, E. V., Harrison, L. J., Richardson, J., & Davis, S. (1993). *Evaluating scour at bridges*. (Tech. Rep.).
- Richardson, L. F. (1922). *Weather prediction by numerical process*. Cambridge University Press.
- Rotta, J. (1962). Turbulent boundary layers in incompressible flow. *Prog. Aero. Sci.*, 46.

- Saddoughi, S. G., & Veeravalli, S. V. (1994). Local isotropy in turbulent boundary layers at high Reynolds number. *Journal of Fluid Mechanics*, 268, 333–372.
- Sheppard, D. M., & Miller Jr, W. (2006). Live-bed local pier scour experiments. *Journal of Hydraulic Engineering*, 132(7), 635–642.
- Sheppard, D. M., Odeh, M., & Glasser, T. (2004). Large scale clear-water local pier scour experiments. *Journal of Hydraulic Engineering*, 130(10), 957–963.
- Shields, A. (1936). Anwendung der aehnlichkeitsmechanik und der turbulenzforschung auf die geschiebebewegung. *PhD Thesis Technical University Berlin*.
- Sreenivasan, K. R. (1995). On the universality of the kolmogorov constant. *Physics of Fluids*, 7(11), 2778–2784.
- Unger, J., & Hager, W. H. (2007). Down-flow and horseshoe vortex characteristics of sediment embedded bridge piers. *Experiments in Fluids*, 42(1), 1–19.
- Yang, B. H., & Joseph, D. D. (2009). Virtual Nikuradse. *Journal of Turbulence*(10), N11.
- Yanmaz, A. M., & Altinbilek, H. D. g. . a. (1991). Study of time-dependent local scour around bridge piers. *Journal of Hydraulic Engineering*, 117(10), 1247–1268.